

# **EXPERIMENTATION AND PHYSICAL LAYER MODELING FOR OPPORTUNISTIC LARGE ARRAY-BASED NETWORKS**

A Dissertation  
Presented to  
The Academic Faculty

By

Haejoon Jung

In Partial Fulfillment  
of the Requirements for the Degree  
Doctor of Philosophy  
in  
Electrical and Computer Engineering



School of Electrical and Computer Engineering  
Georgia Institute of Technology  
May 2014

Copyright © 2014 by Haejoon Jung

# **EXPERIMENTATION AND PHYSICAL LAYER MODELING FOR OPPORTUNISTIC LARGE ARRAY-BASED NETWORKS**

Approved by:

Professor Mary Ann Weitnauer, Advisor  
*School of Electrical and Computer  
Engineering  
Georgia Institute of Technology*

Professor Hua Wang  
*School of Electrical and Computer  
Engineering  
Georgia Institute of Technology*

Professor John Barry  
*School of Electrical and Computer  
Engineering  
Georgia Institute of Technology*

Professor Sung Ha Kang  
*School of Mathematics  
Georgia Institute of Technology*

Professor Ye (Geoffrey ) Li  
*School of Electrical and Computer  
Engineering  
Georgia Institute of Technology*

Date Approved: January 2014

*To my parents and my wife.*

## ACKNOWLEDGMENTS

I would like to sincerely thank my advisor Prof. Mary Ann Weitnauer for her guidance and continuous support. She has been an excellent advisor and mentor with motivation, enthusiasm, patience, and immense knowledge. I am deeply indebted to her for providing me with insightful suggestion, feedback, advice, and encouragement during my doctoral study. In addition to her fundamental role in our academic research, I greatly appreciate her close personal rapport with all of her students and their families.

My special thanks go to the members of my thesis committee, Prof. John Barry, Prof. Ye (Geoffrey) Li, Prof. Hua Wang, and Prof. Sung Ha Kang for their terrific support during my graduate studies at Georgia Tech. Their enlightening suggestions have greatly improved my research and the quality of this dissertation.

I also would like to thank the professors of Yonsei University, Prof. Sooyong Choi, Prof. Taewon Hwang, Prof. Chungyong Lee, and Prof. Seong-Lyun Kim for writing recommendation letters for my PhD study and giving continuous advices. In particular, I am deeply grateful to Prof. Chungyong Lee for officiating and blessing my wedding.

I thank my friends and colleagues at the Smart Antenna Research Lab, Alper Akanser, Dr. Yong Jun Chang, Sunghwan Cho, Dr. Sayed Ali Hassan, Dr. Jin Woo Jung, Dr. Aravind Kailas, Jian Lin, Qiongjie Lin, Van Nguyen, Gaurav Pradhan, Abdul Qadir, Dr. Lakshmi Thanayankizil, and Feng Wang. I also thank the visiting scholars, Mingxi Zhang, Dr. Nikolaj Marchenko, Dr. Gao Zhen, Zhenzhe (Stephen) Sun, and Lakshmikanth Guntupali. Further, I thank all my Korean friends at Georgia Tech including Dr. Hyongsuk Jeon, Dr. Namshik Kim, Dr. Seok-chul Kwon, and Dr. Hyung-Seok Yu.

Finally, I wish to thank my parents and wife. My parents, Seungjin Jung and Hoisook Kim have always believed in me and encouraged me to reach my goals. Their love and sacrifice have enabled me to attain this advanced stage in my career. Finally, I would like to dedicate this work to my dear wife, Heyjin Lee, whose love and encouragement helped



me complete this journey.

# TABLE OF CONTENTS

<b>ACKNOWLEDGMENTS</b> . . . . .	iv
<b>LIST OF TABLES</b> . . . . .	x
<b>LIST OF FIGURES</b> . . . . .	xi
<b>SUMMARY</b> . . . . .	1
<b>CHAPTER 1 INTRODUCTION</b> . . . . .	2
<b>CHAPTER 2 ORIGIN AND HISTORY OF THE PROBLEM</b> . . . . .	6
2.1 Multi-packet OLA Transmission and Intra-flow Interference . . . . .	6
2.1.1 Broadcasting in Wireless Multi-hop networks . . . . .	9
2.1.2 OLA Transmission on Strip-shaped cooperative Routes or Networks . . . . .	10
2.2 Cooperative Transmission Link Model . . . . .	11
2.2.1 Outage Probability of a Virtual Multiple-Input- Single-Output (VMISO) Link . . . . .	12
2.2.2 Link Asymmetry of a Virtual Multiple-Input-Single- Output (VMISO) Link . . . . .	13
2.3 Experimental Studies on CCT . . . . .	14
2.4 OLA-based Routing and Error Control Algorithms . . . . .	15
2.4.1 Reliability and Error Control . . . . .	16
2.4.2 Existing Medium Access and Error Control for CT-based Routing . . . . .	17
<b>CHAPTER 3 ANALYTICAL FRAMEWORK FOR INTRA-FLOW ANALYSIS</b> 21	
3.1 Deterministic Channel and Continuum Assumptions . . . . .	22
3.2 Validity in Finite-density Networks . . . . .	24
3.3 Two-dimensional Disk Networks . . . . .	25
3.4 Two-dimensional Strip Networks . . . . .	28
3.4.1 Free Space Path Attenuation ( $\alpha = 2$ ) . . . . .	30
3.4.2 Higher Path Attenuation ( $\alpha > 2$ ) . . . . .	30
3.5 Multi-packet Transmission and Network Throughput . . . . .	32
<b>CHAPTER 4 MULTI-PACKET OLA BROADCASTS IN DISK NETWORKS</b>	35
4.1 Signal Model of Intra-flow Interference . . . . .	35
4.2 Theoretical Analysis of Pipelined broadcast in the infinite disk network . . . . .	36
4.2.1 Feasibility for Free Space Path Loss Exponent ( $\alpha = 2$ ) . . . . .	36
4.2.2 Feasibility for Higher Path Loss Exponent ( $\alpha > 2$ ) . . . . .	40

4.2.3	Lower Bound of Broadcast Throughput with $\alpha > 2$ for the Interference-limited Case . . . . .	41
4.3	Numerical Results with the Finite Disk Network in Free Space ( $\alpha = 2$ ) . . . . .	45
4.3.1	Ten-Packet Example . . . . .	47
4.3.2	Step-size Control . . . . .	49
4.4	Numerical Results with the Finite Network for Higher Path Loss Exponents ( $\alpha > 2$ ) . . . . .	50
4.4.1	Twenty-Packet Example in the Finite Disk Network . . . . .	51
4.4.2	Impacts of $\alpha$ and $\bar{P}_r$ on $M_{R,opt}$ . . . . .	54
4.4.3	Impacts of $\tau$ on $M_{R,opt}$ . . . . .	55
4.5	Summary . . . . .	57

## CHAPTER 5 MULTI-PACKET OLA TRANSMISSION ON STRIP-SHAPED COOPERATIVE ROUTES OR NETWORKS . . . . .

5.1	Signal Model of Intra-flow Interference . . . . .	58
5.2	Multi-packet Propagation for the Finite Strip . . . . .	58
5.2.1	Upper Bounds on Hop-Counts and Step-sizes . . . . .	59
5.2.2	Packet Insertion Period . . . . .	60
5.2.3	Worst-Case Packet . . . . .	61
5.2.4	Stable State with Equal Step-size . . . . .	62
5.3	Spatial Pipelining in the Infinite Strip Network . . . . .	64
5.3.1	Feasibility of Spatial Pipelining . . . . .	64
5.3.2	Lower Bound of Optimal Throughput for the Interference-limited Case . . . . .	64
5.4	Optimal Packet Insertion Period in the Finite Network . . . . .	67
5.4.1	Equal Step-size Approximation . . . . .	68
5.4.2	Upper Bound of $M_{L,opt}$ with $\alpha = 2$ . . . . .	68
5.4.3	Possible Multi-packet Transmission Strategy . . . . .	69
5.5	Numerical Analysis of Optimal Throughput in the Finite Strip Network . . . . .	71
5.5.1	Impact of $P_s$ , $\bar{P}_r$ , and $\alpha$ on $M_{L,opt}$ with $\alpha = 2, 3$ , and 4 . . . . .	72
5.5.2	Impact of $\tau$ and $\alpha$ on $M_{L,opt}$ with $\alpha = 2, 3$ , and 4 . . . . .	74
5.5.3	Impact of Simultaneous Variations in $\bar{P}_r$ and $\tau$ with Fixed Ratio for $\alpha = 2, 3$ , and 4 . . . . .	76
5.6	Summary . . . . .	77

## CHAPTER 6 VIRTUAL MULTIPLE-INPUT-SINGLE-OUTPUT (VMISO) LINK ANALYSIS OF CCT . . . . .

6.1	SNR Penalty from the Path-loss Disparity in a VMISO Link . . . . .	79
6.1.1	System Model . . . . .	79
6.1.2	Outage Rate Approximation . . . . .	81
6.1.3	Upper and Lower Bounds of Outage Rate . . . . .	84
6.1.4	Simulation Results and Discussion . . . . .	86

6.2	Link Asymmetry in VMISO-based Networks . . . . .	89
6.2.1	System Model . . . . .	89
6.2.2	Correlation of Forward and Reverse Links . . . . .	91
6.2.3	Link Asymmetry Quantified by Power Ratio . . . . .	93
6.3	Summary . . . . .	99
<b>CHAPTER 7 EXPERIMENTAL STUDIES OF CONCURRENT COOPERATIVE TRANSMISSION . . . . .</b>		<b>100</b>
7.1	Two-hop Range Extension of Concurrent Cooperative Transmission . . . . .	100
7.1.1	Experiment Design . . . . .	100
7.1.2	Measurement Campaign with Three Topologies . . . . .	104
7.1.3	Experimental Results . . . . .	108
7.2	Demonstration of an OLA-based Routing Protocol . . . . .	113
7.2.1	Original OLAROAD Protocol . . . . .	113
7.2.2	Protocol Modification . . . . .	115
7.2.3	Network Model . . . . .	117
7.2.4	Experimental Results . . . . .	119
7.3	Summary . . . . .	125
<b>CHAPTER 8 OLA-BASED ROUTING AND ERROR CONTROL . . . . .</b>		<b>127</b>
8.1	Comparison Cases . . . . .	127
8.2	Example Routes of OLA-PRISE and OLAROAD . . . . .	127
8.3	Issues in Link-level MAC and ARQ for OLA-based Routing . . . . .	131
8.3.1	Uncertainty in Link Definition . . . . .	131
8.3.2	Cluster-level Decision . . . . .	131
8.3.3	Link Asymmetry . . . . .	132
8.4	Proposed Algorithms . . . . .	132
8.4.1	Routing Operation based on Node Degree . . . . .	133
8.4.2	Local Ganging in OLA-PRISE . . . . .	135
8.5	Simulation Results . . . . .	136
8.5.1	System Model . . . . .	136
8.5.2	Simulation Results . . . . .	138
8.6	Summary . . . . .	141
<b>CHAPTER 9 CONCLUSION AND SUGGESTED FUTURE WORKS . . . . .</b>		<b>143</b>
<b>APPENDIX A PROOF OF THE PROPERTIES OF <math>H(X)</math> . . . . .</b>		<b>147</b>
<b>APPENDIX B PROOF OF THEOREM 1 . . . . .</b>		<b>149</b>
<b>APPENDIX C PROOF OF THEOREM 2 . . . . .</b>		<b>150</b>
<b>APPENDIX D PROOF OF THEOREM 3 . . . . .</b>		<b>151</b>
<b>APPENDIX E PROOF OF THEOREM 4 . . . . .</b>		<b>153</b>

<b>REFERENCES . . . . .</b>	<b>156</b>
-----------------------------	------------

## LIST OF TABLES

Table 1	Feasibility of spatially-pipelined OLA broadcasts in the infinite disk network ( $\alpha$ : path-loss exponent, $\tau$ : decoding threshold, $\bar{P}_r$ : transmit power per unit area, $\mu = \exp(\frac{\tau}{\pi\bar{P}_r})$ ) . . . . .	37
Table 2	Numerically computed minimum packet insertion periods $\hat{M}_{I,opt}$ and $\hat{M}_{I,opt}^*$ for $\tau = 1$ . . . . .	45
Table 3	Average step-sizes of Packet 25 with different transmit powers . . . . .	73
Table 4	Directional range-extension ratios $\rho_d$ . . . . .	111
Table 5	Coverage-extension ratios $\rho_c$ . . . . .	112
Table 6	Configuration parameters in AODV implementation. . . . .	119
Table 7	Three CT-based Routing Algorithms . . . . .	128

## LIST OF FIGURES

Figure 1	Three-nodes cooperative transmission model . . . . .	6
Figure 2	Concurrent cooperative transmission (CCT) model . . . . .	7
Figure 3	The sequence of packet transmission on a virtual MISO link in [1] . . . . .	18
Figure 4	Path Access Control (PAC) in [2] . . . . .	19
Figure 5	The sequence of packet transmission on a virtual MISO link in [3] . . . . .	20
Figure 6	Coverage analysis based on Continuum approach . . . . .	26
Figure 7	The OLA transmission on the strip network based on the continuum assumption and straight line approximation . . . . .	28
Figure 8	$h(x)$ curves for $\alpha = 2$ and $3$ , when $\bar{P}_r = 3$ , $\tau = 1$ , and $W = 1$ . . . . .	31
Figure 9	Timing diagram of spatial pipelined OLA with $M = 3$ . . . . .	33
Figure 10	Intra-flow interference of multiple packets OLA broadcasts . . . . .	35
Figure 11	Illustration to derive the lower bound of SINR for a given packet insertion period $M$ . . . . .	41
Figure 12	$\alpha$ versus $1/q(\alpha)$ , when $\tau = \{1, 10, 100\}$ . . . . .	43
Figure 13	The time evolution of the distances, when $\mu=1.8$ , $M=34$ , $M_0=35$ , and $R=300$ . . . . .	48
Figure 14	The time evolution of the distances, when $\mu=2$ , $M=9$ , $M_0=10$ , and $R=10$ . . . . .	49
Figure 15	The time evolution of distances with step-size control, when $M=95$ , $M_0=94$ , and $R=300$ . . . . .	49
Figure 16	Numerical results with twenty packets for $\alpha = 2.5$ , when $M = M_{R,opt} = 6$ , $M_0 = 50$ , and $R = 68000$ . . . . .	52
Figure 17	Numerical results with twenty packets for $\alpha = 4$ , when $M = M_{R,opt} = 3$ , $M_0 = 50$ , and $R = 200$ . . . . .	52
Figure 18	Numerical results for the different path loss exponents $\alpha = \{2.5, 3, 3.5, 4\}$ , when $M_0 = 50$ , $\tau = 10$ , and $\bar{P}_r = P_s = \{100, 400\}$ . . . . .	55

Figure 19	Numerical results for the different decoding thresholds $\tau = \{5, 10, 15, 20\}$ , when $\alpha = \{2.5, 3, 3.5, 4\}$ , $M_0 = 50$ , and $\bar{P}_r = P_s = 300$ . . . . .	55
Figure 20	The snapshot of multiple-packet OLA broadcast . . . . .	59
Figure 21	The time evolution of the hop distances, when $M = 10$ . . . . .	60
Figure 22	The time evolution of the hop distances, when $M = 5$ . . . . .	60
Figure 23	The overlapped step-sizes $r_{(i,k)}$ curves of 200 packets . . . . .	62
Figure 24	Numerical results with the increasing $\bar{P}_r = P_s$ , when $\tau = 10^3$ , $W = 1$ and $L = 1200, 215, 121$ for $\alpha = 2, 3, 4$ , respectively . . . . .	73
Figure 25	Numerical results with the increasing $\tau = 25, 50, 75, 100$ for path loss exponents $\alpha = 2, 3, 4$ , when $P_s = \bar{P}_r = 5000$ , $M_0 = 50$ , and $W = 1$ . . . . .	75
Figure 26	Numerical results for the same ratio of $\frac{\bar{P}_r}{\tau}$ : $(P_s, \bar{P}_r, \tau) = (50, 50, 1)$ , $(5 \times 10^2, 5 \times 10^2, 10)$ , $(5 \times 10^3, 5 \times 10^3, 10^2)$ , $(5 \times 10^4, 5 \times 10^4, 10^3)$ , when $\alpha = 2, 3, 4$ , $M_0 = 50$ , and $W = 1$ . . . . .	76
Figure 27	Logical illustration of a VMISO-based multi-hop network . . . . .	78
Figure 28	Two-hop cooperative transmission scenario for each cooperative hop . . . . .	79
Figure 29	Network topology model . . . . .	79
Figure 30	PDF of $d_k$ and its approximations, when $r_s = 1$ and $d_0 = 4$ . . . . .	85
Figure 31	Outage curves, when $R = 1$ , $d_0 = 2$ , $r_s = 1$ , $\alpha = 4$ , and $N = 6, 8$ . . . . .	86
Figure 32	$d_0/r_s$ versus SNR gaps, when $r_s = 1$ , $\alpha = 4$ , and $N = 6$ . . . . .	88
Figure 33	$\alpha$ versus SNR gaps, when $r_s = 1$ , $d_0 = 2$ , and $N = 6$ . . . . .	88
Figure 34	$N$ versus SNR gaps, when $r_s = 1$ , $d_0 = 2$ , and $\alpha = 4$ . . . . .	88
Figure 35	Network topology model . . . . .	89
Figure 36	Illustration of forward and reverse links . . . . .	91
Figure 37	Correlation coefficient versus number of relays $L$ . . . . .	92
Figure 38	Two CDFs of $\eta = \frac{P_R}{P_F}$ with $d_0 = 2$ , $r_s = 1$ , and $\alpha = 4$ . . . . .	95
Figure 39	$d_0/r_s$ versus for $\alpha = 4$ and $L = 6$ . . . . .	97



Figure 40	$\alpha$ versus for $d_0/r_s = 2$ and $L = 6$ . . . . .	97
Figure 41	$L$ versus for $d_0/r_s = 2$ and $\alpha = 4$ . . . . .	97
Figure 42	$F_\eta(x)$ with $L = 1$ and $2$ for $d_0/r_s = 2$ and $\alpha = 4$ . . . . .	98
Figure 43	Floor plan of the measurement environment. . . . .	102
Figure 44	The logical topology of the experiment. . . . .	102
Figure 45	Testbed nodes: (a) the receiver cluster, (b) one relay node. . . . .	103
Figure 46	Three measurement topologies. . . . .	105
Figure 47	Scatter plot of $\bar{\gamma}(\mathbf{d})$ and its linear regression. . . . .	107
Figure 48	Topology1 (wide dispersion): (a) measurement, (b) experiment. . . . .	109
Figure 49	Topology 2 (medium cluster): (a) measurement, (b) experiment. . . . .	109
Figure 50	Topology 3 (tight cluster): (a) measurement, (b) experiment. . . . .	110
Figure 51	An example of the OLAROAD routing. . . . .	115
Figure 52	Network topology of the routing experiment. . . . .	120
Figure 53	Node degree depending on transmit power levels. . . . .	121
Figure 54	End-to-end hop count. . . . .	122
Figure 55	End-to-end round trip time (RTT). . . . .	123
Figure 56	Packet delivery ratio (PDR). . . . .	124
Figure 57	Route discovery time. . . . .	126
Figure 58	Route examples of SISO-based scheme and OLA-PRISE. . . . .	129
Figure 59	OLAROAD route example. . . . .	130
Figure 60	Flow chart of routing selection . . . . .	134
Figure 61	Illustration of local ganging for OLA-PRISE . . . . .	135
Figure 62	Average node degree $\kappa$ . . . . .	137
Figure 63	Average end-to-end latency $L$ . . . . .	139
Figure 64	Average throughput $\eta$ . . . . .	139
Figure 65	Average number of nodes in route $N_{\text{node}}$ . . . . .	140

Figure 66	Illustration of the spatially pipelined OLA transmission in infinite strip network . . . . .	154
-----------	---	-----

## SUMMARY

The objective of this dissertation is to better understand the impact of the range extension and interference effects of opportunistic large arrays (OLAs), in the context of cooperative routing in multi-hop ad hoc networks. OLAs are a type of concurrent cooperative transmission (CCT), in which the number and location of nodes that will participate in a particular CCT cannot be known a priori. The motivation of this research is that the previous CCT research simplifies or neglects significant issues that impact the CCT-based network performance. Therefore, to develop and design more efficient and realistic OLA-based protocols, we clarify and examine through experimentation and analysis the simplified or neglected characteristics of CCT, which should be considered in the network-level system design.

The main contributions of this research are (i) intra-flow interference analysis and throughput optimization in both disk- and strip-shaped networks, for multi-packet OLA transmission, (ii) CCT link modeling focusing on path-loss disparity and link asymmetry, (iii) demonstration of CCT range-extension and OLA-based routing using a software-defined radio (SDR) testbed, (iv) a new OLA-based routing protocol with practical error control algorithm. In the throughput optimization in presence of the intra-channel interference, we analyze the feasibility condition of spatially pipelined OLA transmissions using the same channel and present numerical results with various system parameters. In the CCT link model, we provide the impact of path-loss disparity that is inherent in a virtual multiple-input-single-output (VMISO) link and propose an approximate model to calculate outage rates in high signal-to-noise-ratio (SNR) regime. Moreover, we present why link asymmetry is relatively more severe in CCT compared to single-input-single-output (SISO) links. The experimental studies show actual measurement values of the CCT range extension and realistic performance evaluation of OLA-based routing. Lastly, OLA with primary route set-up (OLA-PRISE) is proposed with a practical route recovery technique.

# CHAPTER 1

## INTRODUCTION

In wireless communication, multi-antenna technologies have been extensively studied because of their ability to enhance channel capacity in fading channels. Moreover, aside from the theoretical performance analysis, various wireless standards have adopted the multi-antenna techniques in actual wireless devices. As an extended concept of the conventional multi-antenna communication, where a single node is equipped with multiple-antenna array, cooperative transmission (CT), in which spatially separated wireless nodes collaborate to form a virtual antenna array, is an effective physical layer scheme to mitigate multi-path fading by spatial diversity.

CT has attracted considerable research interest in recent years, because this technique can enhance system performance through both micro and macro diversity of CT by its distributed nature in space in various wireless network architectures such as wireless sensor networks (WSNs), multi-hop wireless networks (MWNs), and mobile ad-hoc networks (MANETs). For this reason, there are various efforts to adopt CT in mainstream wireless communication standards such as coordinated multi-point transmission (CoMP) in Long Term Evolution-Advanced (LTE-Advanced) [4].

This research is focused on analysis and experimentation of one type of CT known as concurrent cooperative transmission (CCT). In CCT, cooperating nodes transmit multiple copies of the same message at approximately the same time through orthogonal channels, and a receiver achieves a signal-to-noise-ratio (SNR) advantage by combining the copies of the signals. The objective of this research is to analyze and develop algorithms that can effectively use the SNR advantage of CCT in broadcasts and unicasts for multi-hop wireless networks. However, while there have been various efforts in the physical layer research on CCT, the network-scale protocol design and performance evaluation still need much more development before the practical implementation. For this reason, this dissertation

identifies a gap between the conventional theoretical or simulation-based studies of CCT and practical implementation. Specifically, we introduce important issues that have not been considered properly in the conventional research such as intra-flow interference, path-loss disparity, and link asymmetry. Then, we propose more practical algorithms that reflect the issues based on experimental results.

CCT-based broadcasts and unicasts are known to be fast, reliable, power-efficient, and resistant to network-partition problems [5]. However, while most of these benefits are derived from range-extension property of CT, one negative aspect of the range extension is increased interference. The existing studies on CCT do not consider this increase in interference caused by collaborative transmissions of multiple nodes. Instead, the existing studies on CCT consider only a single-shot CCT transmission of a single packet, which suggests that the range extension of CCT is always desirable. On the other hand, if multiple packets are transmitted, for example, if video data needs to be transmitted over a multi-hop network, then network throughput becomes important. When multiple packets within a single data flow are transmitted using the same channel, any one packet transmitted in the network suffers from co-channel interference from the other packets propagating in the same flow, which is referred to as “*intra-flow interference*.” The first contribution of this research is to provide a theoretical analysis of the intra-flow interference in CCT for throughput maximization in a particular form of CCT called Opportunistic Large Arrays (OLAs), in which a group of nodes decode the same packet and then a short time later relay the packet simultaneously in orthogonal channels.

Moreover, the previous CCT studies oversimplify the virtual multiple-input-single-output (VMISO) link model to facilitate their network-scale analysis. To be specific, multiple nodes that create a VMISO link are approximated into a co-located multi-antenna array, which ignores disparate path losses from multiple nodes to a single receiver. In this dissertation, we present the error of this *co-located approximation* and propose a simple model that captures the dissimilar path losses in CCT. Second, as the important aspect of

higher layer protocol design, link asymmetry that inherently appears in VMISO links is presented. Because bidirectional links are commonly assumed in many ad hoc network routing or medium access control (MAC) algorithms, link asymmetry can significantly degrade the higher layer performance metrics. However, the link asymmetry issue has not been considered in the existing studies that make the co-located approximation, even though link asymmetry between two consecutive VMISO links is significantly higher than the conventional non-CT networks.

Also, even though CCT is applied to various applications such as broadcasting, routing, and energy balancing, few experimental studies about CCT are reported in the literature. Instead of experiments on real testbeds, most of CCT-based algorithms are evaluated only by theoretical analysis and simulation results, because commercial off-the-shelf radios do not support the signal combining capability required for CCT. Motivated by this fact, the third part of this research consists of two experimental studies using a software-defined radio (SDR) testbed. First, as the key feature of the CCT-based protocol design, the range extension of CCT is investigated by measurement and simulation. In the second experimental study, a routing protocol based on OLA transmission is compared with the Ad-hoc On-demand Distance Vector Routing (AODV) protocol that operates on a conventional single-input-single-output (SISO) physical layer.

Motivated by the experimental results, in the last chapter of this dissertation, we develop an efficient OLA-based routing to build a multi-hop path for unicasting between a random source and destination pair. In [6], the key routing protocols in ad hoc networks are divided by three categories: flat, hierarchical, and geographic position assisted routing. In the flat routing schemes, all the nodes play an equal role with a same addressing format, while hierarchical protocols aim to cluster the nodes so that cluster heads can do some aggregation and reduction of data. Geographic position assisted protocols utilize position information with the Global Positioning System (GPS). In this dissertation, we assume all the nodes except the sink have the same hardware capability, so that the network administrator can

operate the network with high flexibility. For this reason, we are mainly interested in the flat routing that includes AODV and DSR (dynamic source routing). Also, considering the overhead caused by proactive schemes, we are interested in “reactive (on-demand)” routing. In other words, we consider an OLA-based routing scheme that constructs a route between an arbitrary source and destination pair on demand by broadcasting route request (RREQ) packets. For practical protocol design, we investigate the possible issues for error control and medium access schemes for OLA-based routing. Finally, we propose an efficient way to operate OLA-based routing with a technique to prevent frequent transmission errors.

## CHAPTER 2

### ORIGIN AND HISTORY OF THE PROBLEM

In this chapter, we review some of the related research topics and make common definitions and assumptions. In Section 2.1, we overview opportunistic large array (OLA)-based transmission and discuss distinction between single-packet (i.e., single-shot) and multi-packet scenarios. Also, OLA broadcasting is introduced in Section 2.1.1 with the existing non-CT and CT multi-hop broadcasting methods. Moreover, as an idealized cooperative route model, OLA transmission in strip networks is explained in Section 2.1.2. Second, in Section 2.2, we review the existing cooperative transmission link models and their limitations, focusing on path-loss disparity and link asymmetry. In Section 2.3, we will introduce the motivation of the experimental studies in this dissertation. Lastly, in Section 2.4, we review the existing CT-based routing schemes with error control algorithms.

#### 2.1 Multi-packet OLA Transmission and Intra-flow Interference

The classical relay channel model consists of three nodes as shown in Fig.1: Source first transmits a message, and Relay receives the message from Source and forwards to Destination. Therefore, communication between Source and Destination is enhanced by combining two copies of the same message from Source and Relay at Destination. In contrast, we are interested in scenarios, wherein Source and Destination are far away from each other, as shown in Fig.2, where channel capacity of the direct link between Source and Destination is limited by the high path loss. For this reason, Source first transmits to multiple relays, then

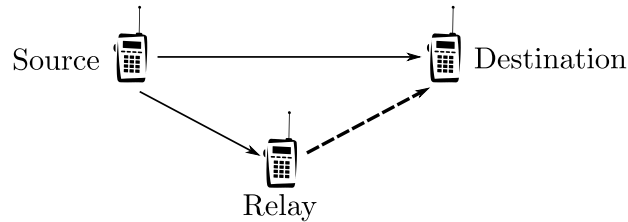


**Figure 1:** Three-nodes cooperative transmission model



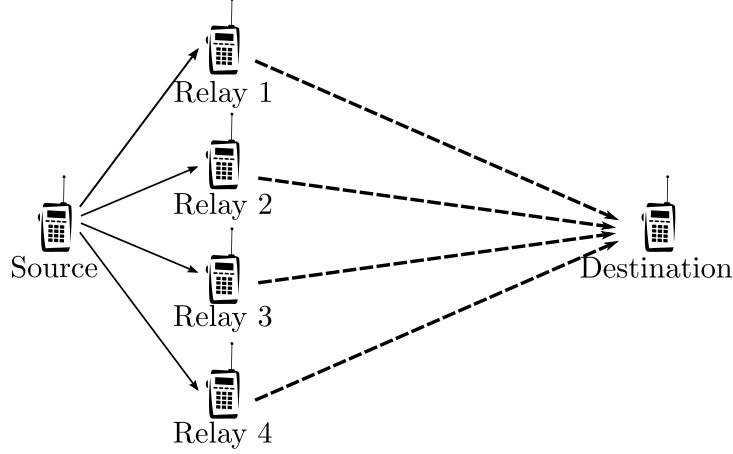


**Figure 2:** Concurrent cooperative transmission (CCT) model

the multiple relays forward the received message to Destination at approximately the same time using diversity channel, which is called concurrent cooperative transmission (CCT). To be specific, CCT is a physical layer technique, wherein multiple physically separated radios transmit multiple copies of the same message over independently fading diversity channels to a receiver that combines the copies. The combining provides a signal-to-noise ratio (SNR) advantage to the receiver through array and diversity gains [7,8]. Array gain is the improvement in the average received SNR [8]. Even if array gain is cancelled by reducing the transmit powers, there will still be diversity gain in randomly fading and shadowed channels by reduction of probability of outage [7,8]. One form of CCT is the Opportunistic Large Array (OLA), where groups of relays are formed without coordination by each relay's successful decoding of a message from a single source or another OLA [9]. The diversity channels can be formed using orthogonal waveforms [10], distributed space-time block codes [11], or phase dithering [12]. Practical OLA transmission has been demonstrated by the authors [13]. OLA-based broadcasts and unicasts are known to be fast, reliable, power-efficient and less susceptible to network partitions [5]. However, while most of these benefits are derived by the range extension property of CCT, one negative aspect of range extension is increased interference. For example, if multiple packets are transmitted using the same channel, each packet suffers from co-channel interference from the other

packets propagating at the same time. In this dissertation, we investigate this “*intra-flow interference*” of the OLA transmission, which is generated by multiple OLAs transmitting different packets from the same source and heading for the same destination within a single flow.

However, most studies of multi-hop OLA transmission do not consider the interference between co-channel packets in a multi-packet transmission, such as would occur in video or large file transfers. Instead, they consider just a one-shot transmission of a single packet, which fully utilizes the range extension property of CT. However, if more than just a single packet should be transmitted, for example, if video data needs to be broadcasted over a tactical mobile ad hoc network, then broadcast throughput becomes important. This dissertation examines the “intra-flow interference” caused by multiple OLAs transmitting different packets from the same source (a single flow) at the same time. We do not consider “inter-flow interference” that would be caused by transmissions from different sources.

To our knowledge, only two other research groups have addressed OLA transmissions of multiple packets. The authors of [12] proposed to insert multiple packets into the network with a fixed period as with conventional single-input-single-output (SISO) multi-hop transmissions. They argue that large inter-packet separation can be chosen to trade throughput for enhanced robustness to topological variation, but the impact of the increased intra-flow interference by CT is not investigated in detail. In their recent work in [14], they only consider “inter-flow” interference caused by different flows using the protocol interference model in [15], where the interference is assumed to be zero, if the interfering node is outside of a certain range. Because they assume the protocol interference model with a constant inter-packet separation, the intra-flow interference from a large number of nodes far from the receiver is not considered.

Therefore, to our knowledge, only one paper [16] treats intra-flow interference in multi-hop OLA transmission. The OLA broadcasting in [16] assumes perfect interference cancellation of interference from preceding packets, and analyzes the effects of the interference

from the following packets. However, for some types of networks such as sensor networks, constraints on node processors and memory may preclude interference cancellation. Also, the presence of multiple time and frequency offsets of cooperators may make channel estimation very challenging [17]. Therefore, we assume that none of the interference is cancelled. Moreover, while the authors in [16] analyze the broadcast capacity from an information theoretical point of view, we focus on the packet-level analysis following [18], in which the inter-packet separation is minimized to maximize the throughput.

There are three network models in the existing studies on OLA: ‘disk’, ‘strip’, and ‘line’ networks. While the disk networks model the multi-hop broadcasts in a large area by concentric rings as in [19] and [20], the strip networks characterize multi-hop unicasts using a cooperative route or multi-hop broadcasts using wireless nodes deployed in strip-shaped structures such as on roadways, bridges, and tunnels as in [21] and [22]. The disk and strip network models differ significantly in terms of the sizes and shapes of OLAs, as a function of hop number. For the single-shot (i.e., single-packet) transmission, the OLAs in the disk-shaped networks form concentric rings, and their areas generally grow exponentially with hop-count [19]. In contrast, the OLA step-sizes of the strip-shaped networks converge to a certain value, as the hop-count increases [21]. Different from the disk and strip networks, the research on line networks in [23] and [24] apply quasi-stationary Markov processes to study single-shot OLA transmission down an infinitely long line of nodes that can only exist in equally spaced positions [23, 24]. However, because of matrix size limitations, that work has not been extended to strip networks with width.

### **2.1.1 Broadcasting in Wireless Multi-hop networks**

The subject of broadcasting in multi-hop wireless networks has attracted the attention of many researchers over the years [25], and there are a number of popular techniques, such as flooding [26], the Probabilistic, Counter, and Location based schemes [27], and broadcast trees [28, 29]. Broadcasts that carry routine vehicle state information and emergency messages have inspired some new broadcast protocols for multi-hop in vehicular ad hoc

networks (VANETs) [30,31]. All of these methods rely on links between a single transmitter and a single receiver.

In contrast, some broadcasting schemes exploit cooperative transmission (CT), in which multiple single-antenna radios gang together to send the same message in independently fading channels so that a receiver can derive a signal-to-noise-ratio (SNR) advantage through diversity combining [7, 32]. This class of schemes includes different ways to create diversity channels, such as orthogonal waveforms [10], distributed space-time block codes [11], or phase dithering [12]. Any of these diversity methods can be used with the opportunistic large array (OLA) [9]. An OLA is formed when a group of radios that all decode the same packet next relay that packet at approximately the same time, as a virtual array. In an OLA broadcast, OLAs are formed in succession, as a new group of nodes are able to decode the OLA transmission from the previous group, forming ever-growing ring-shaped OLAs [19]. The OLA broadcasts are known to be fast and reliable, and able to overcome voids that would cause partitions in networks that do non-cooperative transmission [5]. Because no topology information must be stored, OLA broadcasting is especially attractive for highly mobile networks [33]. The OLA broadcast has also been proposed as the route-request step in two reactive OLA-based unicast routing protocols [12, 13, 33, 34].

### **2.1.2 OLA Transmission on Strip-shaped cooperative Routes or Networks**

We also consider multi-packet OLA transmissions down a “strip” of finite width, such that the nodes are densely and randomly distributed over the strip. The primary motivation for studying this type of node distribution is that it is an idealization of a cooperative route through a large multi-hop network. Such a route can be formed many ways. It is the direct result of the route request (RREQ) and route reply (RREP) of the OLA-based protocols, OLAROAD [13], OLACRA [5], and CBR [35]. However, a strip-shaped route could also be formed using the set-up phase of a conventional shortest-path routing protocol, such as AODV [36], by defining the cooperative route as *all* the nodes that can *decode (or overhear)* the RREP message for a particular source-destination pair, or that can decode Hello

messages sent by nodes on the primary (conventional) route. Or, the route can be formed geometrically assuming each node knows its geographical location (e.g., from GPS) [37]. Regardless of how the cooperative route is created, the Data-transmission phase can follow the method described in this dissertation, to achieve low latency and reliable packet transfer [13]. As stated earlier, there are also a number of applications for which the multi-hop network would just happen to have a strip-shape, such as vehicular networks on roadways or the structural health monitoring networks for bridges and tunnels [38]. One can also imagine a futuristic piece of plastic tape, with embedded radios on it, that could serve as a non-conducting “*communication cable*” [39]. The more confined geometry of the strip network gives different OLA propagation characteristics, compared to the disk. For example, for single-packet transmission, the OLA sizes approach a finite value with hop-count [21] in the strip networks, while OLAs might grow exponentially in the disk networks [5].

## 2.2 Cooperative Transmission Link Model

For small wireless nodes with limited power, where collocated antennas (a real antenna array) cannot be deployed, cooperative transmission (CT) is an alternative way to achieve spatial diversity in fading channels [40, 41]. CT provides an SNR advantage through array and diversity gains by creating a virtual multiple-input-single-output (VMISO) link that connects a transmitting cluster (multiple nodes) with a single receiver node. Based on the SNR advantage of CT, various higher layer protocols have been proposed, in which the VMISO links provide gains at higher layers such as throughput improvement, energy saving, energy balancing, and range extension [1, 5, 42, 43].

In multi-hop ad hoc networks, the CT-based protocols are divided into decentralized and centralized architectures, depending on how the cooperative clusters are activated and supported [44]. In the decentralized architecture such as [5, 35, 45, 46], the cluster is activated randomly in a distributed manner, where all the nodes in a cluster have the equal role. On the other hand, in the centralized cluster architecture, which has a cluster-head in each

cluster, the cluster-head recruits its cooperators and triggers the group transmission to the cluster-head in the next cluster [1, 11, 42, 43, 47, 48]. Because the member nodes follow their cluster heads' decision and the cluster size can be readily controlled, a cluster can work as a single node. Therefore, the centralized cluster architecture guarantees high compatibility to the conventional non-CT or single-input-single-output (SISO)-based systems.

In network layer research using CT, two abstraction models of the VMISO link are widely used to deal with random topologies in the network-scale analysis and simulations. In the decentralized CT architecture, *continuum approximation* in [19] and [5] is frequently used assuming high node density. In the continuum approximation, the number of nodes is assumed to be infinity, while the transmit power of each node becomes infinitesimally small. On the other hand, *co-located approximation* model, where physically separated cooperating nodes in a cluster are simplified to be a single node with a multiple-antenna array, appears in the centralized architecture CT studies in low node density as in [1, 42, 43, 48]. In this co-located approximation model, the disparate path losses caused by the different distances between the transmitting nodes in a cluster to the receiver node are ignored. The authors in [49] realized through simulation of some specific topologies that there can be a significant error (i.e., SNR penalty) incurred for making the co-located assumption.

### **2.2.1 Outage Probability of a Virtual Multiple-Input-Single-Output (VMISO) Link**

Beaulieu et al. [41] derived a closed-form expression for the outage probability at the destination for decode-and-forward (DF) relays, where the location of the relays are assumed known. [41] has an intermediate result, where the number of relays that successfully decode is assumed known, while the final result in [41] allows for the opportunistic case, where the number of relays that successfully decode is not known a priori. However, this final expression in [41] is long, complicated, and numerically sensitive [40]. Moreover, the SNR penalty for the co-located assumption is not considered in [41], nor are random locations of nodes taken into account.

In this dissertation, we allow the node locations to be random. For the known number

of successfully decoding relays in multi-path fading channels, we show that the random locations of nodes produces a fading-averaged received power with a log-normal distribution, as in shadowing. We also derive a lower bound based on assuming error-free source-relay links. We also treat the opportunistic case and derive an upper bound for the case when the number of relays that successfully decode is not known a priori by assuming the first-hop errors are independent and identically distributed (i.i.d.). These bounds provide the best and worst case SNR penalties for the co-located assumption. To our knowledge, this is the first study that models the SNR loss due to the random path-loss disparities in the VMISO links.

### **2.2.2 Link Asymmetry of a Virtual Multiple-Input-Single-Output (VMISO) Link**

We are interested in the link asymmetry of VMISO, where the link asymmetry has been neglected by co-located assumption in the previous studies. By “link asymmetry,” we mean a significant difference between the forward and reverse link performance; in an extreme case, a link that should be bidirectional is rendered unidirectional. Link asymmetry adversely affects routing in ad hoc networks, because it causes many routing protocols and link-layer schemes (e.g., AODV and CSMA/CA) to work inefficiently [50]. Similarly, many VMISO-based protocols with the centralized cluster architecture such as [1, 42, 43] require bidirectional links, because such protocols are modified versions of the conventional single-input-single-output (SISO)-based schemes that assume bidirectional links.

In the conventional SISO-based network, link asymmetry is caused by transceiver hardware difference, uneven transmit power control, and noise or other signal propagation phenomena [51]. For VMISO links, we focus on sources of link asymmetry that do not appear in SISO links; we assume the other factors are excluded by calibration. Therefore, in case of time-division duplex (TDD), which is more widely used than frequency-division duplex (FDD) for link-layer signaling (e.g., RTS-CTS-DATA-ACK in *IEEE 802.11* [52]), the forward and reverse channels are typically assumed to be equal with frequency nonselective block fading [53]. On the other hand, the VMISO-based networks inherently suffer

from the link asymmetry because each VMISO link consists of multiple SISO links from different transmitters to a single receiver.

Because of the overhead and the implementational complexity of cooperative reception [8], most of the CT-based protocols let each node at the receive cluster individually decode its own received signal. Therefore, if looking at the forward and reverse VMISO links between two neighboring clusters with the centralized architecture, the cooperative relays in each cluster are only used for transmission, while a cluster head exclusively decodes the received signal from the other cluster. Thus, considering that multiple SISO links make a single VMISO link, the reverse and forward VMISO links have only one common SISO link, which is between the two cluster heads. On the other hand, the other SISO links between the cooperators in one cluster to the cluster head in the other cluster have independent channel characteristics, because cooperative relays in a cluster impact only on the *transmit* channel to the other cluster. In addition, the link asymmetry of the two VMISO links is more severe than the co-located model, because physically separated relays make disparate path losses depending on their locations. Considering these two factors (exclusive signal reception by cluster heads and path-loss disparity), this dissertation explores the forward-reverse link asymmetry between two CT clusters, while excluding the other factors (e.g., hardware, transmit power, and irregular signal propagation). To our knowledge, there has not been a study about this link asymmetry problem in the VMISO-based networks.

### **2.3 Experimental Studies on CCT**

For precise evaluation of CCT-based broadcasting and unicasting protocols, the models obtained from measurements are essential to compare the CCT-based schemes with the conventional non-CT algorithms. However, while several experimental studies are reported in the other types of CT, very few demonstrations of CCT with practical synchronization have been reported [54]. Therefore, systematic experimental studies about the range extension and the CCT-based routing with comparison to the conventional non-CT-based schemes are



presented in this research.

## 2.4 OLA-based Routing and Error Control Algorithms

Existing CT-based routing schemes can be divided into two categories: schemes that build the CT route around a single-input-single-output (SISO) primary route, and all-OLA routing schemes, which use OLAs in every phase of the protocol. The SISO primary route-based schemes in [1, 42, 55] first construct a conventional SISO multi-hop route as the primary route. Then, the nodes in the primary route collect cooperators to create VMISO links. On the other hand, the all-OLA routing algorithms in [5] and [35] build a route using end-to-end handshake of RREQ and RREP in CT, which is not limited by the existence of non-CT route. In other words, if there were a network partition that blocks SISO transmissions, the non-CT routing scheme would fail, but all-OLA scheme might still be able to form the route.

The main advantage of the all-OLA routing schemes in [5, 35] is that they fully utilize the wireless broadcast advantage and the cooperative range extension in every phase, including route set-up, so their routes are not limited by the existence of the conventional non-CT route. In other words, if there were a network partition that blocks SISO transmissions, the non-CT routing scheme would fail, but the all-OLA schemes might still be able to form the route. In our research group, we developed an all-OLA routing scheme called OLA Routing On-Demand (OLAROAD), as described in Section 7.2.1. The Controlled Broadcast Region (CBR) in [35] is basically the same OLA-based routing algorithm using Barrage Relay Network (BRN) [12]. However, as we will explain in the demonstration results, the shapes of the OLAs in the all-OLA routing schemes are difficult to control in practice.

On the other hand, with a cluster head in each VMISO hop, the primary route-based schemes are more compatible with the conventional SISO-based network architectures. For example, in [1], each link has a single and deterministic receiver to detect the error, while

the all-OLA routing schemes decide the hop membership (i.e., hop count of each node) on the fly. However, in this case, the wireless broadcast advantage is limited, because only the cluster head tries to decode without any opportunistic reception by the other nodes in the cluster. For this reason, in Chapter 8, we propose a new OLA-based routing scheme with a primary route set-up that provides more efficient in terms of numbers of nodes participating than OLAROAD, while keeping the wireless broadcast advantage by using OLAs for data packet transmission.

### **2.4.1 Reliability and Error Control**

The demonstration of OLAROAD presented in Section 7.2 showed the need for an error-control algorithm. To be specific, when node degree is low, the packet delivery ratio (PDR) of OLAROAD is lower than the non-CT routing scheme, AODV, because AODV has an error-control scheme with retransmission, while OLAROAD does not. For this reason, we became interested in developing an error control scheme for our OLA-based routing schemes.

In this section, we define related technical terms and explore general error control approaches in different layers. Depending on the layer in which it is implemented, error control can operate on an end-to-end basis or over a shorter span, such as a single link [56]. Transmission Control Protocol (TCP) is the most important example of an end-to-end protocol that uses an automatic repeat request (ARQ) strategy.

#### *2.4.1.1 Automatic Repeat Request and FEC*

The main idea of error recovery is to use redundant information computed from the original data. Depending on the size of the redundant information and how it is generated, the receiver can use it to reliably detect transmission errors, correct up to some maximum number of transmission errors, or both. The general approach using this redundant information is known as error control coding (ECC). When a transmission error is detected by ECC, retransmission can be requested, which is widely known as ARQ.

When enough ECC information is available for the received to correct some transmission errors without a retransmission, the approach is known as forward error correction (FEC). Because its complexity and dependencies on a specific modem and channel, FEC has traditionally been implemented in the physical layer.

#### 2.4.1.2 *Link-layer ARQ and end-to-end ARQ*

We are mainly interested in the error control algorithms implemented above the physical layer for CT-based routing protocols. In other words, we limit our scope to ARQ in the link and path (end-to-end) levels. Many link-layer protocols use ARQ (e.g., X.25, AX.25, IEEE 802.11, and IEEE 802.2) as described in [56]. Link-layer ARQ is designed as *best-effort* service, and only end-to-end error recovery can guarantee reliable service to the application.

However, end-to-end error control without link-layer error recovery may degrade network performance, because retransmissions across the end-to-end path take much longer than link-layer error control. Therefore, link-layer and end-to-end ARQs often co-exist, especially when frame loss rates are high. For this hybrid recovery using both link-layer and end-to-end ARQs, efficient interaction between the two layers is required not to cause unnecessary and independent reactions to each other (e.g., packet losses and retransmissions on the link layer are interpreted as congestion by TCP).

#### 2.4.2 **Existing Medium Access and Error Control for CT-based Routing**

In this section, we present the existing medium access control and error control (ARQ) algorithms that are designed for cooperative networks. How to access the shared channel (MAC) is closely related to the error control algorithm (ARQ). The MAC and ARQ algorithms in the literature are divided into two: link-based and path-based. The CT algorithms with deterministic membership, where each cluster is controlled by a single cluster head as in [1], “link-level MAC and error control algorithms are used. On the other hand, if the random membership is allowed (e.g., OLAROAD and CBR in [12]), the channel is reserved

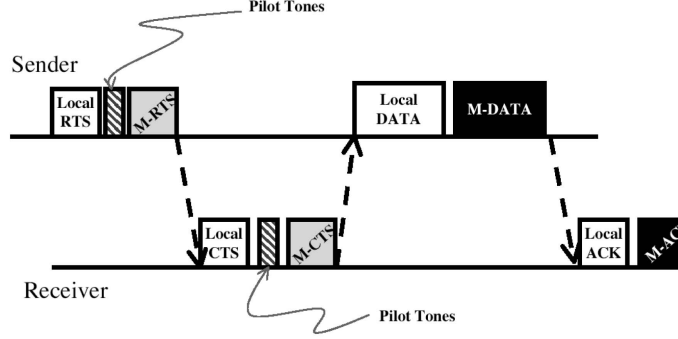


**Figure 3:** The sequence of packet transmission on a virtual MISO link in [1]

on a path basis.

#### 2.4.2.1 Link-level MAC and ARQ

The authors in [1] propose an 802.11-like MAC as shown in Figure 3. In the figure, the functions of M-RTS, M-CTS, and M-ACK are same as RTS, CTS and ACK in the conventional non-CT networks except they are transmitted by the virtual MISO links. The local RTS, local CTS, local DATA, and local ACK are transmitted by the cluster head. These local control messages are sent to the cooperators, then this local transmission is repeated with the cooperator in the virtual MISO mode for M-RTS, M-CTS, M-DATA, and M-ACK. The pilot tones between the “local and “MISO control messages are for the channel estimation purpose at the receiver.

#### 2.4.2.2 End-to-end-based MAC without ARQ

In [2], the authors propose an end-to-end-based MAC called Cooperative Path Access Control (PAC), as shown in Figure 4. This PAC reserves the channel over the full-path from the source and the destination instead of the channel reservation in a link (or hop) basis. In this PAC, the source and destination access the channel by CSMA/CA to send RTS and CTS, respectively. However, the ARQ is intentionally excluded, because the retransmission is difficult to handle in path-based channel access, since the source inserts a new packet periodically by time division multiple access (TDMA).

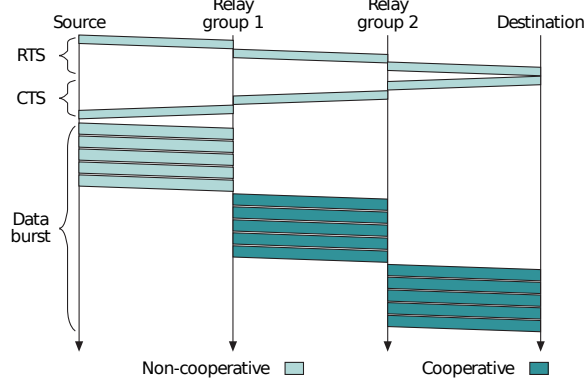


**Figure 4:** Path Access Control (PAC) in [2]

CBR in [35] also uses a path-based channel reservation with TDMA multi-hop scheduling. Their MAC scheme called Barrage Access Control (BAC) has two control packets: RTS and CTS, which are identical to RREQ and RREP in our OLAROAD. The collision between multiple flows is handled by the random back-off of RTS transmission at the source. Each transmitting node in a BRN pseudo-randomly dithers its carrier phase, then the superposition of these signals will introduce a time-varying channel characteristic at a receiver node. A modern error correction code is used to extract the time diversity provided by this time-varying fading channel. However, CBR does not specify any ARQ algorithm.

#### 2.4.2.3 Segment-based MAC with ARQ

As a modified version of [2] with the same name, Path Access Control (PAC) in [3] is a mechanism that reserves the channel for multiple hops, namely a “segment.” The entire source-destination path is composed of multiple segments. In other words, a segment, which consists of consecutive multiple hops, is a subset of the source-destination path. Figure 5 shows an example of their PAC, where two source-destination pairs exist (s1-d1 and s2-d2). In this example, the source s1 that wants to transfer a burst of data to the destination d1, first sends a Segment Access Request (SAR), which is relayed to d2 until it encounters an ongoing transfer. The PAC in d1 replies with a Segment Access Clear (SAC), which again relayed to s1. The SAR and SAC can be regarded as multi-hop RTS and CTS.

Upon receiving the SAC, a data burst is transmitted from s1 to d1. In [3], the author

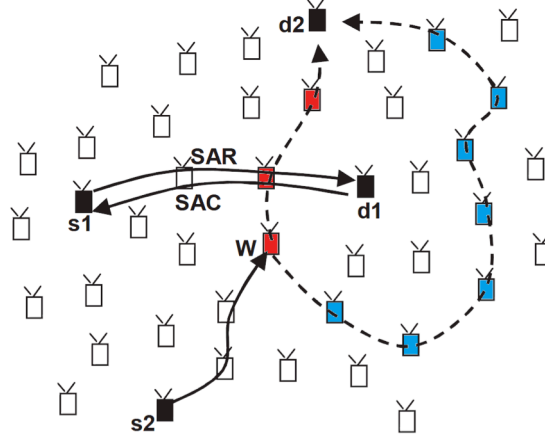


**Figure 5:** The sequence of packet transmission on a virtual MISO link in [3]

mentions the feedback (acknowledgement): an acknowledgement may be sent, or we may simply let the transport layer take care of reliable delivery. In other words, the PAC in [3] does not specify their ARQ algorithm, but if they use one, the ARQ will be implemented in an end-to-end manner

#### 2.4.2.4 Error Control Algorithms for OLA-based Routing

Link-layer error control is extremely challenging for the all-OLA routing schemes (e.g., OLAROAD and CBR), because the time required for gaining consensus within the nodes of an OLA is long and uncertain and complicates the timing of a link-layer error control algorithm. For example, suppose there is an OLA transmission and at least one node in the next-hop region correctly received the packet. In this case, no retransmission should be initiated among OLA nodes. If some of those nodes are not informed about the success of the transmission, then they may attempt to launch a retransmission. Therefore, the nodes within an OLA must reach a consensus that no retransmission is needed. While there exist methods for ad hoc networks of nodes to reach consensus, these methods require many packet exchanges and take a long time. Alternatively, if one node within the OLA could be designated a cluster head, it could have the responsibility for making the retransmission decision. However, designating a cluster head within the OLA is not trivial since OLA memberships are not known a priori.

## CHAPTER 3

### ANALYTICAL FRAMEWORK FOR INTRA-FLOW ANALYSIS

The theoretical framework used to analyze the intra-flow interference in OLA-based transmission is described in this chapter. Half-duplex nodes with decode-and-forward (DF) are assumed to be uniformly and randomly distributed with average density of  $\rho$ . Assuming a single flow, the originating node is a point source in a two-dimensional space. In multi-hop OLA transmissions, when a node receives a packet, it forwards the packet only when the decoding is successful and the node has not transmitted the packet before [9].

As in [19] and [21], let  $P_s$  and  $P_r$  denote the fixed transmit powers from the source and relay, respectively. For simplicity, we assume the unit noise power as indicated by  $N = 1$  as in [19] and [21], without loss of generality. In this dissertation, we consider the received signal-to-noise ratio (SNR) in the absence of the interference and the received signal-to-interference-plus-noise ratio (SINR) in the presence of the interference. Therefore, we can apply the results with the unit noise power  $N = 1$  to general cases  $N \neq 1$  by adapting the transmit powers  $P_s$  and  $P_r$ , accordingly. In other words, the two system parameters  $P_s$  and  $P_r$  are the transmit powers normalized by the noise or noise plus interference power. Moreover, even in the presence of the interference, the analysis based on the SINR can be generalized in the same manner, because we assume the same transmit power  $P_r$  for all the nodes except the source, the transmit power of which is  $P_s$ . By the unit noise power assumption, the received power denoted by  $S$  can be used interchangeably with the received signal-to-noise ratio (SNR), which is defined as  $S/N$ . To calculate the received power, when  $(x, y)$  is the location of a receiver relative to a transmitter in Cartesian coordinates, for a path loss exponent of  $\alpha$ , the path loss function is defined by  $l(x, y) = \frac{1}{(x^2 + y^2)^{\alpha/2}} = \frac{1}{d^\alpha}$ , where  $d = (x^2 + y^2)^{1/2}$  [19, 21]. In the absence of the interference, the decoding is assumed to be correct if the received SNR is greater than or equal to a certain threshold  $\tau$  determined by the modulation and coding [19]. A low threshold  $\tau$  implies a low data rate [21] or

a power-efficient waveform such as frequency-shift keying (FSK) [57], because the nodes are required to decode with low received SNR, which means decoding needs to be less demanding. On the other hand, the higher  $\tau$  implies the higher data rate or bandwidth-efficient waveforms, such as quadrature amplitude modulation (QAM) [57], which require high enough SNR in the absence of the interference (or SINR in the presence of the interference). Therefore, as a minimum requirement for large file transfer applications with bandwidth-efficient waveforms as suggested in [57], we are interested in  $\tau \geq 1$ , which means the ratio of  $\mathbf{S}$  to  $\mathbf{N}$  should be greater than or equal to one.

### 3.1 Deterministic Channel and Continuum Assumptions

For the multi-hop network analysis with a large number of nodes doing CT, we make the deterministic channel and continuum assumptions, as in [19–22] and [16], which allows simpler analysis, but is accurate enough for multi-hop OLA transmissions with high node density, as shown in [19] and [21]. In various studies on CT as in [1, 42, 43], multiple CT transmitters that are physically separated in space are approximated into a single node with multiple-antenna array, which is called *co-located approximation*. However, this co-located approximation causes a significant error especially for the high node density situation as shown in [49] and [58], because this model ignores the disparate path losses from the multiple transmitters to a receiver in a virtual multi-input-single-output (MISO) link of CT.

For this reason, following [19] and [21], we make the “continuum assumption,” which is an accurate model of “finite but high” density networks including path-loss disparity in CT as shown in [19] and [5]. In this continuum model, the node density becomes very large (i.e.,  $\rho \rightarrow \infty$ ), while the relay transmission per unit area, which is denoted by  $\overline{P_r} = \rho P_r$ , is held constant. We refer to this particular limit in the sequel as the “*continuum limit*.” Also following [19] and [21], we assume the deterministic channel model, which assumes that the power received at a node is the sum of the powers from each of the transmitting nodes. With the two (deterministic channel and continuum) assumptions, the received



power from a group of transmitting nodes  $\mathbb{O}$ , which is originally expressed as  $\sum_{j \in \mathbb{O}} P_r \cdot l(d_j)$  by the deterministic channel assumption, can be approximated into an integral form as  $\iint_{\mathbb{O}} \overline{P_r} \cdot l(d) dA$ , where  $A$  is the area of  $\mathbb{O}$ . Therefore, the SNR at a receiver at a distance  $z$  from the origin, receiving power from a disk-shaped OLA of radius  $r$ , centered at the origin, such that  $r < z$ , is  $f(r, z) = \int_0^r \int_0^{2\pi} \overline{P_r} \cdot l(r \cos \theta - z, r \sin \theta) r dr d\theta$ , where  $(r, \theta)$  is the transmitter location in polar coordinates.

Since the “sum of powers” property is based on the assumption of every relay transmitting in an orthogonal diversity channel, and in the limit of the continuum, the number of relays goes to infinity, we seem to be assuming infinite bandwidth. However, in practice, only a finite number of orthogonal diversity channels are used, and if these channels are allocated uniformly, then the number of channels is the diversity order. Furthermore, as the diversity order grows, the increase in diversity gain diminishes [59], corresponding to an effective reduction in fading in the SNR after combining. Therefore, our assumptions apply to networks with high node densities and a high number of diversity channels. For example, the authors in [5] show that packet delivery ratio (PDR) of the flat fading channel with a finite node density ( $\rho = 2.2$ ) gets closer to the results based on the “sum of powers” property with the deterministic channel assumption, as they increase the number of diversity channels from one to four. Similarly, in [60], the simulation results of the probability of successful broadcast (PSB) that assumes uniformly and randomly distributed nodes with  $\rho = 10$  in Rayleigh fading channel show an excellent match with the analysis based on the deterministic channel assumption, as the number of diversity channels increases from one to three. Moreover, we note that it may be possible to get the same performance with better bandwidth efficiency by using distributed orthogonal space-time codes in [32] instead of orthogonal-frequency or orthogonal-time diversity channels for relays.

It follows from a finite number of diversity channels, that one could assign orthogonal channels for consecutive packets (i.e., simultaneously using different OLAs), which would eliminate the intra-flow interference. However, similarly to the diversity channel allocation

to the multiple nodes in an OLA, the number of the channels assigned to the multiple OLAs would be limited in practice. Therefore, if a large file were being transmitted over a large multi-hop network, channels may need to be reused, in which case, the results in this dissertation would still apply.

In further support of our system model based on the continuum and deterministic channel assumptions, we note that the simulation results in [5, 21] and the theoretical study in [19] show that the system with cooperative orthogonal transmission has a deterministic SNR by continuum assumption even in the presence of fading and randomness in the channel, which ultimately gives the same result based on the deterministic channel assumption. Therefore, we note that the theoretical and numerical approaches in this dissertation still work for random fading channels with finite but high node density as well.

### 3.2 Validity in Finite-density Networks

In this section, the applicability and limitation of the analytical model based on the two assumptions are described. This section is focused on how multiple packets propagate in space, the analysis of which is facilitated by the deterministic channel and continuum assumptions. To be specific, we are mainly interested in *packet loss* in multi-packet OLA transmission, which means a packet does not reach the edge of a multi-hop network, for a given inter-packet separation. In the continuum limit, packet loss is indicated in terms of number of hops; that is, a packet is lost if it stops propagating within a finite number of hops (i.e., OLA levels), which is referred to as *transmission die-off* in [19] and [21]. On the other hand, in a real OLA network with finite node density, where the number and placement of nodes are random, packet loss occurs when there is no node that successfully decodes the packet at an intermediate hop before reaching the network edge.

The simulation results in [21], which assume the strip-shaped network, show the propagation prediction based on the continuum assumption is accurate for high enough node

density, specifically  $\rho = 30, 50$ , and  $100$ . For example, when  $\rho = 30$ , the prediction error in the OLA propagation boundary is less than 2% compared to the simulation results. Moreover, in their disk-shaped network study in [19], the continuum analysis shows less than 5% error of the spatial propagation of OLAs to the simulation results of random and finite-density disk networks, when  $\rho = 10$  and  $100$ .

On the other hand, the continuum analysis is not accurate for low node density networks corresponding to  $\rho \leq 5$ , as shown in the simulation results in [21] and [19]. To be specific, the propagation speed becomes highly random with high standard deviation, as  $\rho$  decreases. In particular, for low node-density networks with random fading channel, where the nodes are randomly placed, the packet propagates significantly faster in some parts of the network, while slower in other areas by the opportunistic feature of OLA. Therefore, in this situation, the OLA propagation pattern becomes irregular depending on the speed in different directions, in contrast to the concentric ring pattern in the continuum limit or high-density network as in [19]. However, we note that because of analytical difficulty to predict this highly random propagation characteristic, this dissertation is focused on the high-density network with  $\rho \geq 10$ , where the deterministic channel and continuum assumptions are accurate to model the real network with uniform and random node placement.

### 3.3 Two-dimensional Disk Networks

In the disk-shaped networks, the source is located at the center of the given network area as shown in Figure 6. For the path loss exponent of  $\alpha$ , the first OLA for Packet  $i$  is a disk denoted  $\mathbb{O}_{(i;1)}$ , as shown in Figure 6, with boundary  $r_{(i;1)}$ , which satisfies  $P_s/r_{(i;1)}^\alpha = \tau$ , where  $\tau$  is the decoding threshold. Subsequent OLAs for this packet (Packet  $i$ ) form concentric rings, centered at the origin. In general,  $r_{(i;k-1)}$  and  $r_{(i;k)}$  are the inner and outer boundaries, respectively, of Level  $k$  OLA  $\mathbb{O}_{(i;k)}$  for the same Packet  $i$ . We note that the level index  $k$  is one less than the index of the hop in which  $\mathbb{O}_{(i;k)}$  transmits. For example, for Packet  $i$ , the source transmits in the first hop and  $\mathbb{O}_{(i;1)}$  transmits in the second hop.

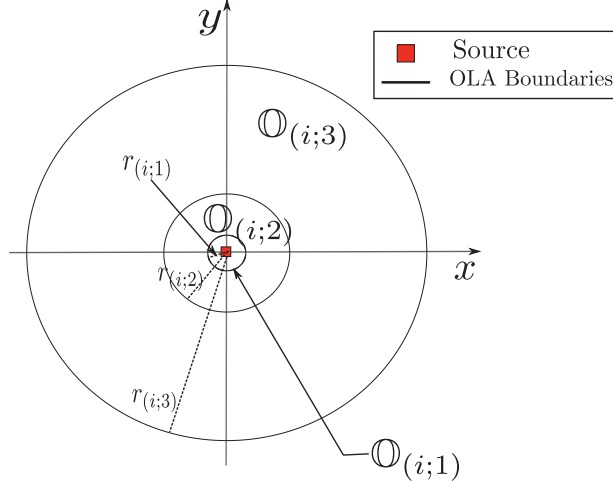


**Figure 6:** Coverage analysis based on Continuum approach

Suppose the receiver location is  $(z, \phi)$  in polar coordinates, where  $z > r_{(i;k)}$ , at the time that OLA  $\mathbb{O}_{(i;k)}$  is transmitting. By circular symmetry, regardless of the angle  $\phi$ , the received SNR at this receiver is denoted  $P(\mathbb{O}_{(i;k)} \rightarrow z) = f(r_{(i;k)}, z) - f(r_{(i;k-1)}, z)$ , where  $f(r, z) = \int_0^r \int_0^{2\pi} \overline{P_r} \cdot l(r \cos \theta - z, r \sin \theta) r dr d\theta$ , as defined in the previous section, which does not have a closed form expression except when  $\alpha = 2$ .

For the free space path attenuation with  $\alpha = 2$ , the function  $f(r, z)$  has a closed form for  $z > r$  as shown in [19], which is given by

$$f(r, z)|_{\alpha=2} = \int_0^r \int_0^{2\pi} \frac{r \cdot \overline{P_r}}{r^2 + z^2 - 2rz \cos \theta} dr d\theta = \pi \overline{P_r} \ln \frac{z^2}{|z^2 - r^2|}, \quad (1)$$

where the subscript ' $_{\alpha=2}$ ' indicates the condition of  $\alpha = 2$ . Therefore, for  $\alpha = 2$ , the received SNR  $P(\mathbb{O}_{(i;k)} \rightarrow z)|_{\alpha=2}$  can be expressed as

$$\begin{aligned} P(\mathbb{O}_{(i;k)} \rightarrow z)|_{\alpha=2} &= f(r_{(i;k)}, z)|_{\alpha=2} - f(r_{(i;k-1)}, z)|_{\alpha=2} \\ &= \pi \overline{P_r} \left| \ln \frac{z^2}{|z^2 - r_{(i;k)}^2|} - \ln \frac{z^2}{|z^2 - r_{(i-1;k)}^2|} \right| \\ &= \pi \overline{P_r} \left| \ln \frac{|z^2 - r_{(i;k-1)}^2|}{|z^2 - r_{(i;k)}^2|} \right|, \end{aligned} \quad (2)$$

where the level index  $k = 1, 2, 3, \dots$  and  $r_0 = 0$ . Also, the absolute value of the logarithm in (2) is just to make sure  $P(\mathbb{O}_{(i;k)} \rightarrow z)|_{\alpha=2} \geq 0$ .

With this closed form expression assuming  $\alpha = 2$ , [19] derived the necessary and sufficient condition for the broadcast to the infinite disc network for “free space” attenuation. In the absence of interference, by defining a new variable  $\mu = \exp(\frac{\tau}{\pi P_r})$ , the condition is  $\mu = \exp(\frac{\tau}{\pi P_r}) \leq 2$  [19].

This condition is interpreted with a physical meaning in [5] using *node degree*  $\kappa = \frac{\rho P_r}{\tau}$ , which is the average number of nodes in the decoding range of a node. Thus, the condition for  $\alpha = 2$  is  $\kappa \geq (\ln 2)^{-1}$ . In other words, the node degree, which is proportional to the transmit power  $P_r$  and node density  $\rho$ , should be large enough for the sustained single-packet OLA broadcasts.

The areas of propagating OLAs are important in the analysis to follow, so we review here the properties of OLA area as a function of hop index in the interference-free case for  $\alpha = 2$ . To be specific, as proven in [19], the area of Level  $k$  OLA,  $A_k = \pi[r_{(i,k)}^2 - r_{(i,k-1)}^2]$ , which is proportional to the transmitting power of  $\mathbb{O}_{(i,k)}$ , is given by

$$A_k = \begin{cases} \frac{\pi P_s}{\tau}, & \mu = 2, \\ \frac{\pi P_s}{\tau(\mu-1)^{k-1}}, & \mu \neq 2. \end{cases} \quad (3)$$

Therefore, when  $\mu < 2$ , the areas of the OLA rings  $A_k$  grow with the hop index, as illustrated in Figure 6; we refer to this as the “ring expansion case.” As we will show in the following sections, the ring expansion means that an OLA for large  $k$  still makes significant interference at the origin. Alternatively, when  $\mu = 2$ , the area of the OLA is kept equal with different  $k$ , because  $A_k = P_s/\tau$  for all  $k$ . Lastly, if  $\mu > 2$ , which means that the node degree is not high enough for the sustained single-packet OLA broadcasts (i.e.,  $\kappa = \frac{\pi P_r}{\tau} < \frac{1}{\ln 2}$ ), the OLA area decreases as  $k$  increases. If plugging in  $\mu > 2$  in (3),  $A_k \rightarrow 0$  as  $k \rightarrow \infty$ , which means that the single packet will stop propagating after some  $k$ . Hence, for the sustained single-packet OLA broadcasts,  $\mu \leq 2$  as shown in [19].

In contrast to  $\alpha = 2$ , when  $\alpha > 2$ , it is very difficult to obtain a closed form solution of the OLA boundaries,  $r_{(i,k)}$ . Considering lossy propagation with a higher path loss exponent,  $\mu < 2$  is not a sufficient condition but a necessary condition for successful OLA broadcast in

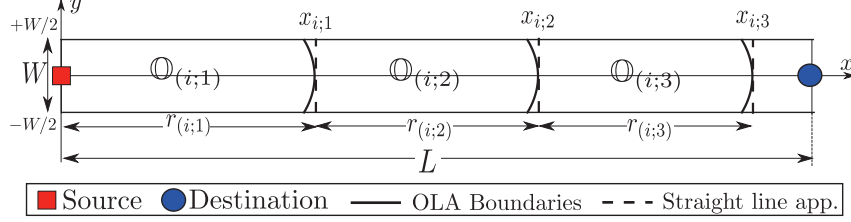


**Figure 7:** The OLA transmission on the strip network based on the continuum assumption and straight line approximation

the absence of interference (the single-packet case) [61]. Furthermore, there is no notion of  $\kappa$  in the continuum limit as we will now explain. The decoding range of a relay is given by the area inside the circle around the relay with the radius of  $r_{\text{siso}}$ , where  $\frac{P_r}{r_{\text{siso}}^\alpha} = \tau$ . Therefore, in a finite-density network with density  $\rho$ , the node degree  $\kappa$  is given by

$$\kappa = \rho \pi r_{\text{siso}}^2 = \rho \left( \frac{P_r}{\tau} \right)^{2/\alpha}. \quad (4)$$

We observe that the exponents of  $\rho$  and  $P_r$  are different, which means  $\kappa$  cannot be expressed as a function of just  $\bar{P}_r$ ,  $\tau$  and  $\alpha$ ; therefore,  $\kappa$  is not constant as the continuum limit is approached for  $\alpha > 2$ . However, we will be able to express bounds in terms of  $\bar{P}_r$  in Theorem 3 in Section 4.2.1.

### 3.4 Two-dimensional Strip Networks

In this section, we consider a strip network with length of  $L$  and width of  $W$ , which is expressed by  $\mathbb{S} = \{(x, y) : 0 \leq x \leq L, |y| \leq \frac{W}{2}\}$ , where decode-and-forward (DF) wireless nodes are uniformly and randomly distributed with average density of  $\rho$ . Assuming unicast traffic, as shown in Figure 7, the source node is at the origin, while the destination is at the right end separated by  $L$  from the source. The other nodes are operating DF relays that forward the packet only when the decoding is successful and the node has not transmitted the packet before [9]. On the other hand, since all nodes in our system model, besides the source, have the opportunity to receive the message, the results in this dissertation also apply to broadcasting.

The first level OLA for the  $i$ th packet is the area denoted by  $\mathbb{O}_{(i,1)}$ , as shown in Figure

7, with boundary  $x_{(i;1)}$  that satisfies  $P_s/x_{(i;1)}^\alpha = \tau$ . Also, for Level  $k \geq 1$ , the nodes that have not transmitted the packet (Packet  $i$ ) so far will join the next level  $k + 1$ , if their received SNR, the signal component of which is determined by the received power from the current level OLA  $\mathbb{O}_{(i;k)}$ , is greater than or equal to  $\tau$ . In other words, subsequent OLAs  $\mathbb{O}_{(i;k)}$  of this packet without interference for  $k \geq 2$  are formed by the SNR condition, which is given by

$$\mathbb{O}_{(i;k)} = \{(x, y) \in \mathbb{S} \setminus \bigcup_{n=1}^{k-1} \mathbb{O}_{(i;n)} : \iint_{\mathbb{O}_{(i;k-1)}} \frac{\overline{P}_r}{[(x - x')^2 + (y - y')^2]^{\alpha/2}} dx' dy' \leq \tau\}. \quad (5)$$

As shown in [21], when the width  $W$  is small enough, the curved boundaries of the OLAs can be approximated by straight lines indicated by the dashed lines in Figure 7. Therefore, the approximated OLA,  $\tilde{\mathbb{O}}_{(i;k)}$ , is the area that satisfies  $x_{(i;k-1)} \leq x \leq x_{(i;k)}$  and  $|y| \leq \frac{W}{2}$ . Suppose the location of a receiver is  $(z, 0)$  such that  $z < x_{(i;k-1)}$  or  $z > x_{(i;k)}$  at the time that OLA  $\tilde{\mathbb{O}}_{(i;k)}$  is transmitting. The SNR at this receiver is denoted as

$$P(\tilde{\mathbb{O}}_{(i;k)} \rightarrow z) = \iint_{\tilde{\mathbb{O}}_{(i;k)}} \frac{\overline{P}_r}{[(x - z)^2 + y^2]^{\alpha/2}} dx dy = \int_{-W/2}^{W/2} \int_{x_{(i;k-1)}}^{x_{(i;k)}} \frac{\overline{P}_r}{[(x - z)^2 + y^2]^{\alpha/2}} dx dy, \quad (6)$$

where the OLA level index  $k = 1, 2, 3, \dots$ , and  $x_0 = 0$ . Therefore, the outer boundary of  $(k + 1)$ st OLA,  $x_{(i;k+1)}$  is the solution of  $P(\tilde{\mathbb{O}}_{(i;k)} \rightarrow z) = \tau$  such that  $z > x_{(i;k)}$ . Let  $r_{(i;k)} = x_{(i;k)} - x_{(i;k-1)}$  be the step-size of  $i$ th packet for  $k$ th level. We treat this integral equation differently, depending on if the path loss exponent  $\alpha$  satisfies  $\alpha = 2$  or  $\alpha > 2$ , because the analytical methods are different.

In spite of the different analytical methods, the two following subsections will show that, for any  $\alpha \geq 2$ , the single-packet OLA propagation with large enough  $\overline{P}_r$  reaches the steady-state, in which the step-size  $r_{(i;k)}$  converges to a fixed value, as the OLA level index  $k$  increases. In other words, the sizes (i.e., hop-distances) of OLAs of a single packet are kept to be the same after a certain  $k$ . We point out that the second case with  $\alpha > 2$  is not present in the existing literature.

### 3.4.1 Free Space Path Attenuation ( $\alpha = 2$ )

For  $\alpha = 2$ , the received power equation in (6) can be expressed by

$$P(\tilde{\mathcal{O}}_{(i;k)} \rightarrow z)|_{\alpha=2} = \int_{x_{(i;k-1)}}^{x_{(i;k)}} \frac{2\bar{P}_r}{(x-z)} \arctan\left(\frac{W}{2(x-z)}\right) dx, \quad (7)$$

The behavior of the single-shot (i.e., single-packet) OLA transmission is well studied in [21], when  $\alpha = 2$ . They derive the sufficient condition for the propagation to the infinite-length strip network, in the absence of interference; the condition is  $\mu < 2$ , where  $\mu = \exp(\frac{\tau}{\pi\bar{P}_r})$ . When this condition holds, as the OLA level goes to infinity, the step-size converges to a positive number  $r_{(i,\infty)}$ , which satisfies  $\frac{W(\pi \ln 2 - \bar{P}_r/\tau)}{4} \leq r_{(i,\infty)} \leq \frac{W\bar{P}_r}{2\tau}$  [21].

### 3.4.2 Higher Path Attenuation ( $\alpha > 2$ )

Many indoor and short-range wireless networks are lossy with higher path loss exponents, so we also investigate the OLA propagation with higher path loss exponent  $\alpha > 2$ , which is not covered in [21]. Following the analytical approach in [21] for  $\alpha = 2$ , to show the steady-state with equal step-size, we will first derive the relationship between the step-sizes of two consecutive OLA levels,  $k$  and  $k + 1$ , by defining a function  $r_{(i;k+1)} = h(r_{(i;k)})$ . Then, we will prove the existence of the steady-state satisfying  $r_{(i;k+1)} = r_{(i;k)}$  that corresponds to the solution of  $x = h(x)$  by showing the properties of  $h(\cdot)$ .

First, when  $\alpha > 2$ , the received power in (6) is given by

$$P(\tilde{\mathcal{O}}_{(i;k)} \rightarrow z)|_{\alpha>2} = \int_{x_{(i;k-1)}}^{x_{(i;k)}} \frac{\bar{P}_r \left(\frac{W^2}{4} + (x-z)^2\right)^{-\alpha/2} (W^2 + 4(x-z)^2)}{4W(\alpha-2)(x-z)^2} \\ \times \left[ (W^2 + 4(x-z)^2) {}_2F_1\left(1, \frac{3-\alpha}{2}, \frac{-1}{2}, \frac{-W^2}{4(x-z)^2}\right) + ((\alpha-5)W^2 - 4(x-z)^2) {}_2F_1\left(1, \frac{3-\alpha}{2}, \frac{1}{2}, \frac{-W^2}{4(x-z)^2}\right) \right] dx, \quad (8)$$

where  $k = 1, 2, 3, \dots$ ,  $x_0 = 0$ , and  ${}_2F_1(\cdot, \cdot, \cdot, \cdot)$  is the Gauss Hypergeometric function [62].

As the previous case with  $\alpha = 2$ , to find the next OLA boundary  $x_{i;k+1}$ , we need to solve the equation  $P(\tilde{\mathcal{O}}_{(i;k)} \rightarrow z) = \tau$ , which can be expressed in terms of the step-size  $r_{(i;k+1)}$  because  $x_{(i;k+1)} = x_{(i;k)} + r_{(i;k+1)}$ . By the variable change with  $u = (x - z)$ , this equation can



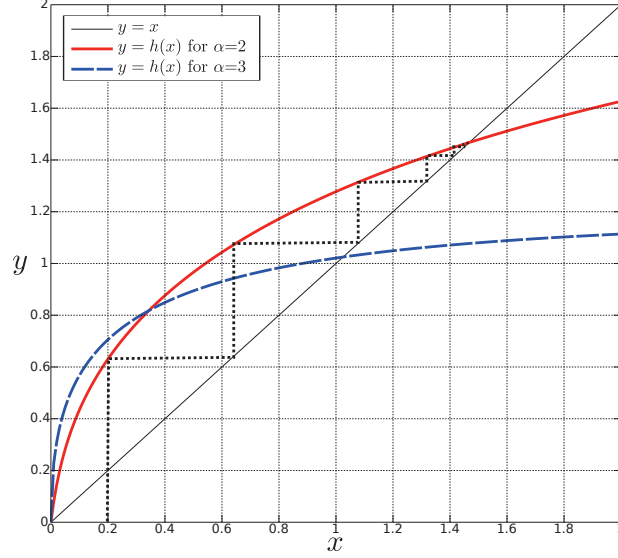


**Figure 8:**  $h(x)$  curves for  $\alpha = 2$  and  $3$ , when  $\bar{P}_r = 3$ ,  $\tau = 1$ , and  $W = 1$

be expressed as

$$\int_{r(i;k+1)}^{r(i;k+1)+r(i;k)} \frac{\left(\frac{W^2}{4} + u^2\right)^{-\alpha/2} (W^2 + 4u^2)}{4W(\alpha - 2)u^2} \times \left[ (W^2 + 4u^2) {}_2F_1\left(1, \frac{3-\alpha}{2}, \frac{-1}{2}, \frac{-W^2}{4u^2}\right) + ((\alpha-5)W^2 - 4u^2) {}_2F_1\left(1, \frac{3-\alpha}{2}, \frac{1}{2}, \frac{-W^2}{4u^2}\right) \right] du = \frac{\tau}{\bar{P}_r}. \quad (9)$$

Let  $G(u, \alpha, W)$  be the term inside the integral. Then, the subsequent step-sizes can be iteratively obtained with  $r_{(i;k+1)} = h(r_{(i;k)})$ , where the function  $h(r_{(i;k)})$  is defined as the unique solution of  $\int_{h(r_{(i;k)})}^{h(r_{(i;k)})+r_{(i;k)}} G(u, \alpha, W) du = \tau/\bar{P}_r$  for  $r_{(i;k)} > 0$ . The following properties for  $h(\cdot)$  are proved in the Appendix.

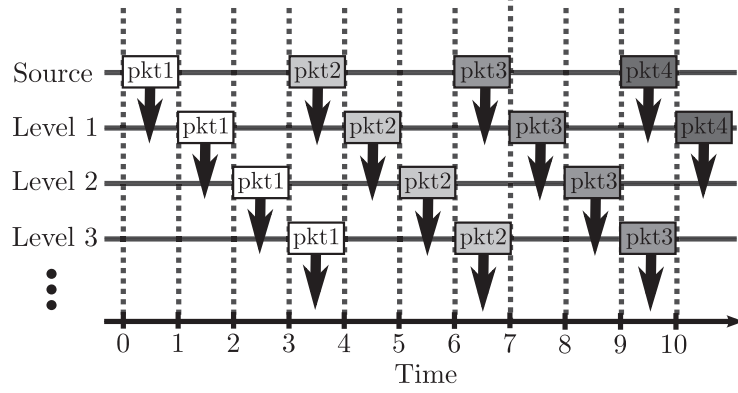
1. For any  $x > 0$ , there exists a unique solution,  $h(x)$ , for  $\int_{h(x)}^{h(x)+x} G(u, \alpha, W) du = \frac{\tau}{\bar{P}_r}$ . By continuity  $h(0) := \lim_{x \rightarrow 0} h(x) = 0$ .
2. The function  $h(\cdot)$  is monotonically increasing.
3. The function  $h(\cdot)$  is concave.

Figure 8 displays these properties of  $h(x)$ , where the black straight line displays  $y = x$  graph, and the red (curved) solid line and the dashed line indicate  $h(x)$  curves of  $\alpha = 2$

and 3, respectively. The three properties proven here for  $\alpha > 2$  are identical to the findings about  $h(x)$  when  $\alpha = 2$  in [21]. Therefore, as proven in [21], if  $h(x) = x$  has a solution except  $x = 0$ , which corresponds to the crossing points of  $y = h(x)$  and  $y = x$  curves in Figure 8, the OLA propagation reaches the steady-state with OLA step-size converged to the solution (i.e.,  $r_{(i;\infty)} = x$ ). For example, the black dotted line indicates how the one-shot OLA transmission reaches the steady-state with  $\alpha = 2$ . Because of more severe path attenuation, the limiting step-size decreases as  $\alpha$  increases as indicated by the crossing points of Figure 8. While  $h'(0)$  has a closed form expression for  $\alpha = 2$ , which corresponds to the sufficient condition for sustained single-packet OLA transmission in a strip network (i.e.,  $\mu < 2$  for  $\alpha = 2$ ) as shown in [21], it is very difficult to obtain the closed form expression of  $h'(0)$ , when  $\alpha > 2$ . As a result, it is also difficult to derive the sufficient condition for sustained single-packet OLA transmission along the strip network in a closed form for  $\alpha > 2$ . However, by the analytical properties for  $\alpha > 2$  proved in the Appendix, we can conclude that the propagation patterns for the both cases ( $\alpha = 2$  and  $\alpha > 2$ ) reach a steady-state with high enough relay transmission power  $\bar{P}_r$ . Furthermore, in constant to  $\alpha = 2$ , for  $\alpha > 2$ , there is no notion of  $\kappa$  in the continuum limit. We observe that the exponents of  $\rho$  and  $P_r$  in (4) are different, and therefore,  $\kappa$  is not constant as the continuum limit is approached for  $\alpha > 2$ .

### 3.5 Multi-packet Transmission and Network Throughput

In this section, we consider multiple packets transmitted from the source to the whole network. We use the definition of the throughput in [18]: the rate at which packets cross a measurement boundary. In other words, we focus on the packet-level throughput analysis as in [18] assuming the packet size, modulation order, coding ratio or other physical-layer parameters are fixed. In some applications, such as large file transfer, throughput is more important than end-to-end latency of a single packet. If the boundary is at the origin where



**Figure 9:** Timing diagram of spatial pipelined OLA with  $M = 3$

the source is located, the throughput is identical to the reciprocal of the packet insertion period at the source (i.e., how often the source can send a new data packet into the network). In the conventional network with single-input-single-output (SISO) links, the packet insertion rate is determined by the time duration that the channel around the source is available again after sending a packet because carrier sense multiple access with collision avoidance (CSMA/CA) is used [63]. However, we note that CSMA/CA, which results in nodes initiating transmission at random times, is not desirable for the OLA transmission, because of the autonomous and distributed control in each node and the need for OLAs to have synchronized transmission. The transmit time synchronization for the same OLA can be achieved based on Global Positioning System (GPS) [12]. Also, in the absence of GPS or other external devices, the preamble-based transmit time synchronization method developed in our research group can be used, as demonstrated using a software-defined radio (SDR) platform in indoor environments in [54]. To be specific, the transmit time synchronization scheme in [54] is designed to support the OLA transmissions. In this scheme, the relays doing CT use an embedded time stamp, which is based on the reception from the previous hop, to hold the packet for a fixed period before firing. The experimental results in [54] show mean rms transmit time spreads on the order of  $50ns$  in indoor environments.

Our main interest in this dissertation is to increase the throughput of OLA transmissions using *spatial pipelining*, which means transmitting a co-channel packet before the previous

one has cleared the network. We define one time unit as the time duration required for transmission and reception over one hop. Suppose the packet insertion period at the source is  $M$  (i.e., the source node injects a new packet into the network every  $M$  time units.) Figure 9 shows an example of spatially pipelined OLA transmissions with  $M = 3$ , where the x- and y-axes represent time and OLA level, respectively. In fact,  $M = 3$  is the minimum packet insertion period that we can achieve because the nodes are assumed to be half-duplex. Since  $M = 3$  in this example in Figure 9, the source injects a new packet (from Packet 1 to 4) at  $t = 0, 3, 6, 9$  with a fixed period  $M = 3$ , and the following level OLAs also periodically receive and forward the packets. Therefore, multiple packets, indicated by the squares with different brightness, are propagating across the network at the same time using the same channel with certain inter-separations, which is called *spatial pipelining*.

If the number of transmitted packets is infinite, the throughput, which is denoted by  $\eta$ , is equal to  $1/M$  as long as the decoding conditions for all the packets in the network are satisfied. However, if spatial pipelining causes a critical drop in SINR at the receivers, it is possible for some packets to stop propagating in the middle of the network, which results in lower throughput. Therefore, we want  $M$  to be in the range that no packet loss occurs. On the other hand, we also consider the propagation speed of a packet, which is implied by the hop-distance of the packet. The propagation speed should be positive (non-zero) until the packet reaches the network edge not to stop propagating in the middle of the network.

## CHAPTER 4

### MULTI-PACKET OLA BROADCASTS IN DISK NETWORKS

#### 4.1 Signal Model of Intra-flow Interference

As a simple example, suppose only two packets are broadcasted such that the second one is transmitted by the source  $M$  time slots after the first as shown in Figure 10. The shaded areas in Figure 10 indicate two OLAs that could be transmitting at the same time. Suppose the smaller one,  $\odot_{(2;k)}$ , transmits the 2nd packet in its  $k + 1$ st hop, and  $\odot_{(1;k+M)}$ , transmits the first packet in its  $k + M + 1$ st hop. We are interested to know if receivers at Points  $A$  at radius  $r_A$  and  $B$  at radius  $r_B$  will be able to decode Packets 1 and 2, respectively. We note that  $r_{(1;k+M)} < r_A$  and  $r_{(2;k)} < r_B < r_{(1;k+M-1)}$ .

For the receiver at Point  $A$ , we have,

$$\text{SINR}_{(1;k+M+1)}(r_A) = \frac{\mathbf{S}}{\mathbf{I} + \mathbf{N}} = \frac{P(\odot_{(1;k+M)} \rightarrow r_A)}{P(\odot_{(2;k)} \rightarrow r_A) + 1}, \quad (10)$$

where  $\mathbf{N} = 1$  by the unit noise power assumption. We will assume that if this SINR is greater than  $\tau$ , the receiver can decode. For the receiver at Point  $B$ , the interference comes from the ring,  $\odot_{(1;k+M)}$ , which encloses Point  $B$ . We will denote that “backwards

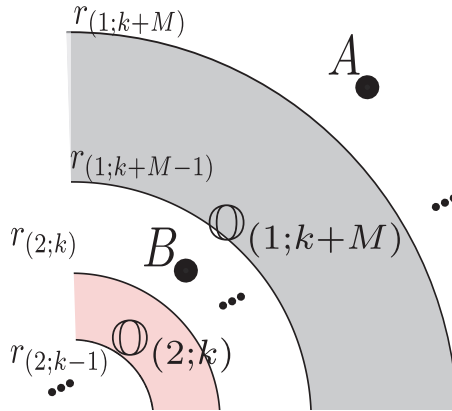


**Figure 10:** Intra-flow interference of multiple packets OLA broadcasts

propagating" power by  $P(r_B \leftarrow \mathbb{O}_{(1;k+M)})$ , and for  $\alpha = 2$ , it can be expressed as

$$P(r_B \leftarrow \mathbb{O}_{(1;k+M)})|_{\alpha=2} = \pi \overline{P_r} \ln \left( \frac{|r_{(1;k+M)}^2 - r_B^2|}{|r_{(1;k+M-1)}^2 - r_B^2|} \right). \quad (11)$$

Thus, for the receiver at Point  $B$ , the SINR is

$$\text{SINR}_{(2;k+1)}(r_B) = \frac{P(\mathbb{O}_{(2;k)} \rightarrow r_B)}{P(r_B \leftarrow \mathbb{O}_{(1;k+M)}) + \mathbf{N}}, \quad (12)$$

where  $\mathbf{N} = 1$  by the assumption in our system model. Therefore,  $r_{(2;k+1)}$  satisfies

$$\text{SINR}_{(2;k+1)}(r_{(2;k+1)}) = \tau. \quad (13)$$

## 4.2 Theoretical Analysis of Pipelined broadcast in the infinite disk network

In this section, we theoretically analyze how the OLA propagation is affected in the infinite disk when multiple packets are transmitted with fixed packet insertion period  $M$  (i.e., the Source inserts a new packet every  $M$  time units). In particular, we are interested in the feasibility of spatially pipelined OLA broadcasts in the presence of intra-flow interference. This infinite disk network exists only theoretically, but it gives an intuition for very large networks where it takes a large number of hop counts to cover the whole network area. The result is different depending on if the path loss exponent,  $\alpha$ , satisfies  $\alpha = 2$  or  $\alpha > 2$ , so we treat these cases in separate sections. To be specific, we will prove that the free space path attenuation with  $\alpha = 2$  makes the spatial pipelining infeasible in Section 4.2.1, while the higher path attenuation with  $\alpha > 2$  allows multi-packet co-channel OLA transmissions with finite packet insertion period  $M$  in Section 4.2.2. Moreover, for the feasible case with path attenuation  $\alpha > 2$  we will derive the impacts of two system parameters  $\alpha$  and  $\tau$  on the lower bound of broadcast throughput in Section 4.2.3 for the interference-limited case. The final results in this section are summarized in Table 1.

### 4.2.1 Feasibility for Free Space Path Loss Exponent ( $\alpha = 2$ )

In this section, we consider the feasibility of sustained multi-packet OLA broadcasts for  $\alpha = 2$ . We make the initial assumption that if sustained multi-packet broadcasting for

**Table 1:** Feasibility of spatially-pipelined OLA broadcasts in the infinite disk network ( $\alpha$ : path-loss exponent,  $\tau$ : decoding threshold,  $\bar{P}_r$ : transmit power per unit area,  $\mu = \exp(\frac{\tau}{\pi \bar{P}_r})$ )

Condition		Feasibility	Corresponding Theorem
$\alpha = 2$	$\mu < 2$	Infeasible	Theorem 1 based on Lemmas 1 and 2
	$\mu = 2$	Infeasible for $\tau > 1$	Theorem 2
$\alpha > 2$		Feasible	Theorem 3

$\alpha = 2$  is possible, then each packet must also at least satisfy the condition for sustained single-packet broadcasting, which is  $\mu \leq 2$  [19]. We will show that under this constraint of  $\mu \leq 2$ , sustained multi-packet broadcasting is infeasible. We will prove this in two parts: first considering the ring expansion case ( $\mu < 2$ ) and second considering the constant-ring-area case ( $\mu = 2$ ). To be specific, for the both cases ( $\mu < 2$  and  $\mu = 2$ ), we will show that when  $\alpha = 2$ , the spatial pipelining is *infeasible* by looking at the SINRs of the two packets (the first and second packets) at the moment the second packet is inserted by the Source  $M$  time slots after the first packet was transmitted.

**Lemma 1** *In the ring expansion case ( $\mu < 2$ ) in the infinitely large network with  $\alpha = 2$ , the interference from the first packet to a disk around the Source with radius  $z$  has a non-zero lower bound regardless of the value of  $M$ , when  $z \rightarrow 0$ .*

*Proof:* With the packet insertion gap of  $M$ , the interference from the first packet to a receiver at a radius  $z$  arbitrarily near the Source is

$$P(z \leftarrow \mathbb{O}_{(1;M-1)})|_{\alpha=2} = \pi \bar{P}_r \ln \left( \frac{|r_{(1;M-1)}^2 - z^2|}{|r_{(1;M-2)}^2 - z^2|} \right), \quad (14)$$

where  $r_{(1;k)}^2 = \frac{P_s(\mu-1)}{\tau(\mu-2)} \left( 1 - \frac{1}{(\mu-1)^k} \right)$  [19]. Therefore,  $P(z \leftarrow \mathbb{O}_{(1;M-1)})$  is a decreasing function of  $M$ , and an increasing function of  $z$ , and has the limit

$$\begin{aligned} P(0 \leftarrow \mathbb{O}_{(1;\infty)})|_{\alpha=2} &= \lim_{z \rightarrow 0, M \rightarrow \infty} P(z \leftarrow \mathbb{O}_{(1;M-1)})|_{\alpha=2} \\ &= \pi \bar{P}_r \ln \left( \frac{1}{\mu - 1} \right) > 0. \end{aligned} \quad (15)$$

□

This implies that no matter how long we wait for the first packet to “move away” from the source, the power from it is never less than  $P(0 \leftarrow \mathbb{O}_{(1;\infty)})|_{\alpha=2}$ . In other words, the co-channel interference from Packet 1 to Packet 2 at the moment when Packet 2 is inserted does not go to zero, even when  $M \rightarrow \infty$ . The reason is that the OLA widths grow without bound with hop index  $k$ . This can be observed by noticing that  $r_{(1;k+1)}^2 - r_{(1;k)}^2$  is proportional to  $1/(\mu - 1)^k$ .

**Lemma 2** *For the ring expansion case ( $\mu < 2$ ) in the infinitely large network with  $\alpha = 2$ , no node at a disk around the Source with radius  $z \rightarrow 0$  can ever decode the second packet, if*

$$P_s < \tau \left[ 1 + \pi \overline{P}_r \ln \left( \frac{1}{\mu - 1} \right) \right]. \quad (16)$$

*Proof:* The maximum received SNR for Packet 2 is  $P_s$ . Therefore, based on Lemma 1, as  $M \rightarrow \infty$ , the maximum SINR at the disk around the source with radius  $z \rightarrow 0$  is given by

$$\max \mathbf{SINR}_{2,1}(z \rightarrow 0)|_{\alpha=2} = \frac{P_s}{1 + \pi \overline{P}_r \ln \left( \frac{1}{\mu - 1} \right)}. \quad (17)$$

Hence, if this maximum value is less than the decoding threshold,  $\tau$ , the second packet cannot form its first OLA,  $\mathbb{O}_{(2;1)}$ .  $\square$

The feasibility condition of the second packet insertion following (16) in this lemma is because of the ring-expansion of the first packet, which does not experience any co-channel interference until the second packet is inserted. In other words, when Packet 2 is inserted, the Packet 1 has an excessively large OLA, which causes significant interference to Packet 2. This ring expansion is beneficial for the single-packet transmission, because it takes less hops to propagate across the network. However, in the multi-packet OLA transmission, the ring-expansion of Packet 1 suppresses the insertion of Packet 2.

**Theorem 1** *In the ring expansion case ( $\mu < 2$ ) in the infinitely large network with  $\alpha = 2$ , when  $\tau \geq 1$ , the second packet always stops propagating in a finite number of hops.  $\tau \geq 1$*



corresponds to the class of bandwidth-efficient waveforms [57], which would be desirable for large file transfers.

The proof is shown in Appendix B. Theorem 1 shows that the “ring expansion” property of the OLA broadcasts makes pipelined packet transmission impossible for  $\tau \geq 1$ . In other words, even if the source transmission power  $P_s$  is large enough to insert Packet 2, which means  $P_s > \tau[1 + \pi\overline{P_r} \ln(\frac{1}{\mu-1})]$  as the opposite case of Lemma 2, Packet 2 always stops propagating for  $\tau > 1$ , because of the excessive interference from Packet 1, the OLA size of which increases exponentially until Packet 2 is inserted.

One might think that when  $\mu = 2$ , the pipelined packet transmission is feasible without the packet loss because the limit in (15) goes to zero by plugging the OLA boundary equation in [19],  $r_{(1;k)}^2 = \frac{P_s k}{\tau}$  into (14). However, this limit  $P(0 \leftarrow \mathbb{O}_{(1;\infty)})|_{\alpha=2} \rightarrow 0$  holds only when  $M \rightarrow \infty$ , which implies the insertion of Packet 2 should wait for an infinite time after Packet 1 transmission. Also, the following theorem shows that the finite packet insertion rate is not achievable, when  $\mu = 2$ .

**Theorem 2** *If  $\mu = 2$ ,  $\alpha = 2$ , and  $\tau \geq 1$ , the pipelined packet transmission is impossible in the infinitely large network with a finite  $M$ .*

The proof is shown in Appendix C. Even though  $\mu = 2$  does not cause the ring-expansion of Packet 1, spatial pipelining is infeasible, because  $\mu = 2$  is the very boundary value for the sustained OLA transmission for the “single-packet case.” Therefore, if co-channel interference is present, the successful OLA transmission condition in terms of SINR ceases to hold even with extremely small interference. In conclusion, Theorems 1 and 2 show that spatial pipelining of OLA broadcasts in the infinite disk network is infeasible with fixed relay transmission power for the free space path loss exponent  $\alpha = 2$ .

#### 4.2.2 Feasibility for Higher Path Loss Exponent ( $\alpha > 2$ )

Because many indoor and short-range wireless networks are lossy with higher path loss exponents, we analyze the feasibility of multiple packet OLA broadcasts in infinite networks for  $\alpha > 2$  in this section. While  $\alpha = 2$  gives a closed form solution of the integral  $f(r, z) = \int_0^r \int_0^{2\pi} \overline{P_r} \cdot l(r \cos \theta - z, r \sin \theta) r dr d\theta$ , where  $l(x, y) = \frac{1}{(x^2 + y^2)^{\alpha/2}}$ , a closed form solution for  $\alpha > 2$  appears to be very difficult to obtain [61]. Therefore, we are not able to derive the closed form expressions of the OLA boundaries even for the single-packet OLA broadcasts. However, [16] shows a sufficient condition of multiple packet OLA broadcast to reach an infinitely large network, propagating at least linearly (i.e.,  $r_{(i,k)} - r_{(i,k-1)} = \Delta$ , where  $\Delta$  is a positive constant) in the presence of co-channel intra-flow interference from later packets. Even though [16] does not consider the interference from the preceding packets because they assume perfect interference cancellation, their theoretical approach to prove the feasibility of spatial pipelining is still applicable for the interference scenario by modification. In the following theorem, we consider the upper bound of the broadcast throughput for  $\alpha > 2$  by introducing the packet insertion period concept, assuming at-least-linearly propagating OLA broadcasts.

**Theorem 3** *When  $\alpha > 2$ , it is “feasible” for spatially pipelined packets to propagate over the infinitely large network with at-least-linearly increasing radial distances (the outer boundaries) with a finite  $M > 3$  assuming the half-duplex nodes, thereby avoiding any packet loss in infinitely large disk networks.*

The proof is shown in Appendix D. The previous theorem treats the  $k$ th hop of the  $i$ th packet, where  $k \geq 1$ . When a new packet is inserted at the source, which corresponds to  $k = 0$ , the only difference with the SINR lower bound for  $k \geq 1$  is that the received signal power  $\mathbf{S} = P_s/\Delta^\alpha$ , while the interference term  $\mathbf{I}$  has the same upper bound as (76). Therefore, if the source transmission power  $P_s$  is high enough, the consecutive packet insertion at the source is feasible, satisfying the linear propagation condition. This feasibility of spatial pipelining

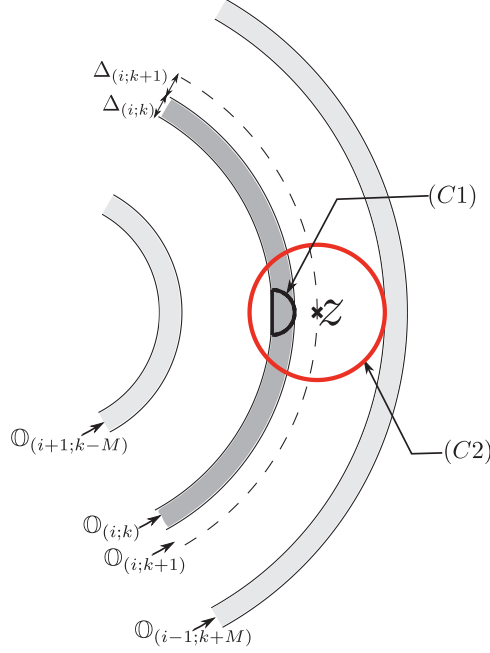


**Figure 11:** Illustration to derive the lower bound of SINR for a given packet insertion period  $M$

for  $\alpha > 2$  is because the high path attenuation of the co-channel interference with  $\alpha > 2$  is beneficial to enhance the spatial reuse, even though the desired signal component also experiences higher attenuation than  $\alpha = 2$ . Because the spatial pipelining is feasible in the presence of co-channel interference when  $\alpha > 2$ , while it is not feasible with  $\alpha = 2$ , now we need to consider the broadcast throughput optimization. Thus, in the following section, we derive the lower bound of the broadcast throughput using the SINR lower bound in (77).

#### 4.2.3 Lower Bound of Broadcast Throughput with $\alpha > 2$ for the Interference-limited Case

In this section, we focus on the theoretical lower bound of the broadcast throughput in the infinite disk network simplifying (77) for the “*interference-limited case*”, by assuming high transmit powers. The key issue in the pipelined OLA broadcasts is the selection of  $M$ ; we want to find the smallest  $M$  satisfying the SINR condition for the infinite disk network that avoids all packet loss, so the throughput  $\eta = 1/M$  is maximized. In other words,  $M_{I,opt}$  is the minimum packet insertion period  $M$  for given parameters such as  $\alpha$ ,  $\bar{P}_r$ ,  $\tau$ , with which the spatially pipelined OLA broadcasting has no packet loss in the infinite disk network.

Suppose  $\hat{M}_{I,opt} = 1/\hat{\eta}_{I,opt}$  is the solution of (77), then  $\hat{\eta}_{I,opt}$  serves as a lower bound of the true optimum  $\eta_{I,opt} = 1/M_{I,opt}$ , because (77) involves  $\mathbf{SINR}_{LB}$ , a lower-than-actual SINR. However, it is difficult to solve (77) to obtain  $\hat{\eta}_{I,opt} = 1/\hat{M}_{I,opt}$ , because of the noise term in the denominator. Hence, in the following Section 4.2.3.1, we will derive an approximate lower bound  $\hat{\eta}_{I,opt}^* = \hat{\eta}_{I,opt}$  in the interference-limited case. Next, we will consider how this bound is impacted by  $\alpha$  and  $\tau$ , in Sections 4.2.3.2 and 4.2.3.3, respectively. The theoretical results on the impacts of  $\alpha$  and  $\tau$  will be compared with the numeral results in the finite disk network for  $\alpha > 2$  in Section 4.4. Lastly, the numerical results in Section 4.2.3.4 will show the comparison between  $\hat{M}_{I,opt}$  and  $\hat{M}_{I,opt}^*$ , where  $\hat{M}_{I,opt}^*$  is the approximate version of  $\hat{M}_{I,opt}$  in the interference-limited case.

#### 4.2.3.1 Approximate Lower Bound $\hat{\eta}_{I,opt}^* = 1/\hat{M}_{I,opt}^*$ for the Interference-limited Case

As  $\bar{P}_r \rightarrow \infty$ ,  $\mathbf{SINR}_{LB}$  in (77) becomes

$$\mathbf{SINR}_{LB} \approx \mathbf{SIR}_{LB} = \frac{(\alpha - 2)(M - 2)^{\alpha-2}}{2^{\alpha+2}}. \quad (18)$$

If we solve  $\mathbf{SIR}_{LB} \geq \tau$  in terms of  $M$ , it gives the minimum packet insertion period as

$$\hat{M}_{I,opt}^* = 2 + \left\lceil \left( \frac{\tau \cdot 2^{\alpha+2}}{\alpha - 2} \right)^{\frac{1}{\alpha-2}} \right\rceil, \quad (19)$$

where the ceiling makes  $\hat{M}_{I,opt}^*$  a positive integer. This bound is a function of just two parameters:  $\tau$  and  $\alpha$ , so it is easier to find this  $\hat{M}_{I,opt}^*$  than  $\hat{M}_{I,opt}$  that is the minimum  $M$  satisfying (77). Using this approximation, we can find the relationship between the achievable broadcast throughput and the system parameters such as  $\alpha$  and  $\tau$  for the interference-limited regime. The two following subsections show the impacts of  $\alpha$  and  $\tau$ , respectively.

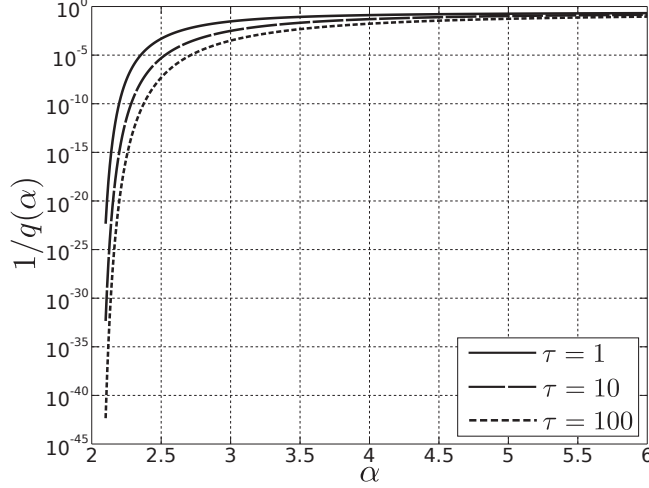


**Figure 12:**  $\alpha$  versus  $1/q(\alpha)$ , when  $\tau = \{1, 10, 100\}$

#### 4.2.3.2 $\hat{M}_{I,opt}^*$ and $\alpha$

Using (19), we can identify the impact of the path loss exponent  $\alpha$  on  $\hat{M}_{I,opt}^*$  for the interference-limited regime. For simplicity, excluding the ceiling on the right hand side in (19), we define a function  $q(\alpha) = 2 + \left(\frac{\tau \cdot 2^{\alpha+2}}{\alpha-2}\right)^{\frac{1}{\alpha-2}}$ , which is less than or equal to the original term with the ceiling. If we differentiate  $q(\alpha)$  with respect to  $\alpha$ , we have

$$q'(\alpha) := \frac{\partial q}{\partial \alpha} = \left(\frac{2^{\alpha+2}\tau}{\alpha-2}\right)^{\frac{1}{\alpha-2}} \times \left( \frac{2^{-\alpha-2} \left( \frac{2^{\alpha+2}\tau \ln 2}{\alpha-2} - \frac{2^{\alpha+2}\tau}{(\alpha-2)^2} \right)}{\tau} - \frac{\ln \left( \frac{2^{\alpha+2}\tau}{\alpha-2} \right)}{(\alpha-2)^2} \right), \quad (20)$$

where  $\alpha > 2$  and the solution of  $q'(\alpha) = 0$  is  $\alpha^* = 2(1 + 8e^\tau)$ . From the second derivative,  $q''(\alpha) = \frac{\partial^2 q}{\partial \alpha^2}$ , we have that  $q''(\alpha^*) > 0$  for  $\tau > 0$ . Therefore, the function  $q(\alpha)$  is minimized at  $\alpha^* = 2(1 + 8e^\tau)$ . Moreover, because  $q'(\alpha) < 0$  for  $1 < \alpha < \alpha^*$ ,  $q$  is decreasing as  $\alpha$  increases. Hence, in this range the achievable throughput is increasing as  $\alpha$  increases. With the ceiling as in (19),  $\hat{M}_{I,opt}^*$  is decreasing or kept to be the same, as  $\alpha$  increases.

Therefore, for the interference-limited regime,  $\hat{\eta}_{I,opt}^* = 1/\hat{M}_{I,opt}^*$  is increasing as  $\alpha$  increases in the range of  $1 < \alpha \leq 2(1 + 8e^\tau)$  for the given decoding threshold  $\tau$ . For the practical interpretation, we assume  $\tau \geq 1$ , which corresponds to the class of bandwidth-efficient waveforms [57] and appropriate for large file transfers. For example,  $\alpha^* \approx 45.4925$

for  $\tau = 1$ . Therefore, in the practical ranges of  $\tau$  and  $\alpha$ , the lower bound of the broadcast throughput  $\hat{\eta}_{I,opt}^*$  increases, as  $\alpha$  increases, which implies the better spatial reuse for higher  $\alpha$ . This relationship can be observed in Figure 12, where the horizontal axis represents the path loss exponent  $\alpha$  with the practical range  $2 < \alpha < 6$  in linear scale, and the vertical axis indicates  $1/q(\alpha)$ , which satisfies  $\hat{\eta}_{I,opt}^* = \lfloor 1/q(\alpha) \rfloor$ , in log scale. In the figure, the curve with the solid line indicates  $1/q(\alpha)$  with  $\tau = 1$ , while the dashed and dotted curves correspond to the graphs of  $1/q(\alpha)$ , when  $\tau = 10$  and  $100$ , respectively. As shown in the figure, as  $\alpha$  increases, all the three curves increase, which confirms our analysis.

#### 4.2.3.3 $\hat{M}_{I,opt}^*$ and $\tau$

Based on (19), we can find that  $\hat{\eta}_{I,opt}^*$  decreases as  $\tau$  increases for the interference-limited case. To prove this, we need to show  $\hat{M}_{I,opt}^*$  is increasing when  $\tau$  increases. Hence, if we differentiate  $q$ , which is defined in the previous subsection, with respect to  $\tau$ , it gives  $\frac{\partial q}{\partial \tau}$  as

$$\frac{\partial q}{\partial \tau} = \frac{2^{\alpha+2} \left( \frac{2^{\alpha+2}\tau}{\alpha-2} \right)^{-1+\frac{1}{\alpha-2}}}{(\alpha-2)^2}, \quad (21)$$

which is always positive for  $\tau > 0$  and  $\alpha > 2$ . Therefore,  $q$  is a increasing function of  $\tau$ , and  $\hat{M}_{I,opt}^*$ , which is equal to ceiling of  $q$ , is increasing or kept to be the same (by the ceiling), as  $\tau$  increases. This behavior is also shown in Figure 12, where the heights of the curves indicating  $1/q(\alpha)$ , decrease, as  $\tau$  increases. Therefore, as  $\tau$  increases, the corresponding broadcast throughput  $\hat{\eta}_{I,opt}^* = \lfloor 1/q(\alpha) \rfloor$  decreases.

#### 4.2.3.4 Comparison with Numerical Results

Table 2 compares the bound,  $\hat{M}_{I,opt}$ , which corresponds to the *original* lower bound of the broadcast throughput using (77), with the asymptotic bound,  $\hat{M}_{I,opt}^*$ , in (18) assuming the interference-limited case. In the table, the four rows correspond to  $\alpha = 2.5, 3, 3.5$ , and  $4$ , while the first four columns represent  $\bar{P}_r = 3, 30, 300$ , and  $3000$ , and the last column corresponds to  $\hat{M}_{I,opt}^*$  for the interference-limited case, when  $\tau = 1$ . The numerical results in the table show that  $\hat{M}_{I,opt}$  decreases as  $\alpha$  increases, which gives higher lower bounds of the broadcast throughputs  $\hat{\eta}_{I,opt}$ . It is because more efficient spatial reuse is possible by

**Table 2:** Numerically computed minimum packet insertion periods  $\hat{M}_{I,opt}$  and  $\hat{M}_{I,opt}^*$  for  $\tau = 1$

	$\bar{P}_r$				
$\alpha$	3	30	300	3000	$\hat{M}_{I,opt}^*$
2.5	89615	2448	2086	2054	2050
3	214	37	35	35	34
3.5	37	13	12	12	12
4	17	8	8	8	8

the reduced co-channel interference level with the higher path loss exponent as shown in Section 4.2.3.2. On the other hand, the larger  $\bar{P}_r$  also results in the decrease of  $\hat{M}_{I,opt}$ , since  $\mathbf{S}_{LB}$  increases relatively more than  $\mathbf{I}_{UB}$  by their relative distance gap of the signal source and interfering OLAs. Moreover,  $\hat{M}_{I,opt}^*$  based on the SIR instead of the SINR is very close to  $\hat{M}_{I,opt}$  when  $\bar{P}_r = 3000$ . However, because the noise is ignored, it always holds that  $\hat{M}_{I,opt}^* \leq \hat{M}_{I,opt}$ .

Moreover, the analysis about the impacts of  $\alpha$  and  $\tau$  on the broadcast throughput can be applied to the finite but large enough disk networks, where it takes a large number of hops to reach the network edge as long as the interference dominates the noise power. Also, we will observe the identical trends in the effects of  $\alpha$  and  $\tau$  in the numerical results in Sections 4.4.2 and 4.4.3.

### 4.3 Numerical Results with the Finite Disk Network in Free Space ( $\alpha = 2$ )

In this section, we studies whether the broadcast throughput in finite networks can be improved by spatial pipelining with the free space path attenuation (i.e.,  $\alpha = 2$ ) by numerical results. To be specific, by using ten-packet examples, where the ten packets are spatially pipelined using the same channel, we will show that when  $\alpha = 2$  the spatial pipelining always degrades the broadcast throughputs both for the ring-expansion (i.e.,  $\mu < 2$ ) and constant-area-OLA cases (i.e.,  $\mu = 2$ ). In a finite network, the interference from the preceding packet to the following packet does not last forever, because there is no more co-operative forwarding of the preceding packet after it reaches the edge of the network. For

example, suppose the OLA broadcasts of a single packet take exactly  $M_0$  hops to reach the edge of the network of radius  $R$ . The radius of the disk network  $R$  satisfies  $R^2 = P_s M_0 / \tau$  when  $\mu = 2$ , and  $R^2 = \frac{P_s(\mu-1)}{\tau(\mu-2)} \left(1 - \frac{1}{(\mu-1)^{M_0}}\right)$  when  $\mu < 2$  [19]. In this case, if we send multiple packets “without” pipelining, the OLA broadcast of each packet will take  $M_0$  time units, so the broadcast throughput  $\eta = 1/M_0$  because the minimum packet insertion period  $M$  without causing intra-flow interference is  $M_0$ .

On the other hand, if Packet 2 is inserted  $M = M_0 - l$  time slots after Packet 1, where  $1 \leq l < M_0$ , the receivers of Packet 2 would experience interference from the first packet just for the first  $l$  time units, and the packet would propagate without the interference until the third packet comes into the network. The question is whether we can use this interference-free time and do broadcast pipelining, to ultimately improve the broadcast throughput  $\eta$ , which is defined by  $1/M$  for the no packet loss case. However, even in this case, when  $\alpha = 2$ , we will show that pipelined OLA broadcasting does not improve the network throughput because the following packet hop-distances become shorter, which finally causes the packet loss. We will show examples using that the packet loss always occurs with ten packets for  $\alpha = 2$ . In particular, spatial pipelining can be used with  $3 \leq M \leq M_0 - 1$ . In this range, the intra-flow interference increases as  $M$  decreases, because smaller  $M$  means the shorter inter-packet distances. To maximize the broadcast throughput  $\eta$ , we need to find the minimum  $M_{R,opt}$  that does not cause any packet loss.

Therefore, as the minimum requirement for the feasibility of spatially pipelined OLA broadcasts,  $M = M_0 - 1$  should not cause packet loss for the spatial pipelining. In this case, we insert the second packet at  $t = M_0 - 1$ , so the two packets coexist on the network, and interfere with each other, for just one time slot (in fact, it can be a little more than one time slot, when the first packet becomes slower by the second packet). The intra-flow interference during this one time unit overlap changes the last ( $M_0$ th) hop-distance of the first packet, and also shortens the first hop-distance of the second packet. In particular, the outer boundary of the second packet is the  $r$  satisfying  $\text{SINR}_{(2;1)}(r) = \frac{P_s/r^2}{1+P(r \leftarrow \bigodot_{(1;M-1)})} = \tau$ .



Therefore, the initial step of the second packet is smaller than the initial step of the first packet. The small size of the first OLA has a lasting effect; all the second-packet OLA boundary radii will be smaller than their first-packet counterparts. Therefore, the second packet takes at least one more hop than  $M_0$  to reach the edge. Furthermore, the third packet inserted at  $t = 2M_0 - 2$  will hurt the radial hop-distance of the second packet, too.

The following numerical results show the effects of this co-channel interference with ten packets. However, because the distances between the packets or OLA step sizes can be an arbitrarily small positive number, the path loss function simply defined by  $l(d) = 1/d^\alpha$  does not hold for very small  $d$  [64]. As in [19], for the numerical evaluations in this dissertation, we separate the path loss function depending on  $d$  to avoid unrealistically inflated received power, which is given by

$$l(d) \triangleq \begin{cases} 1/d^\alpha, & d \geq 1, \\ 1, & d < 1. \end{cases}, \quad (22)$$

where  $d$  is the normalized distance by  $d_0$ .

#### 4.3.1 Ten-Packet Example

In this section, we show the numerical results of the OLA broadcast with ten packets for  $P_s = 10$  and  $\tau = 1$  using a pair of graphs. Figure 13 belongs to the ring expansion case with  $\mu = 1.8$  and the radius of the network  $R = 300$ . In the figure displays the traces of all the 10 packets on the graph of time versus distance, where the horizontal axis is the time and the vertical axis represents the radial distance (from the source to the edge of the network  $R$ ). Also, each curve indicates the propagation pattern of each packet ( $r_{(i;k)}$ , where the packet index  $i$  is from one to ten), on which the number with the bold font is the final hop count determined either by *i*) the packet reaches the edge of the network or *ii*) the packet quits propagating in the middle of the network.

With the given parameters, the single-packet OLA broadcasts take 35 hops to reach the edge of the network, which means  $M_0 = 35$ . If we use the packet insertion period  $M = 35$ ,

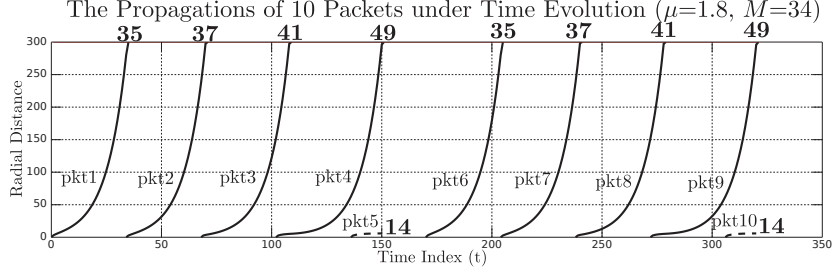
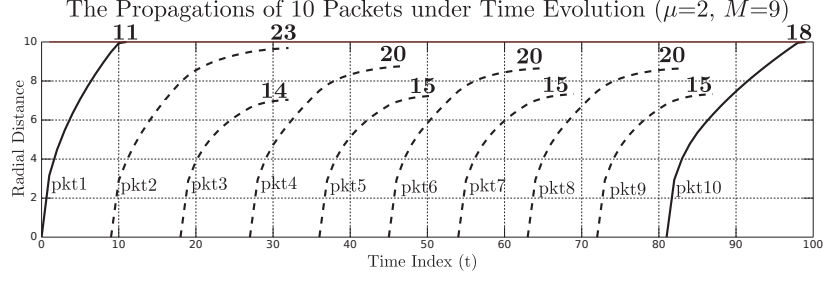


**Figure 13:** The time evolution of the distances, when  $\mu=1.8$ ,  $M=34$ ,  $M_0=35$ , and  $R=300$

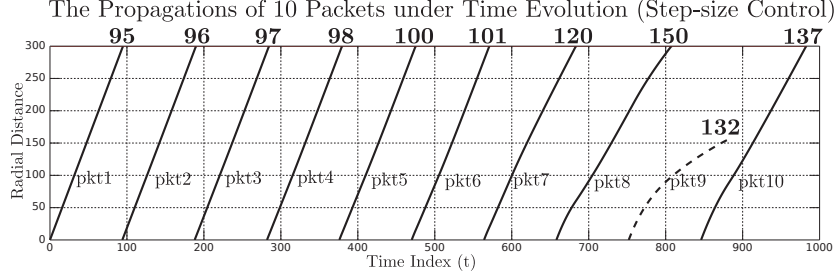
all the ten packets propagate identically with the final hop count of 35 because there is no intra-flow interference. On the other hand, the packet insertion period  $M$  in Figure 13 is  $34 = M_0 - 1$ , which is the marginal value for the spatial pipelining.

Figure 13 shows that from the second to the fourth packets, the hop counts increase because the lagging second packet interferes with the third more than the first packet interference with the second. The effect sequentially causes more severe reductions in the hop-distances of the packets, until the fifth packet is lost; however, after that, the same pattern is repeated by the next five packets (from six to ten). The slopes of the first to fourth packets are decreasing as the packet index increases, and finally the fifth packet is killed. It is a surprising result in that shortening the packet insertion period by just one slot, to  $M = M_0 - 1$ , makes multiple-packet pipelining impossible to achieve (i.e., the packet loss is not avoidable).

Figure 14 shows the case of  $\mu = 2$ , which does not have the ring expansion property. Because the relay power corresponding to  $\mu = 2$  is much lower than the  $\mu = 1.8$  case of Figure 13, we reduce  $R$  to 10, where the single-packet OLA broadcasts take 10 hops (i.e.,  $M_0 = 10$ ). As before, the numerical results in Figure 14 are obtained with  $M = M_0 - 1 = 9$  as the minimum requirement for spatial pipelining. As shown in the figure, eight of the ten packets stop propagating in the middle of the network, which is much worse than the ring expansion case. The reason is that the OLAs transmitting the leading and following packets are more balanced in size and not so far from each other, causing significant interference in both directions.



**Figure 14:** The time evolution of the distances, when  $\mu=2$ ,  $M=9$ ,  $M_0=10$ , and  $R=10$



**Figure 15:** The time evolution of distances with step-size control, when  $M=95$ ,  $M_0=94$ , and  $R=300$

This example results show that when  $\alpha = 2$ , packet loss happens even with ten packets and the marginal packet insertion period of  $M = M_0 - 1$ . Therefore, it is not possible to improve the broadcast throughput by spatial pipelining. Rather, it hurts the broadcast throughput by causing the side effects of the intra-flow interference such as degraded hop-distances and packet loss. Also, this overhead of spatial pipelining would become more significant for faster insertion rates with  $M < M_0 - 1$  or more packets.

#### 4.3.2 Step-size Control

Because the large size of the OLAs of the first packet can be blamed for shortening the second-packet hop-distances, we wondered if constraining OLA sizes would help the situation. It is straightforward to do power control as a function of hop count, to make OLA outer radii equally spaced. This “*step-size control*” approach was proposed in [5] for the purpose of regulating OLA sizes on the route reply phase of an OLA-based reactive routing scheme. In the single-packet OLA broadcasts, we can keep the same step-size of  $\sqrt{(P_s/\tau)} = r_k - r_{k-1}$

for  $k = 1, 2, \dots$  by setting the relay transmission power at  $k$ th OLA to

$$P_r(k) = \frac{\tau}{\pi\rho \ln\left(\frac{4k}{2k+1}\right)}, \quad (23)$$

which is readily derived by the OLA boundary condition that  $r_k = \sqrt{(P_s/\tau)k}$ .

This equal step-size control technique is useful to suppress the intra-flow interference by avoiding the ring expansion problem. Figure 15 shows the numerical results of the OLA broadcast with ten packets following the step-size control power adaptation, where the parameters are same to the numerical analysis in Figure 13. However, because of the reduced total transmit power by the step-size control, the single-packet OLA broadcasts take  $M_0 = 95$  hops, so we use one less packet insertion period of  $M = 94$  for the pipelining. Compared to the results in Figure 13, the impact of the pipelining is smaller in the step-size controlled network, which shows the packet loss of the ninth packet, even though the transmit power level of each relay is decreasing with hop index, to avoid the ring expansion. However, as in the previous fixed relay power examples, the step-size of each packet, which is indicated by the instantaneous slope of the curve, decreases from the first to the eighth packets. It can be also observed by the increasing total hop counts of the packets and the gradual slope variation in Figure 15. Thus, the step-size of the ninth packet is being suppressed to tiny levels, and it stops propagating at the 132th hop.

#### 4.4 Numerical Results with the Finite Network for Higher Path Loss Exponents ( $\alpha > 2$ )

For the finite disk networks, we showed numerically that the pipelined OLA broadcasts always degrade the broadcast throughput for  $\alpha = 2$ , because of the significant co-channel interference and packet loss by the pipelining. On the other hand, through the theoretical analysis assuming even the infinite-size network in Section 4.2, we showed that we can do spatial pipelining, when path attenuation is higher (i.e.,  $\alpha > 2$ ). For this reason, in this section, we investigate the broadcast throughput improvement by the spatial pipelining in finite networks for  $\alpha > 2$ . In contrast to the infinite disk network, the number of interfering

OLAs in a finite network is bounded by the size of the network, since the preceding packets finish propagation once they reach the edge.

Because spatial pipelining is feasible, now our interest is to find the minimum packet insertion period,  $M_{R,opt}$ , that does not cause packet loss, where  $R$  is a finite radius. Finding  $M_{R,opt}$  requires numerical calculations of the OLA boundaries  $r_{(i,k)}$  for the all packet indices  $i$  and levels  $k$  at each time unit. We find the  $M_{R,opt}$  by exhaustive search, testing whether there is packet loss for different  $M$  starting from 3. In Section 4.4.1, we first observe the propagation patterns of the pipelined OLA broadcasts with a 20-packet example, Then, Section 4.4.2 and 4.4.3 provide the numerically computed  $M_{R,opt}$  over the different system parameters  $\alpha$ ,  $\tau$ , and  $\bar{P}_r$ .

#### 4.4.1 Twenty-Packet Example in the Finite Disk Network

The following numerical results show the propagation patterns for  $\alpha = 2.5$  and 4 using the minimum packet insertion periods  $M_{R,opt}$  found by the exhaustive searches. Figure 16 shows the numerical results of twenty-packet OLA broadcast with  $\alpha = 2.5$ ,  $M = M_{R,opt} = 6$ ,  $\bar{P}_r = 30$  ( $\mu \approx 1.0107$ ),  $P_s = 30$ , and  $\tau = 1$ , where the radius of the network  $R = 68000$ . For the single (or non-pipelined) packet OLA broadcast, it takes 50 hops to reach the network edge (i.e.,  $M_0 = 50$ ). The figure displays the traces of the twenty packets on the graph of time versus radial propagation distance. The numbers above the curves on the top of the graph mean the final hop counts of the 20 packets to reach the network edge.

The key observation in Figure 16 is that there is no packet loss, even though the propagation speeds become slower as the packet index increases by pipelining with  $M_{R,opt} = 6$ . Other observations include that the first packet shows the least impact with the final hop count of 51, which is just one hop count larger than the single-packet case  $M_0$ , because the first packet grows fast while it does not undergo intra-flow interference until the second packet is inserted. On the other hand, the final hop counts of the next 19 packets are much bigger, because the network is being filled with pipelined co-channel packets. Especially, Packets 2 to 10 have significantly large final hop counts, because the interference of Packet

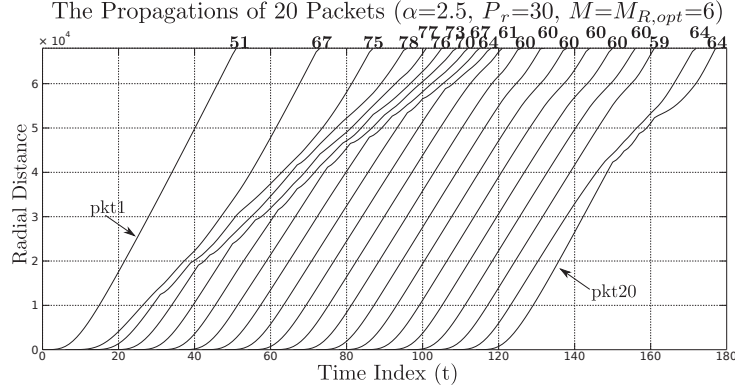


**Figure 16:** Numerical results with twenty packets for  $\alpha = 2.5$ , when  $M = M_{R,opt} = 6$ ,  $M_0 = 50$ , and  $R = 68000$

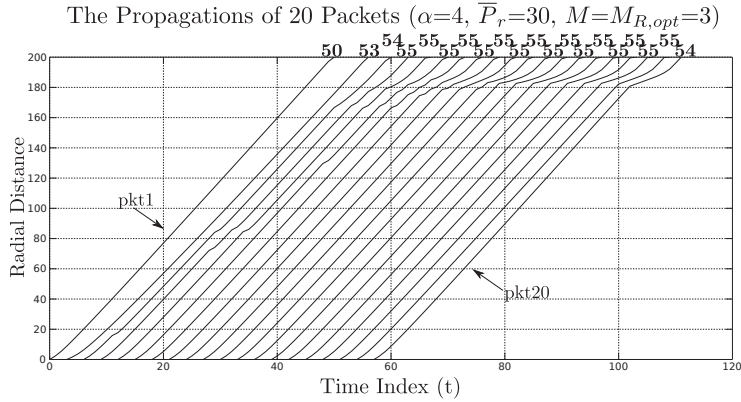


**Figure 17:** Numerical results with twenty packets for  $\alpha = 4$ , when  $M = M_{R,opt} = 3$ ,  $M_0 = 50$ , and  $R = 200$

1 dominates other interference and gives long-lasting impacts to the packets. On the other hand, after this transition, Packets 11 to 18 show quite stable propagation patterns without a sudden change in the slopes, which gives similar final hop counts. On the other hand, the last two packets (Packets 19 and 20) are relatively unstable, because Packet 20 does not have following packets, which is a favorable propagation environment. For that reason, Packet 20 propagates rapidly until it approaches very close to Packet 19. Then, the two packets interfere with each other and become slower.

Figure 17 shows the numerical results of  $\alpha = 4$  with  $R = 200$ , which is selected to obtain the same  $M_0 = 50$  as the previous case. Also, except the disk size  $R$ , the other parameters are kept to be the same as Figure 16 (i.e.,  $\bar{P}_r = 30$ ,  $P_s = 30$ , and  $\tau = 1$ ). The exhaustive search gives  $M_{R,opt} = 3$  for the given parameters, which is also the minimum of

$M$  under the half-duplex system assumption. As the previous example in Figure 16, none of the twenty pipelined packets quit propagating in the middle of the network. Compared to Figure 16, the slopes in Figure 17 are smaller considering the different vertical axis scale, because the path attenuation is larger. However, the propagation patterns of the packets in Figure 17 are more stable, and the slopes are less different than  $\alpha = 2.5$  case in Figure 16. These properties are because the higher path attenuation allows better spatial efficiency and less influence from the more distant co-channel interferers. For example, the throughput improvements by spatial pipelining in Figures 16 and 17 compared to the non-spatial pipelining cases (the ratios of  $M_0/M_{R,opt}$ ) are  $50/6$  ( $\approx 8.33$ ) and  $50/4$  ( $=12.5$ ), which correspond to  $\alpha$  of 2.5 and 4, respectively. Therefore, we can conclude that higher path attenuation allows higher throughput improvement by spatial pipelining from the non-spatial pipelining strategy.

Another interesting observation is that the slopes of Packet 3 to 20 vary significant around the edge  $R = 180$ , caused by the escape of the very preceding packet from the network. For example, after when Packet 3 reaches the edge, Packet 4 is suddenly accelerated, which makes the transmitting OLA size bigger. However, this sharp increase in Packet 4 works as a severe increase in interference to Packet 5, which degrades the propagation speed of Packet 5. For this reason, the following packets after Packet 5 sequentially undergo de-acceleration. Therefore, the packets propagate slower as they approach the network edge, but they suddenly leap forward after when the very preceding packet finishes the propagation. We observe this behavior with different network sizes  $R$ . Even though the slopes are not dramatically changing, we can see a similar behaviors partially in Figure 16.

We note that if the network size  $R$  increases,  $M_{R,opt}$  is likely to increase because the network would accommodate more number of co-channel packets, which would cause higher intra-flow interference. As a result, in general  $M_{R,opt}$  in the finite network is much smaller than the bound  $\hat{M}_{I,opt}$  derived for the infinite network in Section 4.2.3. For example,  $M_{R,opt}$  for  $\alpha = 2.5$  in Figure 16 is six, while the corresponding  $\hat{M}_{I,opt}$  in Table 2 is 2448. Also,

when  $\alpha = 4$ ,  $M_{R,opt}$  in Figure 17 is three, and  $\hat{M}_{opt}$  in Table 2 is eight. The gap between  $M_{R,opt}$  and  $\hat{M}_{I,opt}$  is bigger for lower  $\alpha = 2.5$ , because the interfering OLA areas are inflated in  $\text{SINR}_{LB}$  by integrating to infinity. However, in particular for large  $\alpha$  (e.g.,  $\alpha \approx 4$ ),  $\hat{M}_{I,opt}$  can be helpful to limit the range of the exhaustive search for  $M_{R,opt}$  by serving as an upper bound.

#### 4.4.2 Impacts of $\alpha$ and $\bar{P}_r$ on $M_{R,opt}$

In this section, we test the effects of the path loss exponent  $\alpha$  and the relay transmission power  $\bar{P}_r$  on the optimal packet insertion period  $M_{R,opt}$ . Figure 18 shows the numerical results with 20 packets,  $\tau = 10$  and  $M_0 = 50$  to compare the efficiency of the spatial pipelining (i.e.,  $R$  changes depending on the parameters). In the figure, the horizontal axis indicates  $\alpha = 2.5, 3, 3.5$ , and 4, while the vertical axis indicates  $M_{R,opt}$  obtained by the exhaustive search. Also, the solid and dotted lines represent  $M_{R,opt}$  with  $\bar{P}_r = P_s = 100$  and 400, respectively.

The both lines are decreasing as  $\alpha$  increases, which means we can achieve more efficient spatial reuse with the increase in the broadcast throughput by a factor of  $\frac{\eta_{R,opt}}{\eta_{M_0}} = \frac{M_0}{M_{R,opt}}$  for higher path attenuation. That is because the co-channel interference becomes less significant as  $\alpha$  increases, which is also identical to the theoretical analysis assuming the infinite network in Section 4.2.3.2. On the other hand, if looking at the heights of the two graphs on the same  $\alpha$ , the dotted line corresponding to  $\bar{P}_r = 400$  is always under the solid line, which represents  $\bar{P}_r = 100$ . In other words, the spatial reuse efficiency for higher relay transmission power is better. The reasons is again the relative distance of the signal source OLA and the co-channel interfering OLAs. To be specific, as  $\bar{P}_r$  increases, the resulting SINR also increases, since the signal power increase level is greater than the interference increase level even though both are growing. Also, we note that the height gap between the two graphs is the largest at  $\alpha = 2.5$ , which indicates the low  $\alpha$  case is more vulnerable to the drop in  $\bar{P}_r$ .



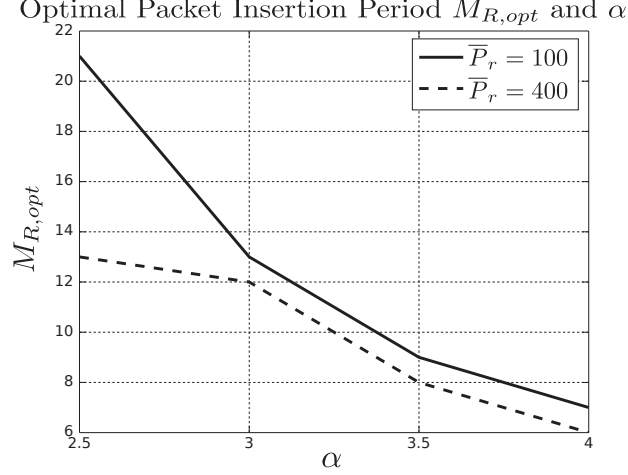


**Figure 18:** Numerical results for the different path loss exponents  $\alpha = \{2.5, 3, 3.5, 4\}$ , when  $M_0 = 50$ ,  $\tau = 10$ , and  $\bar{P}_r = P_s = \{100, 400\}$

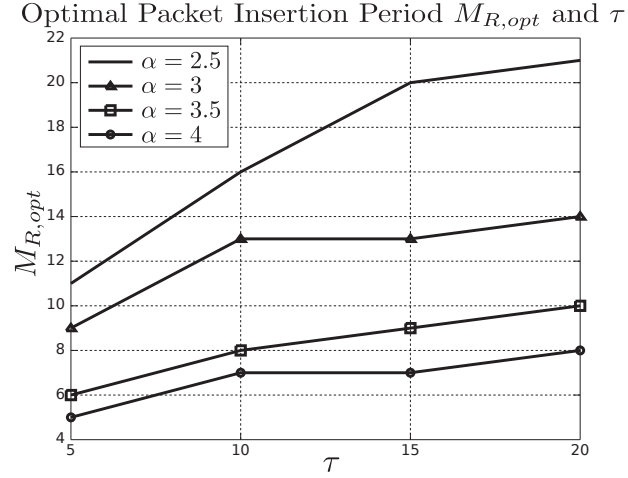


**Figure 19:** Numerical results for the different decoding thresholds  $\tau = \{5, 10, 15, 20\}$ , when  $\alpha = \{2.5, 3, 3.5, 4\}$ ,  $M_0 = 50$ , and  $\bar{P}_r = P_s = 300$

#### 4.4.3 Impacts of $\tau$ on $M_{R,opt}$

The final numerical results present how  $M_{R,opt}$  changes under the decoding threshold  $\tau = 5, 10, 15$ , and  $20$  with  $20$  packets,  $\bar{P}_r = P_s = 300$  and the radii  $R$  are chosen with  $M_0 = 50$  to compare the efficiency of the spatial pipelining as the previous comparison. Figure 19 shows the numerical results by the exhaustive search with the x-axis of  $\tau$  and the y-axis of  $M_{R,opt}$ , where the different lines indicate the different  $\alpha$ : the solid line without marker ( $2.5$ ), the triangle-marker line ( $3$ ), the square-marker line ( $3.5$ ), and the circle-marker line ( $4$ ). All the four lines show the increasing behavior (or keep the same level)  $M_{R,opt}$  of as  $\tau$

increases. This pattern results from a more demanding SINR condition as  $\tau$  grows, which limits the interference levels.

If comparing the heights of the four curves, the lower path-loss exponent gives higher  $M_{R,opt}$  for the same  $\tau$ . In other words,  $\alpha = 2.5$  shows the highest  $M_{R,opt}$ , and  $\alpha = 4$  gives the lowest  $M_{R,opt}$ . That is because the higher  $\alpha$  gives more significant improvement of the throughput by spatial pipelining as shown by the previous numerical results in Section 4.4.2, since the impact of the intra-flow interference decreases as  $\alpha$  grows, which is consistent with the analytical result in Section 4.2.3.2. Moreover, the curve with the higher  $\alpha$  shows more significant increases compared to the curve with the lower  $\alpha$ , as  $\tau$  increases. For example, as  $\tau$  increases, the solid lines with no marker and the triangle-marker, which indicate  $\alpha = 2$  and 2.5 respectively, show more increases of  $M_{R,opt}$  than the solid lines with the square- and circle markers, which represent  $\alpha = 3.5$  and 4, respectively. That is because higher path attenuation (i.e., higher  $\alpha$ ) makes the sensitivity to  $\tau$  smaller. This tendency is consistent with the infinite disk case based on the observation of  $q(\alpha) \approx \hat{M}_{I,opt}^*$  defined in Section 4.2.3.2, which is an approximation of the finite network with very large  $R$ . For example,  $\frac{\partial q}{\partial \tau}$  in (21), which indicates the sensitivity of  $\hat{M}_{I,opt}^*$  to  $\tau$ , is 20480, 32, 3.77834, and 1.26491 for  $\alpha = 2.5, 3, 3.5$ , and 4, when  $\tau = 5$ . Similarly, in Figure 12 in Section 4.2.3.2, the height gaps of the three curves corresponding to  $\tau = 1, 10$ , and 100, which also indicate the sensitivity of  $\hat{M}_{I,opt}^*$  to  $\tau$ , are wider for smaller  $\alpha$ .

However, the decreases in  $M_{R,opt}$  under the change in  $\tau$  is much less significant compared to  $\hat{M}_{I,opt}^*$ . For example, the  $M_{R,opt}$  curves with  $\alpha = 3$  and 4 do not change, when  $\tau$  increases from 10 to 15. That is because the network size is finite, which limits the number of co-channel packets in the network, while  $\hat{M}_{I,opt}^*$  assuming the infinite network is derived based on the highly inflated co-channel interference  $\mathbf{I}$  in (76) than its actual value. Moreover, because  $M_{R,opt}$  must be a positive integer, if the increase of  $\tau$  is not significant enough,  $M_{R,opt}$  does not change as the two cases (e.g., the curves with  $\alpha = 3$  and 4, when  $\tau$  increases from 10 to 15) shown in Figure 19.

The decoding threshold  $\tau$  depends on other various parameters (e.g., modulation order, packet size, and coding scheme) that change the data rate with non-trivial relationships. In this study, we limit our scope to the packet-level analysis as in [18] with the assumption that the parameters deciding  $\tau$  is fixed for a certain system.

## 4.5 Summary

In this chapter, we study the impact of the intra-flow interference on throughput in OLA broadcasts using the continuum and deterministic channel assumptions, which model the high node density situation. For the infinite disk network, we prove that the intra-flow interference of multiple OLA broadcasts discourages spatial reuse for free space path loss exponent  $\alpha = 2$ , because any co-channel pipelining causes shorter step sizes that greatly delay the second packet, and the further insertion of packets causes packet loss. On the other hand, for higher path attenuation with  $\alpha > 2$ , we theoretically show that the spatial pipelining is feasible and derive the lower bound of the broadcast throughput.

Numerical results with the finite network sizes confirm the theoretical analysis that spatial pipelining hurts the broadcast throughput for  $\alpha = 2$  by causing packet loss, while it improves the throughput and none of packets are lost when  $\alpha > 2$ , by taking advantage of spatial pipelining, which becomes more efficient as  $\alpha$  increases. Therefore, the results indicate that the multiple-packet transmission strategy for OLAs should be determined based on the path attenuation. When  $\alpha = 2$ , we suggest the best strategy is to wait to insert a packet until after the preceding co-channel packet has reached the edge of the network. On the other hand, if  $\alpha > 2$ , the broadcast throughput can be improved by the spatial pipelining, which verifies that OLA broadcasts can be an effective solution for multiple-packet transmissions in the high path attenuation environments. Lastly, this chapter shows the impact of the different system parameters on the optimal packet insertion period (i.e., the optimal broadcast throughput), which has the same trends both in the theoretical analysis in the infinite disk network and the numerical results in the finite disk network.

## CHAPTER 5

### MULTI-PACKET OLA TRANSMISSION ON STRIP-SHAPED COOPERATIVE ROUTES OR NETWORKS

#### 5.1 Signal Model of Intra-flow Interference

For simplicity to explain the signal model, suppose only two packets are transmitted: the second packet is transmitted by the source  $M$  time units after the first packet transmission. Figure 20 shows a part of a long strip network with the length of  $L$  and width of  $W$ . The shaded areas in Figure 20 indicate two OLAs that could be transmitting at the same time. Suppose the smaller one,  $\tilde{\mathcal{O}}_{(2;k)}$ , transmits the second packet in its  $k + 1$ st hop, and  $\tilde{\mathcal{O}}_{(1;k+M)}$ , transmits the first packet in its  $k + M + 1$ st hop. We are interested to know if receivers at Points  $A$  at  $(x_A, 0)$  and  $B$  at  $(x_B, 0)$  will be able to decode Packets 1 and 2, respectively. We note that  $x_{(1;k+M)} < x_A$  and  $x_{(2;k)} < x_B < x_{(1;k+M-1)}$ .

For the receiver at Point  $A$ , we have,

$$\text{SINR}_{(1;k+M+1)}(x_A) = \frac{\mathbf{S}}{\mathbf{I} + \mathbf{N}} = \frac{P(\tilde{\mathcal{O}}_{(1;k+M)} \rightarrow x_A)}{P(\tilde{\mathcal{O}}_{(2;k)} \rightarrow x_A) + 1}. \quad (24)$$

We will assume that if this SINR is greater than  $\tau$ , the receiver can decode. For the receiver at Point  $B$ , the interference comes from  $\tilde{\mathcal{O}}_{(1;k+M)}$ , which is to the right of Point  $B$ . Thus, for the receiver at Point  $B$ , the SINR is

$$\text{SINR}_{(2;k+1)}(x_B) = \frac{P(\tilde{\mathcal{O}}_{(2;k)} \rightarrow x_B)}{P(\tilde{\mathcal{O}}_{(1;k+M)} \rightarrow x_B) + 1}. \quad (25)$$

Therefore,  $x_A = x_{(1;k+M+1)}$  satisfies  $\text{SINR}_{(1;k+M+1)}(x_A) = \tau$ , while  $x_B = x_{(2;k+1)}$  satisfies  $\text{SINR}_{(2;k+1)}(x_B) = \tau$ .

#### 5.2 Multi-packet Propagation for the Finite Strip

In this section, we explore the properties in multi-packet OLA propagations along a strip network of finite length, using numerical analysis. The results motivate the theoretical approach for the infinite strip case in the following section.

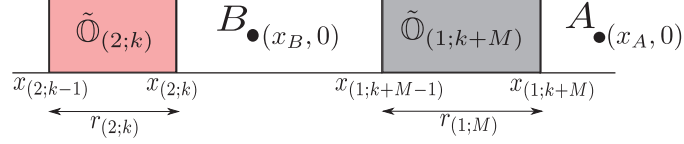


**Figure 20:** The snapshot of multiple-packet OLA broadcast

As an example to show the impact of the co-channel interference, we numerically calculate the propagation dynamics with  $\alpha = 2$ ,  $P_s = 100$ ,  $\overline{P_r} = 100$ ,  $\tau = 10$ ,  $W = 1$ , and  $L = 200$ . Even though  $\alpha = 2$  is used in this example, we note that the following properties in this section are common for any  $\alpha \geq 2$ . If the source sends only one packet, there is no intra-flow interference. For the given parameters, a single packet takes 41 hops for the single packet to reach the destination by OLA transmission, which we denote by  $M_0 = 41$ . Therefore, with a fixed packet insertion period  $M$ , if the source injects new packets, interference will occur if  $M < M_0 = 40$ ; we refer to this situation as *spatial pipelining*.

Figure 21 shows the numerical results of the OLA transmission with ten packets for  $M = 10$ , where the x-axis indicates time, and the y-axis denotes the propagation distance in terms of the horizontal distance from the source ( $x_{(i;k)}$  in Figure 7). The ten black solid curves represent the OLA propagations of the ten packets as time evolves, while the red dashed lines are the reference curves showing the interference-free (or the single-packet OLA transmission) situation that we denote by  $x_{(0;k)}$ . The numbers with the bold font on the black curves indicate the final hop-counts when the packets finish propagations. Also, the slopes of the black curves in the figure mean the step-sizes  $r_{(i;k)} = x_{(i;k)} - x_{(i;k-1)}$ , while the slope of the red curve indicates the interference-free step-sizes  $r_{(0;k)} = x_{(0;k)} - x_{(0;k-1)}$ . Figure 22 shows the numerical results of a shorter packet insertion period of  $M = 5$ , where we observe that Packets 3, 6, and 8 are lost, because they quit propagating.

### 5.2.1 Upper Bounds on Hop-Counts and Step-sizes

Because of the co-channel interference, the step-sizes of the pipelined OLA transmission are smaller than the step-sizes of the single-packet OLA transmission, where co-channel interference does not exist. In Figures 21 and 22, the step-size decrease causes the slope

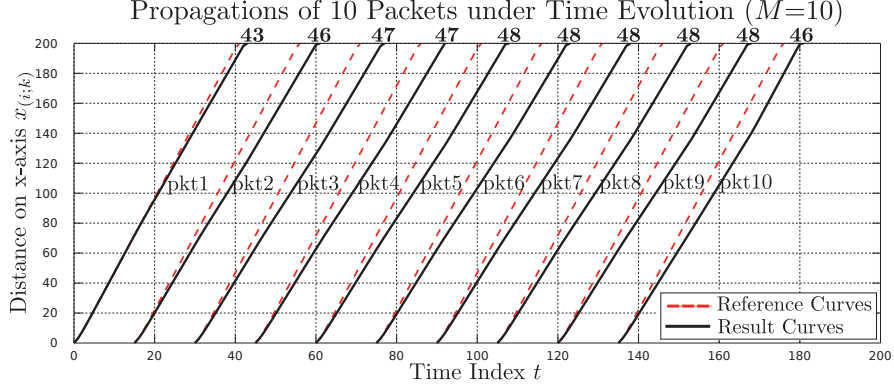


**Figure 21:** The time evolution of the hop distances, when  $M = 10$

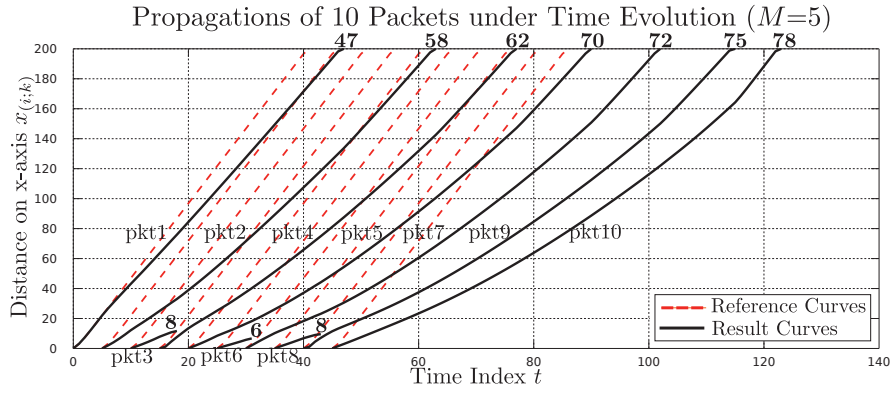


**Figure 22:** The time evolution of the hop distances, when  $M = 5$

of the black curves to be lower than the red dashed curves. Also, because  $x_{(i;k)}$  is the accumulated value of the step-sizes, it is bounded by  $x_{(0;k)}$ . Therefore, regardless of the packet insertion period,  $r_{(i;k)} \leq r_{(0;k)}$  and  $x_{(i;k)} \leq x_{(0;k)}$  always hold. This property is important to estimate the range of the OLA boundaries, which is required to numerically calculate the SINR equation. Because  $x_{(i;k)} \leq x_{(0;k)}$  always holds, the final hop-counts of the packets in Figures 21 and 22 are greater than  $M_0 = 40$  except the packet loss cases in Figure 22.

### 5.2.2 Packet Insertion Period

If the final hop-count at the destination for the single-packet case is  $M_0$ , the range of the packet insertion period  $M$  for the spatial pipelining is  $3 \leq M \leq M_0 - 1$ , assuming a half-duplex system. In this range, the intra-flow interference increases as  $M$  decreases, because a smaller  $M$  means the shorter inter-packet distances. However, if  $M$  is too small, some packets die off in the middle of the network as do Packets 3, 6, and 8 in Figure 22, because

the inter-packet spacing is not enough to keep the SINR above the decoding threshold  $\tau$ . As indicated by the decreasing slopes of Packets 3, 6, and 8, the step-sizes  $r_{(i,k)}$  of the three packets gradually decrease as hop goes. Since the received power is proportional to the area of the transmitting (i.e., current-hop) OLA, the smaller step-size of the current hop makes the step-size of the next hop even smaller. At the same time, as the step-sizes of Packets 3, 6, and 8 decrease, the SINRs of their neighboring co-channel packets (Packets 2, 4, 5, 7, and 9) increase, since the interferences from Packet 3, 6, 8 become smaller. For this reason, the three packets finally stop propagating right after the time when their OLA sizes become too small to exceed the decoding threshold. Because this packet loss results in a waste of time and energy, which reduces the throughput, it is significant to choose the appropriate  $M$  to maximize the network throughput without causing any packet loss. Also, while Figure 22 shows the time-varying slopes, the slope of each packet curve in Figure 21 is almost stable, because the step-size change between adjacent hops is very small.

### 5.2.3 Worst-Case Packet

Depending on the packet index, packets have different propagation patterns in terms of the hop distance and hop-count. As long as no packets are lost, the first packet always shows the fastest propagation, because it does not experience interference until the second packet comes into the network. For a similar reason, the first and last few packets undergo relatively less interference, because the numbers of their co-channel packets are smaller compared to the packets with the intermediate indices. For example, in Figure 21, among the ten packets, Packet 1 shows the smallest final hop-count of 43, and its slope in Figure 21 is also the highest. Packets 2 and 10 also show the relatively smaller hop-counts of 46, while Packet 5 to 9 have 48. If looking at the curve of Packet 5 in Figure 21, the instantaneous slope is minimized around when  $x_{(5,k)} \approx 100$ , which is the horizontal mid-point of the strip network. Suppose there are three consecutive co-channel packets along a strip network as a simplified example. Among the three packets, the one in the middle always has the highest total interference. In conclusion, if no packets are lost, a packet experiences the highest

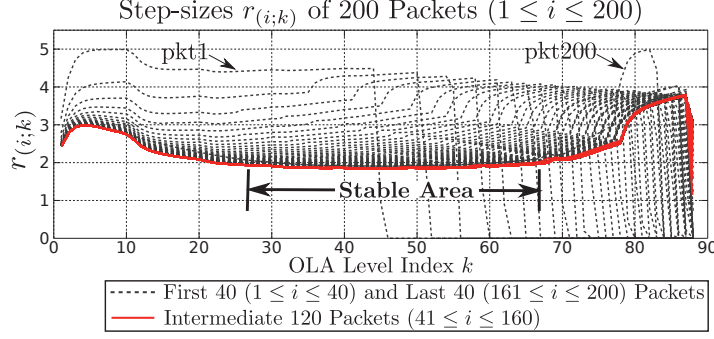


**Figure 23:** The overlapped step-sizes  $r_{(i;k)}$  curves of 200 packets

interference, when it is the middle one of the sequence (i.e.,  $i \approx 50$ , if the total number of packets is 100), and when it is in the middle of the strip (i.e.,  $x_{(i;k)} \approx L/2$ ).

#### 5.2.4 Stable State with Equal Step-size

For multiple-packet OLA transmission in the finite-length strip networks, the steady-state of the single-packet propagation is perturbed, when a new following packet is inserted or a preceding packet reaches the destination. In this situation, there are two kinds of perturbation factors in terms of the packet index and the location in the network. To be specific, for a large enough network length  $L$  and a large number of packets  $n$ , the first and last few packets show the different propagation patterns from the packets with the intermediate indices, because the network is not fully filled with multiple co-channel packets when the first and last few packets propagate. Also, the packets with the intermediate indices reach a *stable state* with an almost equal step-size in the middle area of the network (the neighborhood of the network mid-point:  $x_{(i;k)} \approx L/2$ ), where the packets are less affected by the new insertion of the following packets and the exit of the preceding packets at the both ends.

As an example, Figure 23 shows the step-sizes of multiple packets with the horizontal axis of the OLA level index  $k$  and the vertical axis of the step-sizes  $r_{(i;k)}$ , which are numerically computed with 200 packets. The other parameters are identical to Figure 21 (i.e.,  $\alpha = 2$ ,  $P_s = 100$ ,  $\overline{P_r} = 100$ ,  $\tau = 10$ ,  $W = 1$ ,  $L = 200$ , and  $M = 10$ ). In the figure, the first 40 and last 40 packets, which have the packet indices  $1 \leq i \leq 40$  and  $161 \leq i \leq 200$ , are indicated by the black dotted lines, while the intermediate 120 packets, which have the



indicated  $41 \leq i \leq 160$ , are indicated by the red solid lines. All the 200 packets (both the black dotted line and red solid lines) show the flat bowl-shaped curves, excluding the sudden drops of the final step-size clipped by the network edge, because the numbers of the neighboring co-channel packets are smaller around the both ends as explained in the previous section, which makes the propagation speed faster around the network boundaries than the propagation speed in the middle area of the strip.

However, the overlapped curves of the 200 packets are quite different in terms of the total hop-counts and the fluctuation levels, which are indicated by the widths and heights, respectively. On the other hand, the red solid curves representing the 120 packets with the intermediate indices ( $41 \leq i \leq 160$ ) show almost the same pattern, if excluding the black dotted curves indicating the packets that experience a partially filled network (i.e.,  $1 \leq i \leq 40$  and  $161 \leq i \leq 200$ ). Also, the middle area of the overlapped red curves has relatively stable heights, where  $r_{(i;k)}$  does not change significantly for different OLA level index  $k$ , because it is physically far from the both ends and less affected by the perturbations from the network boundaries (i.e.,  $x_{(i;k)} \approx 0$  or  $L$ ). This observation is the motivation for our analytical approach in the next section. If both the number of packets  $n$  and the network length  $L$  go to infinity, the throughput performance should be governed by this stable state with a fixed step-size propagation.

This stable state can be found by observing the step-sizes of consecutive packets. Numerically, we can start searching from the mid-sequence packet  $i' = N/2$ , by picking its OLA level  $k'$ , the boundary of which is closest to the mid-point of the network (i.e.,  $x_{(i';k')} \approx L/2$ ). Then, the stable state range in terms of the OLA level, which is denoted by  $k_{min} \leq k \leq k_{max}$ , for the same packet  $i'$  can be defined by the indices  $k$  that have almost equal step-sizes  $|r_{(i';k)} - r_{(i';k')}| < \epsilon$  with a certain  $\epsilon \approx 0$  (e.g.,  $0.01 \cdot r_{(0;k')}$ , where  $r_{(0;k')}$  is the interference-free step-size). After that, the stable state range across different packets can be found by searching the packet indices  $i$  that satisfy  $|r_{(i;k)} - r_{(i';k)}| < \epsilon$  for the same  $k_{min} \leq k \leq k_{max}$ .

### 5.3 Spatial Pipelining in the Infinite Strip Network

In this section, we consider the spatially pipelined OLA transmission for the infinite-length strip network in presence of co-channel interference from the preceding and following packet OLAs. The “infinite” network is a theoretical concept, but it provides an intuition to explain the multi-packet OLA transmission in a large network, where a large number of hops are required for a packet to reach the destination.

#### 5.3.1 Feasibility of Spatial Pipelining

If the spatial pipelining in the infinite network is feasible, there should be a finite packet insertion period  $M$  that does not cause packet loss for infinitely many packets on the fly. This feasibility issue can be proved by showing that the simultaneously transmitted co-channel packets are at-least-linearly propagating down the strip. The core idea used in the proof (at-least-linearly propagating OLAs) is the same as [16], which proves the feasibility in the *disk-shaped network* with *interference cancellation* from the preceding packets. In the following, we extend this result to strip networks and no cancellation.

**Theorem 4** *For finite  $\tau$  that is small enough compared to the transmission powers  $\overline{P}_r$  and  $P_s$ , an infinite number of the spatially pipelined packets are feasible to propagate at least linearly with a fixed step-size  $\Delta$  for a finite packet insertion period of  $M$ , without causing packet loss in the infinite-length strip network.*

The proof is shown in Appendix E.

#### 5.3.2 Lower Bound of Optimal Throughput for the Interference-limited Case

The most important issue in the pipelined OLA transmission is the selection of  $M$ ; we want the smallest value of  $M$  that causes no packet loss, so the throughput  $\eta = 1/M$  is maximized. Suppose  $M_{I,opt}$  is the minimum packet insertion period  $M$  for given parameters such as  $\alpha$ ,  $\overline{P}_r$ ,  $\tau$ , and  $W$ , with which the spatially pipelined OLA transmission with infinitely many co-channel packets is sustained in the infinite network. Then, if  $\hat{M}_{I,opt}$  is the minimum  $M$

that satisfies the inequality in (81),  $M_{I,opt} \leq \hat{M}_{I,opt}$  always holds, and the corresponding throughputs satisfy  $\eta_{I,opt} \geq \hat{\eta}_{I,opt}$ . Therefore, we can find the lower bound of the throughput  $\hat{\eta}_{I,opt} = 1/\hat{M}_{I,opt}$  using (81).

However, it is difficult to solve (81), because there are too many variables. The number of variables can be reduced by letting  $\bar{P}_r \rightarrow \infty$ , where the interference is significantly greater than the noise power. In the limit,  $\mathbf{SINR}_{LB}$  in (81) becomes

$$\mathbf{SINR}_{LB} = \frac{\mathbf{S}_{LB}}{\mathbf{I}_{UB}} = \frac{(\alpha - 1)(M - 2)^{\alpha-1}}{2^{\alpha-1}}. \quad (26)$$

If we solve  $\mathbf{SINR}_{LB} \geq \tau$ , it gives the minimum packet insertion period as

$$\hat{M}_{I,opt}^* = \left\lceil 2 \left( \frac{\tau}{\alpha - 1} \right)^{\frac{1}{\alpha-1}} \right\rceil + 2, \quad (27)$$

where the ceiling is because  $\hat{M}_{I,opt}^*$  is a positive integer, which is a function of just two parameters:  $\alpha$  and  $\tau$ .

### 5.3.2.1 $\hat{M}_{I,opt}^*$ and $\alpha$

In the single-shot (or single-packet) transmission, the higher path loss exponent  $\alpha$  degrades the propagation speed of the packet, but for the multiple-packet transmission with spatial pipelining, the higher  $\alpha$  can be beneficial, because the spatial reuse becomes more efficient as  $\alpha$  grows. The following corollary proves the improvement of throughput resulted by the better spatial reuse with higher  $\alpha$ .

**Corollary 1** *For the interference-limited case, the lower bound of the throughput  $\hat{\eta}_{I,opt}^*$ , which is equal to  $1/\hat{M}_{I,opt}^*$ , increases as  $\alpha$  increases for  $1 < \alpha \leq 1 + e^\tau$  when the decoding threshold  $\tau$  is fixed.*

*Proof:* For simplicity, excluding the ceiling on the right hand side in (27), we define a function  $q(\alpha) = 2 \left( \frac{\tau}{\alpha-1} \right)^{\frac{1}{\alpha-1}} + 2$ , which is less than or equal to the original term with the

ceiling. If we differentiate  $q(\alpha)$  with respect to  $\alpha$ , we have  $q'(\alpha) = \frac{\partial q}{\partial \alpha}$  as

$$q' = -2 \left[ \frac{\ln\left(\frac{\tau}{\alpha-1}\right) + 1}{(-1 + \alpha)^2} \right] \left(\frac{\tau}{\alpha-1}\right)^{\frac{1}{\alpha-1}}, \quad (28)$$

where the solution of  $q'(\alpha) = 0$  is  $1 + e^\tau$ . The second derivative  $q''(\alpha) = \frac{\partial^2 q}{\partial \alpha^2}$  to test the concavity is given by

$$q'' = 2 \left(\frac{\tau}{\alpha-1}\right)^{\frac{1}{\alpha-1}} \left[ \frac{3 + 2 \ln\left(\frac{\tau}{\alpha-1}\right)}{(\alpha-1)^3} + \frac{\left(1 + \ln\left(\frac{\tau}{\alpha-1}\right)\right)^2}{(\alpha-1)^4} \right]. \quad (29)$$

Because  $q''(\alpha = 1 + e^\tau) = 2 \cdot \exp(-3 - \frac{1}{e^\tau})/\tau^3$  is always positive, the function  $q(\alpha)$  is minimized at  $\alpha^* = 1 + e^\tau$ . Moreover, because  $q'(\alpha) < 0$  when  $1 < \alpha < \alpha^*$ ,  $q(\alpha)$  decreases as  $\alpha$  increases. With the ceiling as in (27),  $\hat{M}_{I,opt}^*$  decreases or stays the same, as  $\alpha$  increases. Hence, in this range, the lower bound of the throughput  $\hat{\eta}_{I,opt}^*$  increases, as  $\alpha$  increases.  $\square$

As a practical example, we assume  $\tau > 1$ , which corresponds to the class of bandwidth-efficient waveforms for large file transfer [57]. Specifically,  $\alpha^* \approx 3.718$  for  $\tau = 1$ , and  $\alpha^* \approx 8.389$  for  $\tau = 2$ . Therefore, in the practical ranges of  $\tau$  and  $\alpha$ , the lower bound of the throughput  $\hat{\eta}_{I,opt}^*$  increases, as  $\alpha$  increases, which confirms the better spatial reuse for higher  $\alpha$ .

### 5.3.2.2 $\hat{M}_{I,opt}^*$ and $\tau$

The decoding threshold  $\tau$  is a important parameter that determines the required inter-packet separation, the increase of which makes the throughput decrease, for the sustained OLA transmission with multiple packets. The following corollary shows the impact of  $\tau$  on the lower bound of the throughput  $\hat{\eta}_{I,opt}^*$  for the interference-limited case.

**Corollary 2** *For the interference-limited case with  $\bar{P}_r \rightarrow \infty$ , the lower bound of the throughput  $\hat{\eta}_{I,opt}^*$  decreases as  $\tau$  increases.*

*Proof:* We must show  $\hat{M}_{I,opt}^*$  increases when  $\tau$  increases. Hence, if we differentiate  $q$ , which is defined in Corollary 1, with respect to  $\tau$ , we have  $\frac{\partial q}{\partial \tau}$  as

$$\frac{\partial q}{\partial \tau} = \frac{2\left(\frac{\tau}{\alpha-1}\right)^{\frac{2-\alpha}{\alpha-1}}}{(\alpha-1)^2}, \quad (30)$$

which is always positive, when  $\tau > 0$  and  $\alpha > 1$ . Therefore,  $q$  is a increasing function of  $\tau$ . Hence,  $\hat{M}_{I,opt}^*$ , which is equal to ceiling of  $q$ , increases or stays the same (by the ceiling), as  $\tau$  increases.  $\square$

We note that while the increase in  $\tau$  reduces the packet insertion rate at the source, the network capacity and transmission rate, which is defined as  $R = \log_2(1 + \tau)$  in [16], increases, when  $\tau$  increases. For example, when  $\tau$  increases, we can use higher-order modulation or increase the packet size. However, we limit our scope to the packet-level analysis (i.e., how often we can insert the packet at the source) following [18].

The two corollaries can be applied to the finite network with large enough  $L$ , where a large number of hops are required to reach the edge of the network, as long as the interference is significantly greater compared to the unit noise power. In the numerical results with the finite networks in Section 5.5, we observe the identical trends of the throughput depending on  $\alpha$  and  $\tau$ .

## 5.4 Optimal Packet Insertion Period in the Finite Network

In this section, we investigate the throughput optimization for finite strip networks that has a finite length  $L$ . However, we still focus on large enough length  $L$ , where the final hop-count of the single-packet OLA transmission,  $M_0$ , is large. Otherwise, it is a trivial problem, and there is not a significant advantage of the spatial pipelining compared to the simple OLA transmission with  $M = M_0$  (no-spatial pipelining).

Finding the optimal packet insertion period  $M_{L,opt}$  (the minimum  $M$  that does not cause packet loss for finite  $L$ ) requires numerical calculation of the OLA boundaries  $x_{(i,k)}$  for the

all packet indices  $i$  and levels  $k$  at each time unit. Also, this numerical calculation should be repeated for different  $M$  starting from 3, to see whether there is packet loss. To limit this exhaustive search of  $M_{L,opt}$ , we might use  $\hat{M}_{L,opt}$  in Section 5.3, which corresponds to the lower bound of the throughput in the infinite network. However, the interference term in  $\hat{M}_{L,opt}$  is so highly inflated by integrating the infinitely many co-channel OLAs that  $\hat{M}_{L,opt}$  actually makes an excessively loose upper bound in the finite strip case. Therefore, we propose a new upper bound of  $M_{L,opt}$  assuming  $\alpha = 2$ , which give an appropriate range for the exhaustive search by *equal step-size* approximation based on the observations in Section 5.2. This upper bound is derived using the sustained single-packet OLA transmission condition in [21] for the free space path loss ( $\alpha = 2$ ). Moreover, because  $M_{L,opt|\alpha=2} \geq M_{L,opt|\alpha>2}$  by the increased spatial reuse efficiency with higher  $\alpha$ , the upper bound of  $M_{L,opt}$  with  $\alpha = 2$  is also the upper bound for the general case  $\alpha \geq 2$ .

#### 5.4.1 Equal Step-size Approximation

To guarantee the sustained spatial pipelining without packet loss, we need to focus on the worst-case scenario: the packet with index  $i$  in the middle sequence and  $x_{(i,k)} \approx L/2$  according to third observation in Section 5.2, and keep it alive. Also, if  $L$  is large enough, the co-channel OLAs have almost the equal step-size over the wide area around the mid-point of the network, which is shown in the fourth observation in Section 5.2. For this reason, we approximate the multi-packet OLA propagation patterns with the equal step-size to find the upper bound for  $M_{L,opt}$ . By assuming equal step-size, we neglect the “*edge effect*” in the finite network, or equivalently, we examine an  $L$ -long window of the infinite strip.

#### 5.4.2 Upper Bound of $M_{L,opt}$ with $\alpha = 2$

Under the equal step-size assumption, the condition for an infinite OLA propagation is the same as that for a single isolated packet (i.e.,  $\mu < 2$  as in Section 3.4), with unity noise

power replaced by noise-normalized interference power plus one:

$$\exp \left[ \frac{\tau(1 + \mathbf{I})}{\pi P_r} \right] < 2, \quad (31)$$

where  $\mathbf{I} = \sum_{j \neq 0} P(\tilde{\mathcal{O}}_{(i+j;k-jM)} \rightarrow x_{(i;k+1)})$  and the step-size of  $\tilde{\mathcal{O}}_{(i+j;k-jM)}$  is  $\Delta$ . A solution pair  $(M, \Delta)$  must satisfy (31) as well as the step-width condition:

$$\mathbf{SINR}_{(i;k+1)}(z) = \frac{P(\tilde{\mathcal{O}}_{(i;k)} \rightarrow z)}{\mathbf{I} + 1} = \tau, \quad (32)$$

where  $z = x_{(i;k+1)} = x_{(i;k)} + \Delta$  for all  $i$  and  $|x_{(i;k)} - x_{(j;k)}| = M\Delta|i - j|$  for all  $k$ . For given  $M$  and  $\Delta$ , the maximum number of packets pipelined in the network is  $n = \lceil \frac{L}{M\Delta} \rceil$ . Hence, for Packet  $i$  in the middle, the number of its preceding co-channel packets is  $n_p = \lceil \frac{n-1}{2} \rceil$ , while the number of its following packets is  $n_f = \lfloor \frac{n-1}{2} \rfloor$ . Therefore, when  $(n - 1)$  is odd,  $n_p = n_f + 1$ , which is because we consider the worst-case scenario and  $n_p = n_f + 1$  gives higher interference than  $n_f = n_p + 1$ , considering the propagation direction. Thus, with the number of co-channel packets  $n_p$  and  $n_f$ , we are able to test if the given  $\Delta$  and  $M$  satisfy (31) and (32). If  $\hat{M}_{L,opt}$  is the minimum  $M$  that satisfies these two conditions,  $\hat{M}_{L,opt} > M_{L,opt}$ .

### 5.4.3 Possible Multi-packet Transmission Strategy

We can consider a simple algorithm to find the optimal packet insertion period  $M_{L,opt}$  that maximizes the throughput by using  $\hat{M}_{L,opt}$  as the upper bound of  $M_{L,opt}$ , when the system parameters are known. To find  $M_{L,opt}$ , the source first needs to know the hop count  $M_0$  from the source to the destination, where the destination is located. Because the theoretical bound  $\hat{M}_{L,opt}$  in this section is obtained by assuming the free space path loss ( $\alpha = 2$ ),  $M_{L,opt} \leq \hat{M}_{L,opt}$  for  $\alpha > 2$ . Therefore, in general case with  $\alpha \geq 2$ , the search range of  $M_{L,opt}$  is  $3 \leq M \leq \min(M_0, \hat{M}_{L,opt})$ .

The end-to-end hop count  $M_0$  in the absence of the co-channel interference can be identified in the routing process. As stated in Section 2.1.2, the strip network models a cooperative route between a source and destination pair formed by on-demand routing protocols such as OLAROAD [13], OLACRA [5], and CBR [35]. These OLA-based

routing schemes require two end-to-end handshakes from the source to the destination as demonstrated in [13]: first handshake is to build a route using route request (RREQ) and route reply (RREP) and second handshake to check the route is valid using two additional control packets, route confirm (RC) and route confirm acknowledgement (RCACK). If RC, which is sent from the source to the destination in the second handshake, has the same data rate and packet length (by adding dummy bytes at the end of RC) as the data packet to have the same transmission ranges, RC will have the same hop-count characteristics as the data transmission in a static channel. Therefore, the destination can identify  $M_0$ , when it receives the RC originated from the source, because the RC has a hop count field incremented by one in each hop. After the destination receives the RC, it sends the RCACK, which contains the end-to-end hop count  $M_0$  information, back to the source. Therefore, when the source receives the RCACK, it can obtain  $M_0$  and use this information to limit the search scope of  $M_{L,opt}$ .

The search method of  $M_{L,opt}$  for  $3 \leq M \leq \min(M_0, \hat{M}_{L,opt})$  can be different (e.g., increasing, decreasing, or tree-based search) depending on the system requirements or applications. Regardless of the searching method, the packet loss before reaching the edge (i.e., destination) caused by  $M < M_{L,opt}$  can be detected in various ways. First, the error can be detected at the source through end-to-end error control in OLA-based unicasts. As suggested in [3] and [35], end-to-end error recovery, which is similar to the end-to-end error control in the Transmission Control Protocol (TCP), is more desirable in OLA-based unicasts compared to link-layer error control, because of random OLA levels and possible link asymmetry between two consecutive OLAs that have different numbers of cooperators [65]. Therefore, using the end-to-end feedback such as acknowledgement (ACK) signal sent from the destination using an orthogonal control channel, the source can detect the packet loss occurred with  $M < M_{L,opt}$ .

Alternatively, the packet loss can be found in intermediate OLAs by the virtual ACK as in [5], which is simply the OLA transmission that the current level OLA overhears from



the next level OLA in the next time slot (i.e., right after the transmission of the current level OLA). To be specific, in the multi-hop OLA transmission, Level  $k$  OLA forwards the packet received from Level  $(k - 1)$  OLA. Therefore, the nodes in Level  $(k - 1)$  OLA will detect an error (or packet loss) of their transmission to Level  $k$  OLA, if they cannot hear the data forwarding from Level  $k$  to Level  $(k + 1)$  for a fixed time duration in the following time slot, which implies Level  $k$  OLA fails to received the packet from Level  $(k - 1)$  OLA. If the packet loss is detected by Level  $(k - 1)$  OLA by this virtual ACK, the nodes in Level  $k$  OLA will send a feedback signal (i.e., negative acknowledgement (NACK)) to the source. Then, the source can detect the error and adapt the packet insertion period  $M$  to be longer. We note that the design of any link-level ACK or NACK scheme using OLAs is very challenging and outside the scope of this dissertation.

Once the optimal packet insertion period  $M_{L,opt}$  is found in a finite-length strip network with given system parameters such as  $\bar{P}_r$ ,  $\tau$ ,  $\alpha$ , we can expect how  $M_{L,opt}$  will change under the variation of a single parameter from the initial set-up based on the theoretical results in Section 5.3 and the numerical results in the next section. However, we note that more detailed protocol design to find  $M_{L,opt}$  and its evaluation are outside the scope of this dissertation.

## 5.5 Numerical Analysis of Optimal Throughput in the Finite Strip Network

In this section, we present three sets of numerical results for optimal throughput using spatially pipelined OLA transmission in the finite network. The optimal packet insertion period  $M_{L,opt}$  in the following results are obtained by exhaustive search, which corresponds to the optimal throughput  $\eta_{L,opt} = 1/M_{L,opt}$  for an infinite number of packets. We test a finite number of packets (but large enough to fill the network fully pipelined) for the numerical computation.

The following numerical results show the effects of different system parameters such as

$\bar{P}_r$ ,  $\tau$ , and  $\alpha$  on  $M_{L,opt}$ . However, as described in Section 4.3, because the distance between the packets or the OLA step-sizes can be an arbitrarily small positive number, the path loss function simply defined by  $l(d) = 1/d^\alpha$  does not hold for very small  $d$  [64]. Therefore, we use the path loss function in (22) as in Section 4.3

### 5.5.1 Impact of $P_s$ , $\bar{P}_r$ , and $\alpha$ on $M_{L,opt}$ with $\alpha = 2, 3$ , and 4

We first look at the effect of the transmit powers  $P_s$  and  $\bar{P}_r$  on the optimal packet insertion period  $M_{L,opt}$ , which is obtained by exhaustive search with given  $\alpha$ . By comparing the three cases with different  $\alpha$ , we will also consider the impact of  $\alpha$ . In the numerical results in Figure 24, we observe the variation in  $M_{L,opt}$ , which is indicated by the y-axis, when  $P_s$  and  $\bar{P}_r$ , which are indicated by the x-axis, increase from  $5 \times 10^4$  to  $10^5$  with  $10^4$  intervals. We use 50 packets with  $\tau = 10^3$  and  $W = 1$ . Moreover, to measure the degree of the throughput improvement by the ratio  $M_{L,opt}/M_0$ , we set the different lengths  $L = 1200$ , 215, and 121 for  $\alpha = 2, 3$ , and 4, respectively, to have the same final hop-count for the single-packet OLA transmission as  $M_0 = 50$  with the same  $P_s = \bar{P}_r = 5 \times 10^4$ . Therefore, the smaller  $M_{L,opt}$  means more efficient spatial pipelining compared to  $M_0 = 50$ , because the throughput increases as  $M$  decreases.

In the figure, the curve with the ‘x’-markers indicates the upper bound  $\hat{M}_{L,opt}$  derived in Section 5.4. Also, the solid line with no marker represents  $M_{L,opt}$  found by exhaustive search with  $\alpha = 2$ , while  $\alpha = 3$  and 4 cases are indicated by the curves with the square and triangle markers, respectively. If comparing the four curves at the same transmit powers  $P_s = \bar{P}_r$ ,  $\hat{M}_{L,opt} > M_{L,opt}$  always holds for all  $\alpha$ . Also, the higher path loss exponent  $\alpha$  gives lower  $M_{L,opt}$ , which means that we can expect more throughput improvement by spatial pipelining with higher  $\alpha$ , which is consistent with Corollary 1 in Section 5.3.

The upper bound  $\hat{M}_{L,opt}$  and the optimal  $M_{L,opt}$  with  $\alpha = 2$  show sharp decreases, as  $P_s$  and  $\bar{P}_r$  increase, because the increase in the signal power  $\mathbf{S}$  is relatively bigger than the increase in the interference  $\mathbf{I}$  by the physical distances. In other words, the increase in  $\bar{P}_r$  improves SIR at the desired receiver. Also, because  $\bar{P}_r$  increases, while  $\tau$  is fixed,

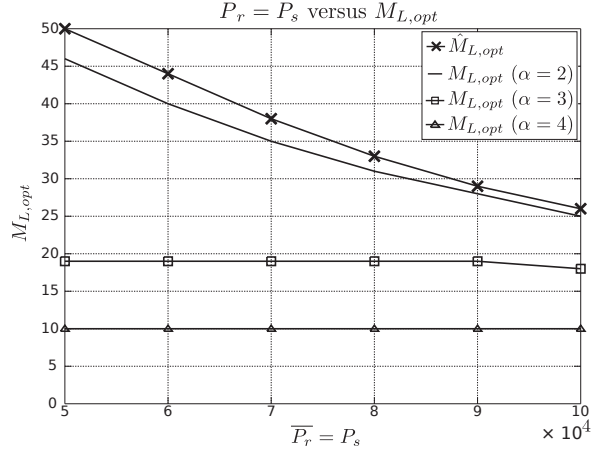


**Figure 24:** Numerical results with the increasing  $\bar{P}_r = P_s$ , when  $\tau = 10^3$ ,  $W = 1$  and  $L = 1200, 215, 121$  for  $\alpha = 2, 3, 4$ , respectively

**Table 3:** Average step-sizes of Packet 25 with different transmit powers

	$P_s = \bar{P}_r$					
$\alpha$	$5 \times 10^4$	$6 \times 10^4$	$7 \times 10^4$	$8 \times 10^4$	$9 \times 10^4$	$10 \times 10^4$
2	20.101	27.272	32.432	36.363	40.231	44.444
3	2.172	2.471	2.756	3.071	3.413	2.722
4	1.407	1.476	1.571	1.642	1.691	1.754

SINR increases, because noise becomes insignificant. For the same reasons, smaller  $M$  (i.e., shorter inter-packet spacing) can be accommodated. As a result,  $M_{L,opt}$  decreases, as the transmit powers increase. On the other hand, the optimal packet insertion periods  $M_{L,opt}$  with  $\alpha = 3$  and 4 are less sensitive to the transmit power change compared to  $\hat{M}_{L,opt}$  and  $M_{L,opt}$  with  $\alpha = 2$ . In the figure,  $M_{L,opt}$  with  $\alpha = 3$ , which is represented by the solid line with square markers, decreases only by one at  $P_s = \bar{P}_r = 10^5$ , while  $M_{L,opt}$  with  $\alpha = 4$ , which is indicated by the solid line with the triangle markers, does not change. That is simply because the impacts of the transmit powers on  $M_{L,opt}$  with higher exponents ( $\alpha = 2$  and 3) are not large enough, because of the high attenuation. In other words, the increases in  $P_s$  and  $\bar{P}_r$  should be more significant for the higher path loss exponent cases to reduce  $M_{L,opt}$  considerably.

Even though  $M_{L,opt}$  does not change much with  $\alpha = 3$  and 4, the increase of SINR can be noticed by the variation of the step-size. Table 3 shows the step-sizes, which are

averaged over all OLA levels, of the middle sequence packet (Packet 25) that experiences the lowest SINR as explained in Section 5.2.3. In the table, the three rows correspond to  $\alpha = 2, 3$ , and 4, while the columns indicate the six transmit power levels. As the transmit powers increase, the average step-sizes also increase for all cases except only when  $P_s = \bar{P}_r = 10^5$  and  $\alpha = 3$ . This exception is because  $M_{L,opt}$  decreases by one at the corresponding point. At this point, the improvement of SINR by increasing transmit powers is enough to accommodate the reduction of  $M_{L,opt}$  for  $\alpha = 3$ . On the other hand, for  $\alpha = 2$ , both the reduction of  $M_{L,opt}$  in Figure 24 and the growth of the step-size in Table 3 happen at the same time. That is because the significant step-size growth with  $\alpha = 2$  reduces the number of co-channel packets in the network significantly, which again inflates the SINR and the step-size. In contrast, the higher path loss exponents cases with  $\alpha = 3$  and 4 show relatively slower increases of step-size than  $\alpha = 2$ , which does not significantly reduce the number of co-channel packets in the network.

### 5.5.2 Impact of $\tau$ and $\alpha$ on $M_{L,opt}$ with $\alpha = 2, 3$ , and 4

The second set of numerical results in Figure 25 present the impact of the decoding threshold  $\tau$  on the optimal packet insertion period  $M_{L,opt}$  for different path loss exponents  $\alpha = 2, 3$ , and 4, with 50 packets,  $W = 1$ , and  $P_s = \bar{P}_r = 5000$ . As shown in the figure, the x-axis indicates the decoding threshold  $\tau = 25, 50, 75$ , and 100, while the y-axis represents  $M_{L,opt}$ . Also, the optimal packet insertion periods  $M_{L,opt}$  are found by exhaustive search with 50 packets, choosing different lengths  $L$  to keep the same final hop-count for the single-packet OLA transmission  $M_0 = 50$  for different  $\tau$ . Moreover, as in Figure 24, the graph with the ‘x’-markers indicates the upper bound  $\hat{M}_{L,opt}$ , while the other three graphs, which correspond to the different path loss exponents  $\alpha = 2, 3$ , and 4, are indicated by the solid lines with no markers, the square markers, and the triangle markers, respectively.

In the figure, all the four curves increase, as  $\tau$  increases, which means the optimal inter-packet spacing increases. This behavior is identical to Corollary 2 in Section 5.3. Also, when comparing the heights of the three curves indicating  $M_{L,opt}$  at the same  $\tau$ , a curve

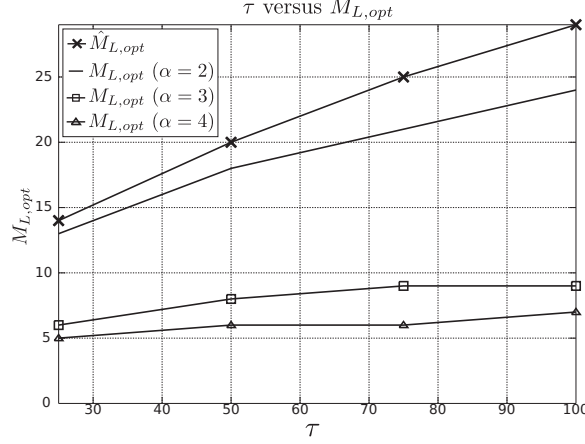


**Figure 25:** Numerical results with the increasing  $\tau = 25, 50, 75, 100$  for path loss exponents  $\alpha = 2, 3, 4$ , when  $P_s = \overline{P_r} = 5000$ ,  $M_0 = 50$ , and  $W = 1$

with the lower path loss exponent has the greater  $M_{L,opt}$  than the higher path loss exponent curve(s). Furthermore, among the three curves representing  $M_{L,opt}$ , the slopes of the  $\alpha = 2$  graph is the highest, compared to the curves with  $\alpha = 3$ , and 4, which means that the ‘ $\alpha = 2$ ’ case is the most sensitive to the increase in  $\tau$ . For  $\alpha = 3$  and 4, because the slopes of the two  $M_{L,opt}$  curves are close to zero, the corresponding throughputs  $1/M_{L,opt}$  slightly decrease. The decoding threshold  $\tau$  depends on other various parameters (e.g., modulation order, packet size, and coding scheme) that change the data rate with non-trivial relationships. In this study, we limit our scope to the packet-level analysis with the assumption that the parameters deciding  $\tau$  is fixed for a certain system.

Moreover, the graph corresponding to the upper bound  $\hat{M}_{L,opt}$  is always higher than the three other curves representing  $M_{L,opt}$  with  $\alpha = 2, 3$ , and 4, which implies that the upper bound is applicable for any  $\alpha \geq 2$ . Moreover, if comparing the heights of the three curves of  $M_{L,opt}$  corresponding to  $\alpha = 2, 3$ , and 4, at the same x values, we can find  $M_{L,opt}$  decreases as  $\alpha$  increases. In other words, as the path loss exponent  $\alpha$  increases, the throughput improvement by spatial pipelining becomes more significant, which confirms Corollary 1 in Section 5.3.

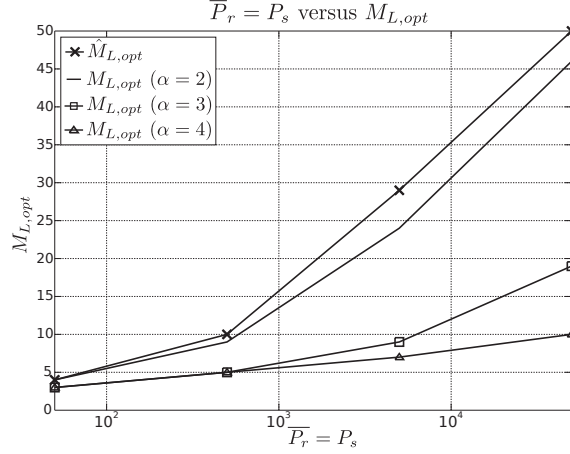


**Figure 26:** Numerical results for the same ratio of  $\frac{\bar{P}_r}{\tau}$ :  $(P_s, \bar{P}_r, \tau) = (50, 50, 1), (5 \times 10^2, 5 \times 10^2, 10), (5 \times 10^3, 5 \times 10^3, 10^2), (5 \times 10^4, 5 \times 10^4, 10^3)$ , when  $\alpha = 2, 3, 4$ ,  $M_0 = 50$ , and  $W = 1$

### 5.5.3 Impact of Simultaneous Variations in $\bar{P}_r$ and $\tau$ with Fixed Ratio for $\alpha = 2, 3$ , and 4

In the last set of numerical results, we explore the impact of simultaneous variations in  $\bar{P}_r$  and  $\tau$ , when the ratio of the two is fixed. Also, we explore the impact of  $\alpha$  by comparing the results with  $\alpha = 2, 3$ , and 4. Figure 26 shows how the optimal packet insertion period  $M_{L,opt}$  varies over different path loss exponents  $\alpha = 2, 3$ , and 4 with 50 packets,  $W = 1$ , and the fixed ratio of  $\frac{\bar{P}_r}{\tau} = 50$ . Based on (4),  $\kappa = 50\pi$ , when  $\alpha = 2$ , while  $\kappa$  is not defined in the continuum limit with  $\alpha > 2$  as discussed at the end of Section 3.4.2. We consider four different sets of parameters as  $(P_s, \bar{P}_r, \tau) = (50, 50, 1), (5 \times 10^2, 5 \times 10^2, 10), (5 \times 10^3, 5 \times 10^3, 10^2)$  and  $(5 \times 10^4, 5 \times 10^4, 10^3)$ , where  $\frac{\bar{P}_r}{\tau} = 50$ . Moreover, as in the previous numerical results, we set the different lengths  $L = 1200, 215$ , and 121 for  $\alpha = 2, 3$ , and 4, respectively, to see the throughput enhancement by the ratio  $M_{L,opt}/M_0$  for the same  $M_0 = 50$ , when the ratio  $\frac{\bar{P}_r}{\tau}$  is held constant.

In the resulting figure, Figure 26, the x-axis indicates  $P_s = \bar{P}_r$  in log scale, and the y-axis represents  $M_{L,opt}$  in linear scale with the same legend as in Figures 24 and 25. First, all the four curves increase, as the parameter sets move from the first:  $(50, 50, 1)$ , to the last:  $(5 \times 10^4, 5 \times 10^4, 10^3)$ . By increasing transmit powers  $P_s$  and  $\bar{P}_r$ , the received SINR increases as shown in the previous numerical results in Figure 24 and Table 3. Therefore,

with a fixed  $\tau$ , smaller inter-packet spacing would be possible as shown in the previous results. At the same time, however, by the increase of  $\tau$ , SINR requirement becomes more demanding, which exceeds the influence of the increase in  $\overline{P_r}$ . Thus, the simultaneous increases of transmit powers and  $\tau$ , while keeping the same ratio of the two, result in the increase of  $M_{L,opt}$ . Moreover, in the graph,  $M_{L,opt} \leq \hat{M}_{L,opt}$  always holds, which verifies the upper bound. As the previous results, the upper bound curve indicating  $\hat{M}_{L,opt}$  is always higher than  $M_{L,opt}$  for all  $\alpha = 2, 3$ , and  $4$ , which verifies the upper bound. Moreover, as the previous numerical results and Corollary 1 in Section 5.3, the optimal packet insertion period  $M_{L,opt}$  decreases, as  $\alpha$  increases.

## 5.6 Summary

In this chapter, we analyze the impact of the intra-flow interference in the multi-packet OLA transmission over the strip networks using the continuum and deterministic channel assumptions, which pertain to the high density networks. We present the signal model and the properties of the spatially pipelined OLA transmission in the strip-shaped network, where the length is significantly greater than the width. While the spatial pipelining always hurts the throughput in the disk networks with the free-space path loss  $\alpha = 2$ , in the strip networks it is feasible to improve the network throughput by spatial pipelining regardless of the path attenuation with  $\alpha \geq 2$ , which is proven by theoretical analysis. Moreover, we show the distinct propagation properties of the spatially pipelined OLA transmission, and use the properties to build a simplified multi-packet propagation model with a fixed step-size for the throughput optimization process that reduces the exhaustive search range. The numerical results show the impacts of the different system parameters on the optimal throughput in the finite network.

## CHAPTER 6

### VIRTUAL MULTIPLE-INPUT-SINGLE-OUTPUT (VMISO) LINK ANALYSIS OF CCT

We consider wireless networks with multiple centralized clusters using CT as shown in Figure 27, where the large circles with the dashed lines indicate clusters, the black-filled dots, which are labeled with A, B, and C, and the white-filled circles represent three cluster heads and cooperative relays, respectively. First, the intra-cluster cluster communication, which is indicated by the narrow black arrows, is required to recruit cooperating relays and form a virtual array. Then, the inter-cluster transmissions, which are indicated by the thick black arrows, are done in CT using the VMISO links. The CT through the VMISO links in multi-hop networks can have better reliability, higher throughput, and higher energy-efficiency compared to the conventional SISO networks [1, 2, 5, 11, 19, 35, 42, 43, 47, 66].

Assuming data transmissions from the left to right clusters, a VMISO communication on each cooperative hop consists of two phases as shown in Figure 28, where the source (or the transmit cluster head), which is labeled with ‘S,’ first transmits a packet to the destination (or the receive cluster head), which is labeled with ‘D’, in Phase 1. After that, the multiple relays, which are indicated by the white-filled circles around the source, decode and then forward (DF) using orthogonal channels or space-time codes to the destination in Phase 2 [41]. At the destination, the multiple copies from the source and multiple relays are combined, which provides an SNR advantage.

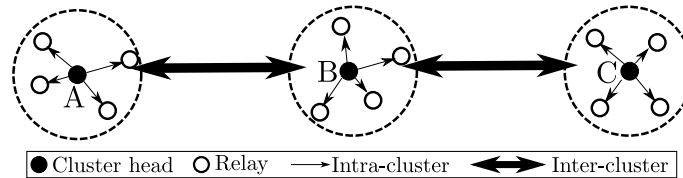


**Figure 27:** Logical illustration of a VMISO-based multi-hop network



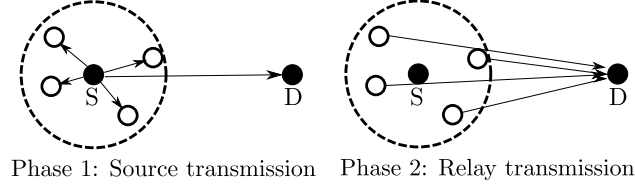


**Figure 28:** Two-hop cooperative transmission scenario for each cooperative hop

## 6.1 SNR Penalty from the Path-loss Disparity in a VMISO Link

### 6.1.1 System Model

We consider a static VMISO network as shown in Figure 35, where the source node is located at the origin with a distance  $d_0$  to the destination. Also, there are  $N$  number of cooperating relays around the source, which are located in the dotted-lined circle with a radius  $r_s$  centered at the source node. As in [1, 42, 43] that assume  $1.5 \leq d_0/r_s \leq 4$  by the CT range extension, depending on the number of relays and path loss exponent,  $r_s$  can be regarded as the SISO range, over which the source collects its cooperators. We note that the co-located VMISO model in [1, 42, 43] assumes that the link between the source and the relays are error-free, which is another factor that causes the error of the co-located approximation.

We assume that  $N$  relays are independently and identically distributed in the circle with the radius  $r_s$  following the uniform distribution. As shown in Figure 35, Relay  $k$  represented by the white-filled circle exists at a distance of  $r_k$  from the source with an angle  $\theta_k$  with respect to the line connecting the source and destination. Also, Relay  $k$  is  $d_k$  away from the destination, which determines the path loss between the relay and the destination. It follows that the polar coordinates  $(r_k, \theta_k)$  of Relay  $k$  have the probability distribution

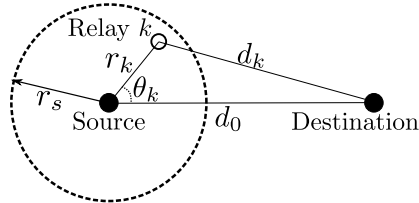


**Figure 29:** Network topology model

functions (PDFs) of  $f_{r_k}(r_k) = \frac{2r_k}{r_s^2}$  and  $f_{\theta_k}(\theta_k) = \frac{1}{2\pi}$ , where  $0 \leq r_k \leq r_s$  and  $0 \leq \theta_k \leq 2\pi$ , respectively.

#### 6.1.1.1 Channel Model

We assume mutually independent Rayleigh fading for any links between two nodes (the source, relays, and destination). The node indices of the source and destination are zero and  $N + 1$ . The complex channel gains are denoted by  $h_{0:k}$  (from the source to Relay  $k$ ),  $h_{0:N+1}$  (from the source to the destination), and  $h_{k:N+1}$  (from Relay  $k$  to the destination) with the relay node index  $1 \leq k \leq N$ . Hence,  $\Omega_{i:j} = |h_{i:j}|^2$  follows the exponential distribution with a parameter  $\lambda_{i:j}$  that is determined by the locations of Nodes  $i$  and  $j$ . Therefore, when the node locations are given, the cumulative distribution function (CDF) of  $\Omega_k$  given  $\lambda_{i:j}$  is expressed as  $F_{\Omega_{i:j}|\lambda_{i:j}}(x) = 1 - e^{-\lambda_{i:j}x}$ , where the conditional mean and variance are  $\mathbb{E}\{\Omega_{i:j}|\lambda_{i:j}\} = 1/\lambda_{i:j}$  and  $\mathbb{V}\text{AR}\{\Omega_{i:j}|\lambda_{i:j}\} = 1/\lambda_{i:j}^2$ , respectively. If the path loss exponent is  $\alpha$ , then  $\lambda_{0:k} = r_k^\alpha$  for the source-relay link and  $\lambda_{k:N+1} = d_k^\alpha$  for the relay-destination link.

#### 6.1.1.2 Outage Model

In this section, we first consider the outage probability for a deterministic network topology (i.e., the relay locations are given), the closed form of which is provided in [41]. However, while [40, 41] and other existing physical layer studies in CT assume a specific network topology, which is not random, we consider the random spatial distribution of the relays to capture the effect of the path-loss disparity.

Assuming the same transmission powers for the source and  $N$  relays, the conditional mutual information between the source and Relay  $k$  given that  $\lambda_{0:k} = r_k^\alpha$  is  $\mathbf{I}_{0:k}(\text{SNR}|\lambda_{0:k}) = \frac{1}{N+1} \log_2(1 + \text{SNR} \cdot \Omega_{0:k})$ , where SNR is the transmit SNR of each node [41]. Therefore, for a certain transmission rate  $R$  (bit/Hz/sec), the probability that Relay  $k$  fails to decode the received signal from the source is given by

$$p_k = F_{\Omega_{0:k}|\lambda_{0:k}}(g(\text{SNR}, R)) = 1 - e^{-\lambda_{0:k} \cdot g(\text{SNR}, R)}, \quad (33)$$

where  $F_{\Omega_{0:k}|\lambda_{0:k}}(x)$  is the conditional CDF of  $\Omega_{0:k}$  given  $\lambda_{0:k} = r_k^\alpha$ , and  $g(t, R) = (2^{(N+1)R} - 1)/t$ .

Suppose that for a given network topology,  $\mathcal{S}$  is a particular set of  $M$  relays that successfully decode the source transmission, where  $0 \leq M \leq N$ . Therefore, the conditional mutual information of the VMISO link, conditioned on  $\mathcal{S}$ , is given by  $\mathbf{I}(\text{SNR}|\mathcal{S}) = \frac{1}{N+1} \log_2(1 + \text{SNR} \cdot \Omega_{0:N+1} + \sum_{k \in \mathcal{S}} \text{SNR} \cdot \Omega_{k:N+1})$ .

Thus, the outage probability of the VMISO communication for a given network topology indicated by two parameter vectors  $\bar{\Lambda}_s = [\lambda_{0:1}, \lambda_{0:2}, \dots, \lambda_{0:N}]^T$  and  $\bar{\Lambda}_d = [\lambda_{1:N+1}, \lambda_{2:N+1}, \dots, \lambda_{N:N+1}]^T$  that satisfy  $\lambda_{0:k} = r_k^\alpha$  and  $\lambda_{k:N+1} = d_k^\alpha$  with  $1 \leq k \leq N$  is expressed as  $P_{out|\bar{\Lambda}_s, \bar{\Lambda}_d} = \sum_{\mathcal{S}} \Pr[\mathbf{I} < R|\mathcal{S}] \cdot \Pr[\mathcal{S}]$ , where  $\Pr[\mathcal{S}] = (\prod_{k \notin \mathcal{S}} p_k) \cdot (\prod_{k \in \mathcal{S}} (1 - p_k))$ . This equation is the same as in [41] except that we suppose  $\Pr[\mathcal{S}]$  is the probability conditioned on the certain network topology (i.e.,  $\bar{\Lambda}_s$  and  $\bar{\Lambda}_d$ ). Considering the randomness of the relay locations, the outage rate averaged over the random network topology has  $N^2$ -fold integral as

$$P_{out} = \int \dots \int P_{out|\bar{\Lambda}_s, \bar{\Lambda}_d} \cdot \prod_{k=1}^N [f_{\lambda_{0:k}, \lambda_{k:N+1}}(\lambda_{0:k}, \lambda_{k:N+1}) d\lambda_{0:k} d\lambda_{k:N+1}], \quad (34)$$

where  $f_{\lambda_{0:k}, \lambda_{k:N+1}}(x_1, x_2)$  is the joint PDF of  $\lambda_{0:k}$  and  $\lambda_{k:N+1}$ , which can be obtained by the variable transformation from  $f_{r_k}(r_k)$  and  $f_{\theta_k}(\theta_k)$ .

## 6.1.2 Outage Rate Approximation

### 6.1.2.1 First-hop Error Approximation

It is hard to obtain the closed form expression of the outage probability under the random relay locations in (34), because the first-hop (between the source and the relays) and second-hop (between the relays to the destination) depend on each other by the random relay locations. Therefore, to focus on the impact of the path-loss disparity in the second-hop, we approximate the first-hop error rates of the  $N$  relays by independent Bernoulli trials. The first-hop outage rate of Relay  $k$  in (33) satisfies that  $0 \leq p_k \leq p_{max} = 1 - e^{-r_s^\alpha \cdot g(\text{SNR}, R)}$ , because  $0 \leq r_k \leq r_s$ . If all  $N$  relays have the same constant first-hop error rate of  $p$ , where  $0 \leq p \leq p_{max}$ ,  $P_{out|\bar{\Lambda}_s, \bar{\Lambda}_d}$  in Section 6.1.1.2, which does not depend on  $\bar{\Lambda}_s$  anymore, is simplified as

$$P_{out|\bar{\Lambda}_d} = \sum_{M=0}^N \binom{N}{M} p^{N-M} (1-p)^M \Pr \left[ \sum_{k=0}^M \Omega_{k:N+1} < g(\text{SNR}, R) \right]. \quad (35)$$

If  $Y = \sum_{k=0}^M \Omega_{k:N+1}$ , then  $\Pr \left[ \sum_{k=0}^M \Omega_{k:N+1} < g(\text{SNR}, \mathbf{R}) \right] = F_{Y|M, \bar{\Lambda}_{d(1:M)}}(g(\text{SNR}, \mathbf{R}))$  that is the conditional CDF of  $Y$  for given  $M$  and a truncated vector with  $M$  elements out of  $N$ ,  $\bar{\Lambda}_{d(1:M)} = [\lambda_{1:N+1}, \dots, \lambda_{M:N+1}]^T$ . Therefore, the final outage in (34) is approximated with  $N$ -fold integral by

$$\begin{aligned} \tilde{P}_{out} = & \sum_{M=0}^N \binom{N}{M} p^{N-M} (1-p)^M \int \dots \int F_{Y|M, \bar{\Lambda}_{d(1:M)}}(g(\text{SNR}, \mathbf{R})) \\ & \times f_{\lambda_{1:N+1}}(\lambda_{1:N+1}) \dots f_{\lambda_{N:N+1}}(\lambda_{N:N+1}) d\lambda_{1:N+1} \dots d\lambda_{N:N+1}, \end{aligned} \quad (36)$$

As a general case, when  $\lambda_{k:N+1} \neq \lambda_{j:N+1}$  for  $k \neq j$ ,  $F_{Y|M, \bar{\Lambda}_{d(1:M)}}(y)$  follows the hypoexponential distribution [67] as

$$F_{Y|M, \bar{\Lambda}_{d(1:M)}}(y) = 1 - \sum_{k=0}^M A_k \exp(-\lambda_k y), \quad (37)$$

where  $A_k = \prod_{j \neq k} \frac{\lambda_j}{\lambda_j - \lambda_k}$  and  $\sum_{k=0}^M A_k = 1$ . On the other hand, when  $\lambda_{0:N+1} = \lambda_{1:N+1} = \dots = \lambda_{M:N+1} = \lambda$ , which corresponds to the co-located antenna array with  $M$  elements,  $F_{Y|M, \bar{\Lambda}_{d(1:M)}}(y)$  is the CDF of the gamma distribution as

$$F_{Y|M, \lambda}(y) = 1 - \sum_{k=0}^M \frac{\exp(-\lambda y) \cdot (\lambda y)^k}{k!}. \quad (38)$$

Therefore, as shown in the equation,  $F_{Y|M, \bar{\Lambda}_{d(1:M)}}(y)$  can be simplified into  $F_{Y|M, \lambda}(y)$  with the single condition variable  $\lambda$  instead of the condition vector  $\bar{\Lambda}_{d(1:M)}$ . Also, the outage probability in (36) can be expressed with a single integral as

$$\tilde{P}_{out} = \sum_{M=0}^N \binom{N}{M} p^{N-M} (1-p)^M \int F_{Y|M, \lambda}(g(\text{SNR}, \mathbf{R})) f_{\lambda|M}(\lambda) d\lambda. \quad (39)$$

We note that, for the co-located approximation,  $P_{out} = F_{Y|M=N, \lambda=d_0^{\alpha}}(g(\text{SNR}, \mathbf{R}))$  without any integral, because all the links have the same distances of  $d_0$  to the destination. Compared to (36), the outage equation in (39) is much simpler, because there is only one integral. Also, the conditional CDF  $F_{Y|M, \bar{\Lambda}_{d(1:M)}}(y)$  in (37) is numerically sensitive to compute [40]. Therefore, ultimately to capture the impact of path-loss disparity, we use an approximation to project the vector  $\bar{\Lambda}_{d(1:M)} = [\lambda_{1:N+1}, \dots, \lambda_{M:N+1}]^T$  into a single variable  $\lambda$  assuming high SNR, while keeping the influence of the random relay locations on the outage rate, in the following section.

### 6.1.2.2 Gamma Approximation of $F_{Y|M, \bar{\Lambda}_{d(1:M)}}(y)$ into $F_{Y|M, \lambda}(y)$

Many studies on CT focus on the asymptotic performance by the limit of  $\text{SNR} \rightarrow \infty$  [40]. In [40], the author proposes a simple but accurate way to calculate outage performance of CT with dissimilar path losses, where the outage probability based on hypoexponential distribution in (37) can be approximated by the outage probability computation using gamma distribution in (38) with a negligible error. This enables us to use the traditional notion of the performance analysis based on the real multiple-antenna array system to the VMISO link. The key result in this approximation is

$$\lambda = \left( \prod_{k=0}^M \lambda_{k:N+1} \right)^{1/(M+1)}. \quad (40)$$

In other words, in this gamma approximation, the single parameter  $\lambda$  is equal to the geometric average of the distinct  $\lambda_{k:N+1}$  for  $k = 0, 1, \dots, M$ .

### 6.1.2.3 Log-normal Approximation of $f_{\lambda|M}(x)$

To calculate the outage rate with the random relay locations in (39) with the gamma approximation, we need to obtain the conditional PDF of  $\lambda$  for given  $M$ . In dB, (40) is expressed as

$$10 \log_{10} \lambda = \frac{10}{M+1} \sum_{k=0}^M \log_{10} \lambda_{k:N+1}, \quad (41)$$

where  $\lambda_{0:N+1} = d_0^\alpha$  is deterministic, while  $\lambda_{1:N+1}, \dots, \lambda_{M:N+1}$  are i.i.d. random variables, when  $d_0, r_s$ , and  $\alpha$  are given. Therefore, when  $M$  is large enough, by the Central Limit Theorem (CLT) [67],  $f_{\lambda|M}(x)$  in (39) is approximated into a log-normal distribution as

$$f_{\lambda|M}(x) \approx \frac{1}{x^\xi \sqrt{2\pi}\sigma} \exp \left[ -\frac{(10 \log_{10} x - \mu)^2}{2\sigma^2} \right], \quad (42)$$

where  $0 < x < \infty$ ,  $\xi = \ln 10/10$ . Also, because  $\lambda_{k:N+1} = 1/d_k^\alpha$ ,  $\mu = \mathbb{E}\{\lambda|M\} = \frac{10\alpha}{M+1}(\log_{10} d_0 + M \mathbb{E}\{\log_{10} d_k\})$  and  $\sigma^2 = \text{VAR}\{\lambda|M\} = \frac{100\alpha^2 M}{(M+1)^2} \text{VAR}\{\log_{10} d_k\}$ .

Therefore, the influence of the random relay locations can be characterized by the log-normal approximation of the PDF of  $\lambda$ , which means that the random separations have the same effect as *log-normal shadowing* on the outage. Using this approximation, the outage

probability  $\widetilde{P}_{out}$  in (39) can be simplified in a summation form using the Gauss-Hermite method [68]:

$$\widetilde{P}_{out} \approx \sum_{M=0}^N \binom{N}{M} \frac{p^{N-M}(1-p)^M}{\sqrt{\pi}} \left[ \sum_{i=1}^m W_i \cdot G\left(10^{\frac{\sqrt{2}\sigma r_i + \mu}{10}}\right) \right]. \quad (43)$$

where  $G(x) = F_{Y|M,\lambda=x}(g(\text{SNR}, R))$ ,  $W_i$  are weight factors,  $r_i$  are the roots of the Hermite polynomial, and  $m$  is the order of the Hermite polynomial. However, the outage probability is determined by the tail property of the channel distribution, and the log-normal approximation has a longer tail than the original conditional PDF  $f_{\lambda|M}(x)$ , especially when  $M$  is small. Therefore, this outage rate based on the log-normal approximation is higher than (39), which is used to derive the upper bound of the outage rate in the following section.

### 6.1.3 Upper and Lower Bounds of Outage Rate

To calculate the approximated outage probability in the previous section, which serves as an upper bound of the real outage capacity,  $\mathbb{E}\{\log_{10} d_k\}$  and  $\mathbb{V}\text{AR}\{\log_{10} d_k\}$  need to be obtained for  $\mu$  and  $\sigma^2$  in (43). However, the PDF of  $d_k$ ,  $f_{d_k}(x)$ , which characterizes the distance from Relay  $k$  to the destination, does not give closed form expressions of its mean and variance. Therefore, in this section, we approximate  $f_{d_k}(x)$  and derive the corresponding  $\mu$  and  $\sigma^2$  in closed forms. Moreover, we also propose upper and lower bounds of the real  $P_{out}$  in (34).

#### 6.1.3.1 Upper Bound $P_{out:U}$

By variable transformation, the original PDF of  $d_k$ ,  $f_{d_k}(x)$  is given by

$$f_{d_k}(x) = \frac{x}{\pi r_s^2} \left( \frac{\frac{r_s}{d_0} - \frac{(d_0^2 - x^2 + r_s^2)}{2d_0 r_s}}{\sqrt{1 - \frac{(d_0^2 - x^2 + r_s^2)^2}{4d_0^2 r_s^2}}} - \frac{\left(\frac{x}{d_0} - \frac{d_0^2 + x^2 - r_s^2}{2d_0 x}\right)}{\sqrt{1 - \frac{(d_0^2 + x^2 - r_s^2)^2}{4d_0^2 x^2}}} + 2 \arccos\left(\frac{d_0^2 + x^2 - r_s^2}{2d_0 x}\right) \right), \quad (44)$$

where  $d_0 - r_s \leq x \leq d_0 + r_s$ . When  $d_0$  is large enough compared to  $r_s$  in Figure 35, the original PDF of  $d_k$ ,  $f_{d_k}(x)$  can be simplified into  $f_{d_k}^*(x) = \frac{2}{\pi r_s^2} \sqrt{r_s^2 - (d_0 - x)^2}$ , where  $d_0 - r_s \leq x \leq d_0 + r_s$ . As an example, in Figure 30, when  $d_0 = 4$  and  $r_s = 1$ ,  $f_{d_k}^*(x)$  is indicated by the black dotted line, while the original PDF  $f_{d_k}(x)$  is represented by the black solid line. As shown in the figure,  $f_{d_k}^*(x) \approx f_{d_k}(x)$  in the domain  $d_0 - r_s \leq x \leq d_0 + r_s$ , which confirms the validity of  $f_{d_k}^*(x)$ . Moreover, this approximated PDF  $f_{d_k}^*(x)$  has the mean and

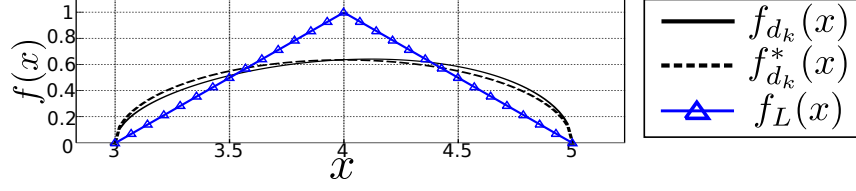


**Figure 30:** PDF of  $d_k$  and its approximations, when  $r_s = 1$  and  $d_0 = 4$

variance in closed forms as  $\mathbb{E}\{d_k\} = d_0$  and  $\text{VAR}\{d_k\} = r_s^2/4$ . Therefore, by the Taylor expansion,  $\mathbb{E}\{\log_{10} d_k\} \approx \log_{10} d_0$  and  $\text{VAR}\{\log_{10} d_k\} \approx \frac{r_s^2}{4(d_0 \ln 10)^2}$ . Therefore, we can obtain  $\mu$  and  $\sigma^2$  as

$$\mu = 10\alpha \log_{10} d_0, \quad (45)$$

$$\sigma^2 = \frac{25M}{(M+1)^2} \left( \frac{\alpha r_s}{d_0 \ln 10} \right)^2. \quad (46)$$

By plugging these two parameters with the worst case first-hop probability  $p = p_{\max} = 1 - e^{-r_s^\alpha \cdot g(\text{SNR}, R)}$  into (43), the upper bound  $P_{\text{out};U}$  of the real  $P_{\text{out}}$  in (34) can be obtained.

#### 6.1.3.2 Lower Bound $P_{\text{out};L}$

To derive a lower bound of the outage probability, we propose a new PDF  $f_L(x)$  that is intentionally designed to obtain a smaller variance  $\sigma_L^2$  than  $\sigma^2$  in (46) to shrink the tail probability of the log-normal approximation in (43). The new PDF  $f_L(x)$ , which is triangle-shaped and symmetric to  $x = d_0$  as indicated by the blue line with the triangle markers in Figure 30, is given by

$$f_L(x) = \begin{cases} \frac{x+r_s-d_0}{r_s^2}, & d_0 - r_s \leq x < d_0, \\ \frac{-x+r_s+d_0}{r_s^2}, & d_0 \leq x < d_0 + r_s, \end{cases} \quad (47)$$

which gives  $\mathbb{E}\{L\} = d_0$  that is same to  $\mathbb{E}\{d_k\}$  and  $\text{VAR}\{L\} = r_s^2/6$  that is smaller than  $\text{VAR}\{d_k\}$ . Thus, using this PDF  $f_L(x)$  and the Taylor expansion, the corresponding  $\mu$  is same to (45), while the reduced version of  $\sigma^2$  in (46) is given by  $\sigma_L^2 = 2\sigma^2/3$ . Therefore, if applying  $\sigma^2 = \sigma_L^2$  with the error-free first-hop condition  $p = 0$ , which always makes  $M = N$ , in (43), the lower bound of the real outage probability denoted by  $P_{\text{out};L}$  can be obtained.

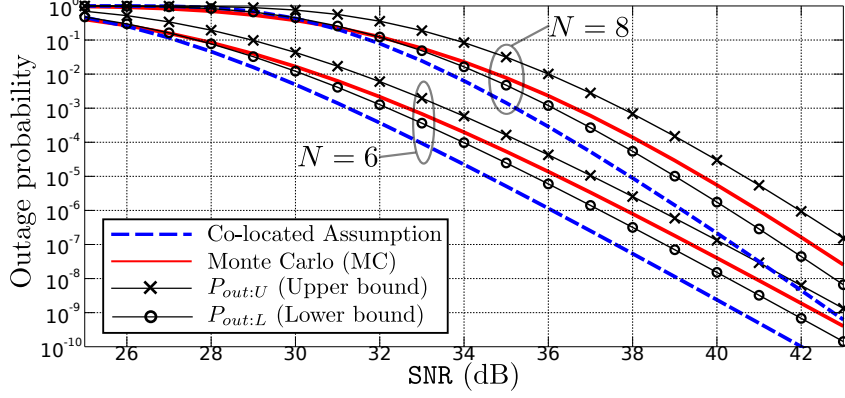


**Figure 31:** Outage curves, when  $R = 1$ ,  $d_0 = 2$ ,  $r_s = 1$ ,  $\alpha = 4$ , and  $N = 6, 8$

### 6.1.4 Simulation Results and Discussion

#### 6.1.4.1 Outage Probability

Figure 31 shows the outage simulation results with  $R = 1$ ,  $d_0 = 2$ ,  $r_s = 1$ , and  $\alpha = 4$ . In the figures, the horizontal axis is SNR in dB, while the vertical axis indicates the outage probability. There are two groups of the curves: the group having the higher outage rates with the steeper slopes corresponds to  $N = 8$ , while the lower group indicates  $N = 6$ . The blue dashed lines represent the outage rates based on the co-located assumption that ignores the path-loss disparity and first-hop errors. Also, the red solid curves are the true outage probabilities obtained by the Monte Carlo simulation (MC), while the solid lines with the ‘x’- and ‘o’-markers indicate the upper and lower bounds, respectively. Therefore, the gaps between the blue dashed lines and the red solid lines are the errors caused by the co-located assumption. For example, when the target outage rate is  $10^{-6}$ , the errors are about 1.75 and 1.8dB for  $N = 6$  and 8, respectively. In other words, to achieve the outage probability of  $10^{-6}$  considering the relay separations and the source-relay link errors, it requires more transmission power (e.g., 1.75 and 1.8dB for  $N = 6$  and 8, respectively) than the transmit power calculated by the co-located approximation.

Moreover, in the both groups, the real outage curves are always in between  $P_{out:U}$  and  $P_{out:L}$  in the high SNR regime (when the outage is less than  $10^{-4}$ ), which verifies the two bounds. Therefore, the SNR penalty of the co-located assumption (i.e., the error in terms



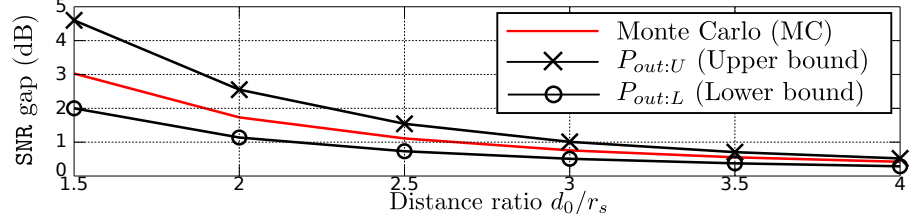
of SNR to achieve the target outage rate) can be estimated by the two bounds that characterize the impact of the path-loss disparity by the equivalent log-normal shadowing model, following the conventional notion of the composite channel.

#### 6.1.4.2 SNR Penalty depending on System Parameters

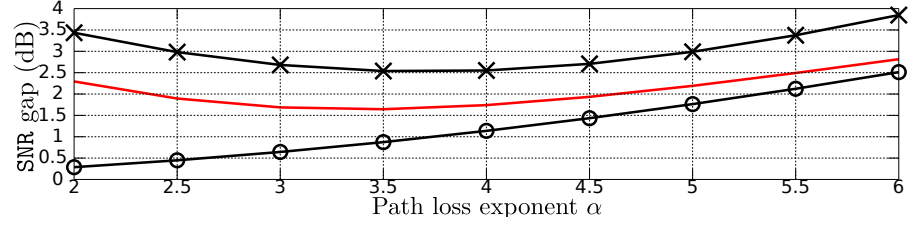
In this section, we look at the error of the co-located assumption in terms of the SNR penalty or gap to achieve the outage probability of  $10^{-6}$  depending on three system parameters: the distance ratio  $d_0/r_s$ , the path loss exponent  $\alpha$ , and the number of relays  $N$ . In the simulation results shown in Figures 39, 33, and 34, there are three SNR gaps to the co-located assumption: the real error based on MC (the red solid lines), and the estimated errors by the upper and lower bounds (the black curves with the 'x'- and 'o'-markers, respectively). In the three figures, the real error is always in between the errors measured by the two bounds.

Figure 39 shows the SNR penalty in dB indicated by the y-axis for the different distance ratio  $d_0/r_s$  represented by the x-axis, when  $r_s = 1$ ,  $\alpha = 4$  and  $N = 6$ . All the three SNR gaps decrease as  $d_0/r_s$  increases, because the impact of the path-loss disparity becomes negligible for high  $d_0/r_s$ , which is also noticed by that the two variances  $\sigma^2$  and  $\sigma_l^2$  of the equivalent log-normal shadowing model are decreasing functions of  $d_0/r_s$ . Also, the first-hop error ignored in the co-located assumption is relatively much smaller than the second-hop error, when  $d_0/r_s$  is large. However, considering that  $d_0/r_s=1.5$  and 2 are the CT range extension ratios widely assumed in the VMISO-based protocol studies, the corresponding errors are large enough to degrade the protocols designed and operated with the co-located assumption.

Figure 33 displays the impact of the path loss exponent  $\alpha$  on the SNR penalty, when  $r_s = 1$ ,  $d_0 = 2$ , and  $N = 6$ . The SNR gaps based on the MC and the upper bound have the convex curves that have the minimum heights at around  $\alpha = 3.5$ , while the lower bound is monotonically increasing. The height decreases of the MC and the upper bounds for  $2 \leq \alpha \leq 3.5$  are because the first-hop error relative to the second-hop error increases as  $\alpha$



**Figure 32:**  $d_0/r_s$  versus SNR gaps, when  $r_s = 1$ ,  $\alpha = 4$ , and  $N = 6$



**Figure 33:**  $\alpha$  versus SNR gaps, when  $r_s = 1$ ,  $d_0 = 2$ , and  $N = 6$

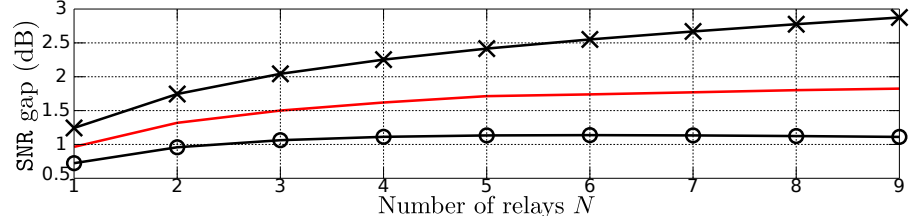


**Figure 34:**  $N$  versus SNR gaps, when  $r_s = 1$ ,  $d_0 = 2$ , and  $\alpha = 4$

decreases for a fixed  $d_0/r_s$ , which means that the first-hop error cannot be ignored in this range. The reason that the lower bound simply increases in this range is also the error-free first-hop assumption. On the other hand, when  $3.5 \leq \alpha \leq 6$ , all the three curves increases, as  $\alpha$  increases, because the path-loss disparity within the VMISO cluster becomes significant ( $\sigma^2$  and  $\sigma_l^2$  are increasing functions of  $\alpha$ ).

In the last figure, Fig 34, the three graphs increase, while the slopes become less steep, as  $N$  increases. This pattern can be explained by the equivalent shadowing model: the path-loss disparity can be characterized the same (fully-correlated) shadowing outcomes overlaid on the independent Rayleigh fading channels of  $N$  antennas in the real MISO link. Thus, by the path-loss disparity, the VMISO link loses a certain degree of the diversity gain because of the increased channel correlation compared to the full diversity in the co-located assumption simply over independent Rayleigh fading. Therefore, the SNR penalty to the

co-located assumption increases, as  $N$  increases, if the degree (variance) of the equivalent shadowing is fixed. However, the variances used in the two bounds ( $\sigma^2$  and  $\sigma_l^2$ ) decrease, when  $N=M$  (assuming the error-free first-hop) increases. Thus, the slopes of the graphs become less steep, as  $N$  increases. Moreover, the MC and the upper bound always have higher slope than the lower bound, because of the diversity gain losses in the MC and the upper bounds are more significant by the first-hop error.

## 6.2 Link Asymmetry in VMISO-based Networks

### 6.2.1 System Model

In this section, we consider both forward and reverse VMISO links as shown in Figure 35, while we only focus on the forward VMISO link from the source to the destination. Therefore, we extend the system model in Section 6.1.1 to deal with the both two-way VMISO links. As in the path loss disparity analysis system model, the distance between the source and destination, which are labeled with 'S' and 'D', respectively, is  $d_0$ . Also, we assume cooperating relays are uniformly and randomly distributed around the cluster heads (source and destination), in the area of the dashed-line circles with a radius  $r_s$  centered at the cluster heads.

We assume that  $M$  relays in the source cluster and  $N$  relays in the destination cluster are independently and identically distributed in the two circles with the radius  $r_s$  following the uniform distribution. As shown in Figure 35, Relay  $i$  and Relay  $j$  in the source and destination clusters, represented by the white-filled circles, exist at distances of  $r_{F:i}$  and  $r_{R:j}$  from their cluster heads (source and destination) with angles of  $\theta_{F:i}$  and  $\theta_{R:j}$  with respect to

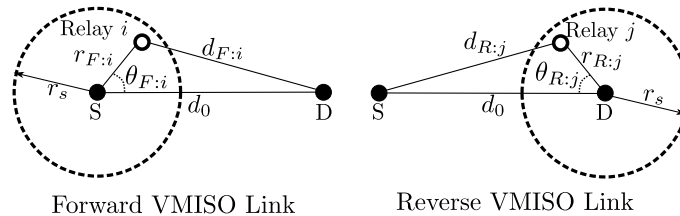


**Figure 35:** Network topology model

the line connecting the source and destination, respectively. Also, Relays  $i$  and  $j$  are  $d_{F:i}$  and  $d_{R:j}$  away from the other cluster heads respectively, which determines the path losses from the relays to the other cluster heads. It follows that the polar coordinates  $(r_{v:w}, \theta_{v:w})$  centered at each cluster head, where  $v \in \{F, R\}$  and  $w = 1, \dots, N$  for  $v = F$  or  $w = 1, \dots, M$  for  $v = R$ , have the probability distribution functions (PDFs):  $f_{r_{v:w}}(r_{v:w}) = \frac{2r_{v:w}}{r_s^2}$  and  $f_{\theta_{v:w}}(\theta_{v:w}) = \frac{1}{2\pi}$ , where  $0 < r_{v:w} \leq r_s$  and  $0 \leq \theta_{v:w} \leq 2\pi$ , respectively.

#### 6.2.1.1 Channel Model

As in Section 6.1.1, we assume mutually independent Rayleigh fading for any links between two nodes in different clusters. The node indices of the two cluster heads (the source and destination) are zero, while the relays have indices  $1 \leq i \leq M$  and  $1 \leq j \leq N$  for the source and destination clusters, respectively. The complex channel gains of the forward links are denoted by  $h_{i,j}$ , while the reverse channel gains are denoted by  $g_{j,i}$ , where  $i = 0, \dots, M$  and  $j = 0, \dots, N$  including the communication channels involving the cluster heads. However, we note that only the cluster head in each cluster decodes the signals received from the other cluster in a VMISO network, which means that we only need to consider the channel gains  $h_{i,0}$  and  $g_{j,0}$  for  $i = 0, \dots, M$  and  $j = 0, \dots, N$ . For simplicity, we assume unit transmit power for all the nodes. Hence,  $\Omega_{F:i} = |h_{i,0}|^2$  and  $\Omega_{R:j} = |g_{j,0}|^2$  follow the exponential distribution with a parameter  $\lambda_{F:i} = d_{F:i}^\alpha$  or  $\lambda_{R:j} = d_{R:j}^\alpha$ , which is determined by the locations of Nodes  $i$  and  $j$ , with the path loss exponent  $\alpha$ . The cumulative distribution functions (CDF) of  $\Omega_{v:w}$  given  $\lambda_{v:w}$  is expressed as

$$F_{\Omega_{v:w}|\lambda_{v:w}}(x) = 1 - e^{-\lambda_{v:w}x}, \quad (48)$$

where  $v \in \{F, R\}$  and  $w = 1, \dots, N$  for  $v = F$  or  $w = 1, \dots, M$  for  $v = R$ . Also, the conditional mean and variance for given  $\lambda_{v:w}$  are  $\mathbb{E}\{\Omega_{v:w}|\lambda_{v:w}\} = 1/\lambda_{v:w}$  and  $\text{VAR}\{\Omega_{v:w}|\lambda_{v:w}\} = 1/\lambda_{v:w}^2$ , respectively.

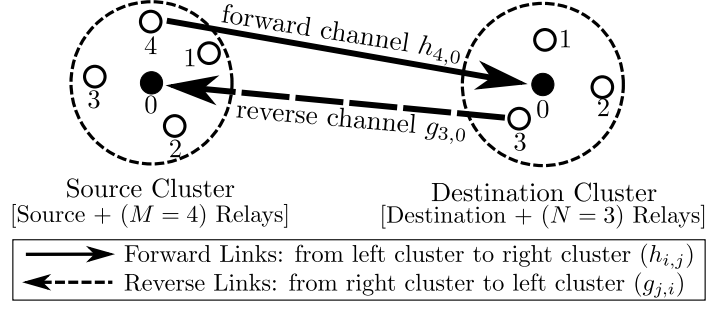


**Figure 36:** Illustration of forward and reverse links

## 6.2.2 Correlation of Forward and Reverse Links

### 6.2.2.1 Signal Reception Only at the Cluster Head

Without cooperative reception, the centralized CT networks use a single VMISO link in one direction for each hop, because only the receive cluster head decodes, while the cooperative relays are used only for transmission. For a real or virtual MIMO link with  $(M+1)$  transmit antennas and  $(N+1)$  receive antennas, the forward channel gain can be expressed by a  $(M+1) \times (N+1)$  channel matrix  $\mathbf{H}$  that has elements  $h_{i,j}$  denoting the channel gain from transmit antenna  $i$  to receive antenna  $j$ . Moreover, the reverse channel matrix  $\mathbf{G}$ , the dimension of which is  $(N+1) \times (M+1)$ , has elements  $g_{j,i}$  that denotes the reverse channel gain from antenna  $j$  to  $i$ . Assuming frequency nonselective block fading, by the reciprocity stated in [53], we can assume  $\mathbf{H} = \mathbf{G}^T$ , where  $\mathbf{T}$  is the matrix transpose. However, a VMISO link uses only a part of the channel matrices  $\mathbf{H}$  and  $\mathbf{G}$ . For example, the forward link channel gains  $h_{i,0}$ , where  $i = 1, \dots, M$ , are one row of the matrix  $\mathbf{H}$ . Similarly, the reverse link channel gains  $g_{j,0}$ , where  $j = 1, \dots, N$ , are one row of the matrix  $\mathbf{G}$ . Therefore, in general, a VMISO hop has only one common channel gain between the forward and reverse links  $h_{0,0} = g_{0,0}$ . Assuming unit transmit power for simplicity with maximal ratio combining (MRC), the total received powers at the cluster heads through the forward and reverse links can be represented as  $P_F = \sum_{i=0}^M \Omega_{F:i}$  and  $P_R = \sum_{j=0}^N \Omega_{R:j}$ , where  $\Omega_{F:i} = |h_{i,0}|^2$  and  $\Omega_{R:i} = |g_{j,0}|^2$ . Because  $\Omega_{F:0} = |h_{0,0}|^2 = \Omega_{R:0} = |g_{0,0}|^2$ , the correlation coefficient between the

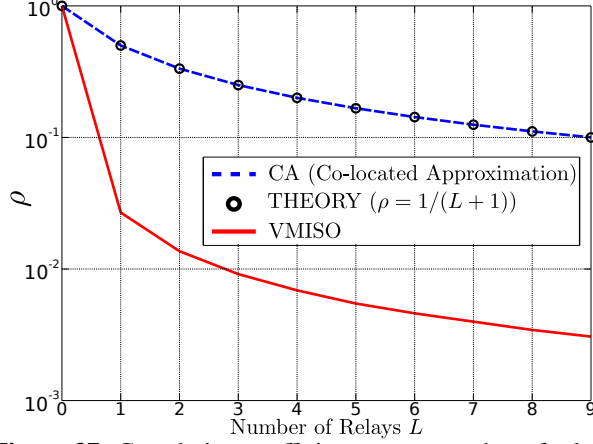


**Figure 37:** Correlation coefficient versus number of relays  $L$

two received powers  $P_F$  and  $P_R$ , which is one measure of link asymmetry, is given by

$$\rho = \frac{\text{COV}\{P_F, P_R\}}{\sqrt{\text{VAR}\{P_F\} \text{VAR}\{P_R\}}}, \quad (49)$$

where  $\text{COV}$  denotes covariance. If excluding the random relay locations by the co-located assumption, which means  $d_{F:i} = d_{R:j} = d_0$  for all  $i$  and  $j$ ,  $\rho$  simplifies to  $\frac{1}{\sqrt{(M+1)(N+1)}}$ , because the only common component between  $P_F$  and  $P_R$  is  $\Omega_{F,0} = \Omega_{R,0}$ , while the other channel power components are independent.

#### 6.2.2.2 Path-loss Disparity in VMISO

As shown in Section 6.1, the multiple SISO links between the transmitters (the relays and cluster head of the current cluster) to the receiver (the cluster head in the other cluster) have dissimilar path losses, which means  $\lambda_{v:w} \neq \lambda_{v':w'}$  when  $v \neq v'$  or  $w \neq w'$ . For this reason, the received power  $P_v$  follows the hypoexponential distribution in (37) instead of the gamma distribution in (38).

We can use  $\sigma^2$  in (46) as an indicator of the degree of the path-loss disparity. By using this  $\sigma^2$ , we can estimate how the impact of the path-loss disparity, which can be modeled as log-normal shadowing, changes depending on system parameters such as the path-loss exponent  $\alpha$ , the distance ratio  $r_s/d_0$ , and the number of relays  $L$ .

Figure 37 shows the impact of the path-loss disparity on  $\rho$ , where the vertical axis indicates the correlation coefficient  $\rho$  in a log scale and the horizontal axis in a linear scale indicates the number of relays  $L$ , assuming the same number of relays  $M = N = L$ . In the

figure, the blue dotted line, which is labeled with ‘CA’ in short, indicates  $\rho$  obtained from  $10^6$  random Rayleigh fading samples for the co-located case, while the circles labeled with ‘THEORY’ represent the theoretical curve  $\rho = 1/(L + 1)$ . The two (CA and THEORY) graphs show the identical results, as we expected. Lastly, the red line indicates the correlation coefficient  $\rho$  of the VMISO links obtained by  $10^6$  samples in the presence of path-loss disparity by the random relay locations, when  $d_0 = 3$ ,  $r_s = 1$ , and  $\alpha = 4$ . For all the three graphs,  $\rho$  decreases as  $L$  increases, because each cluster head is the only receiver of a VMISO link. Also, as shown in the figure, the red curve (VMISO) is always smaller than the blue line (CA), which means  $P_F$  and  $P_R$  become much less correlated by the random relay locations and the corresponding disparate path losses.

### 6.2.3 Link Asymmetry Quantified by Power Ratio

As shown in the previous section, the forward and reverse VMISO links become less correlated as the number of relays increases, because of the exclusive reception at the cluster head and the disparate path losses by the random relay topologies. However, from the higher-layer perspective, the received power difference of the two VMISO links, which can be translated into the error rate gap, is more practical than the correlation  $\rho$ . Therefore, in this section, we use the ratio of the signal powers of the two links as  $\eta = \frac{P_R}{P_F}$  to quantify the link asymmetry of the forward and reverse links.

#### 6.2.3.1 Probability Distribution of $\eta = \frac{P_R}{P_F}$

It is difficult to obtain a closed form expression for the probability distribution of  $\eta = \frac{P_R}{P_F}$ , because of the disparate path losses and the common elements ( $h_{0,0}$  and  $g_{0,0}$ ) of the two VMISO links, which makes  $0 < \rho < 1$ . Therefore, we can only calculate the probability distribution of  $\eta$  by simulation with random samples or numerical computation. On the other hand, in the absence of path-loss disparity and when  $h_{0,0}$  and  $g_{0,0}$  are also independent (e.g., FDD), the CDF of  $\eta = \frac{P_R}{P_F}$  can be obtained by using the outage probability (17)

in [69], which is derived to calculate the outage rate determined by signal-to-interference-ratio (SIR) with independent Nakagami signal and Nakagami interference. Applying our system parameters, the CDF of  $\eta$  in this case, denoted by  $F_\eta^*$ , is given by

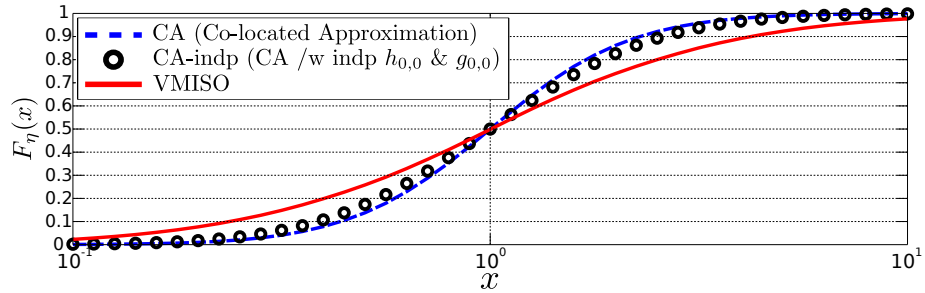
$$F_\eta^*(x) = \left(1 + \frac{1}{x}\right)^{1-M-N} \cdot \sum_{k=0}^{N-1} \binom{M+N-1}{k} \left(\frac{1}{x}\right)^k. \quad (50)$$

Because the true CDF  $F_\eta(x)$  without any approximation, which includes the path-loss disparity and the common channel elements  $h_{0,0} = g_{0,0}$ , does not give a closed form, the CDF  $F_\eta^*(x)$  in (50) can be used to estimate the degree of the link asymmetry, when path-loss disparity is small enough (i.e.,  $\sigma^2$  in (46) is small) with large  $M$  and  $N$  (i.e.,  $\rho$  in (49) is small).

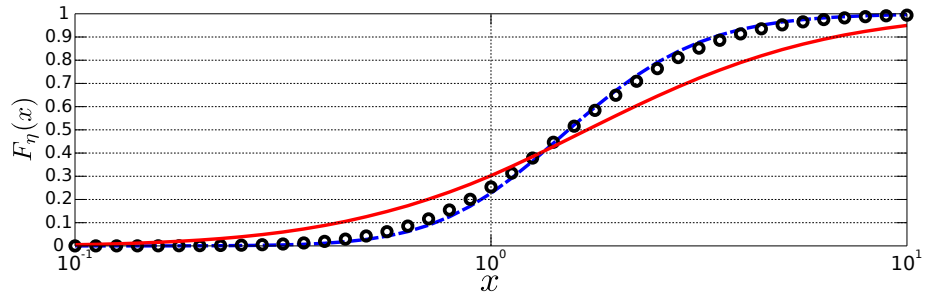
Figures 38 (a) and (b) show the CDFs  $F_\eta(x)$  with the same number of relays ( $M = N = 3$ ) and different number of relays ( $M = 5$  and  $N = 3$ ), respectively, when  $d_0 = 2$ ,  $r_s = 1$ , and  $\alpha = 4$ . In the figures, the x-axis indicates the ratio  $\eta = \frac{P_R}{P_F}$  in a log scale, while the y-axis is the corresponding cumulative probability in a linear scale. In each figure, the black circles labeled with ‘CA-indp’ in short represent the theoretical CDF in (50) that ignores the common SISO link between the two cluster heads (i.e.,  $h_{0,0}$  and  $g_{0,0}$  are assumed to be independent) in the absence of the path-loss disparity. Moreover, the blue dotted line labeled with ‘CA’ and red solid line labeled with ‘VMISO’ indicate the CDF of the co-located approximation and the true VMISO CDF, respectively. Because  $F_\eta(x) = \Pr[\eta = \frac{P_R}{P_F} \leq x]$ ,  $F_\eta(x) = \Pr[P_R \leq x \cdot P_F]$ , while  $1 - F_\eta(x) = \Pr[P_R > x \cdot P_F]$ . Therefore, as the length of the left and right tails increase, an extreme case with a very small or large ratio  $\eta$  becomes more likely, which means the link asymmetry of the two VMISO links gets more severe. With this interpretation, the true VMISO curve indicated by the red solid line is more asymmetric than the co-located approximation indicated by the blue dotted line in both figures. Moreover, the black circles, which represent  $F_\eta^*(x)$  in (50), indicate show slightly more asymmetric links with the longer tails than the blue curve, because the approximate CDF  $F_\eta^*(x)$  assumes that  $h_{0,0}$  and  $g_{0,0}$  are independent.



If comparing the two figures, all the three graphs in Figure 38a are symmetric about the point  $(x, y) = (1, 0.5)$ , while in Figure 38b  $F_\eta(1) < 0.5$  for all the three curves, which means  $\mathbb{E}\{\eta\} < 1$ . In other words, statistically  $P_F > P_R$  in Figure 38b, because the source cluster has more number of relays than the destination cluster. In contrast, in Figure 38a, all the three curves satisfy  $F_\eta(x) = 1 - F_\eta(1/x)$  by the symmetry about the mean point  $(x, y) = (1, 0.5)$ . Therefore, for more balanced powers in the both directions, the clusters in multi-hop networks should use the same number of relays. In fact, the authors in [1] propose that all the clusters on a multi-hop CT-based route have to use the same number of nodes to avoid the link asymmetry for their link-layer algorithm, which is a modified version of *IEEE 802.11* MAC. However, the use of a fixed number of nodes cannot completely solve the link asymmetry issue caused by the inherent characteristics of the VMISO communication, which is ignored in [1], as we can see the long tails in Figure 38a.



(a)  $F_\eta(x)$  with  $M = N = 3$



(b)  $F_\eta(x)$  with  $M = 5$  and  $N = 3$

**Figure 38:** Two CDFs of  $\eta = \frac{P_R}{P_F}$  with  $d_0 = 2$ ,  $r_s = 1$ , and  $\alpha = 4$

### 6.2.3.2 Parametric Study

In this section, we observe the variation in the VMISO link asymmetry depending on the three system parameters: the distance ratio  $d_0/r_s$ , the path-loss exponent  $\alpha$ , and the number of relays  $L$ . We assume the same number of relays for the both clusters  $M = N = L$  as a prerequisite to minimize asymmetry compared to the case with  $M \neq N$ . To measure the degree of the link asymmetry, we look at the probability  $p_{2X}$  that the difference of the two powers,  $P_F$  and  $P_R$ , is greater than or equal to 3dB. This probability  $p_{2X}$  can be expressed using  $F_\eta(x)$  by its symmetry as

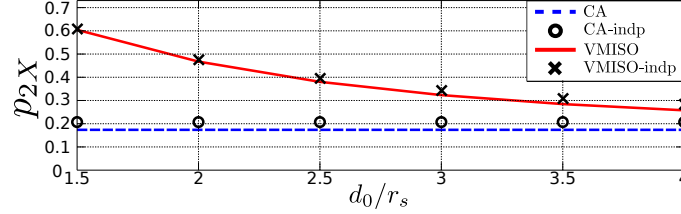
$$p_{2X} = \Pr[P_F \geq 2P_R] + \Pr[P_R \geq 2P_F] = 2 \cdot F_\eta(1/2). \quad (51)$$

In the simulation results in Figures 39, 40, and 41, there are four graphs in each figure: the co-located approximation (the blue dotted line), the theoretical curve assuming independent  $h_{0,0}$  and  $g_{0,0}$  in (50) (the black circles), the true VMISO result curve (the red solid line), and the VMISO with path-loss disparity but assuming independent  $h_{0,0}$  and  $g_{0,0}$  (the black ‘x’-markers). We label the four curves with ‘CA’, ‘CA-indp’, ‘VMISO’, and ‘VMISO-indp’. If we look at the VMISO curves indicated by the red solid lines in the three figures, the link asymmetry is very severe, because  $p_{2X}$  varies from about 0.25 to 0.6 for all parameter variations.

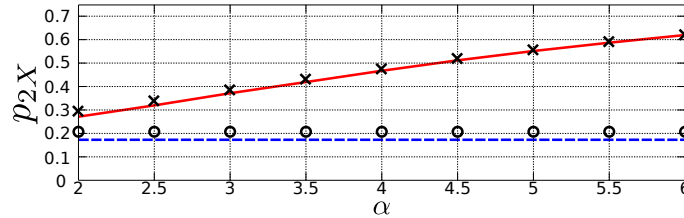
Figure 39 displays the probability  $p_{2X}$  indicated by the y-axis for the different distance ratio  $d_0/r_s$  indicated by the x-axis, when  $\alpha = 4$  and  $L = 6$ . In the figure, only the VMISO and VMISO-indp graphs, which correspond to the red solid line and black ‘x’-markers, decrease, as the distance ratio  $d_0/r_s$  increases, while the other two, CA and CA-indp, do not change. The decrease of the VMISO graphs happens because the path-loss disparity, which can be estimated by  $\sigma^2$  in (46), becomes more severe, as  $d_0/r_s$  increases. For the same reason, the VMISO group shows always higher  $p_{2X}$  than the CA group that ignores the path-loss disparity by the random relay locations. Also, the gaps within the same groups (CA-to-CA-indp and VMISO-to-VMISO-indp) are very small, since the single common SISO link ( $h_{0,0} = g_{0,0}$ ) has very little effect when  $L = 6$ .

Figure 40 shows the impact of the path-loss exponent  $\alpha$  on  $p_{2X}$ , when  $d_0/r_s = 2$  and  $L = 6$ . The VMISO group graphs increase, as  $\alpha$  increases, because the path losses of the different relays become more dissimilar, as  $\alpha$  increases. We note that  $\sigma^2$  in (46) is an increasing function of  $\alpha$ , which is consistent with the simulation results in Figure 40. On the other hand, similarly to the previous results in Figure 39, the other two results (CA and CA-indp) stay the same, because they are obtained by the co-located approximation.

In the last figure, Figure 41, the four graphs show how the number of relays  $L$  affects  $p_{2X}$  with  $d_0/r_s = 2$  and  $\alpha = 4$ . In contrast to Figures 39 and 40, both the CA and VMISO groups have the identical trends:  $p_{2X}$  decreases for  $L \geq 2$ , as  $L$  increases. For small  $L$ , the two graphs in the same group (e.g., VMISO-to-VMISO-indp and CA-to-CA-indp) give a large gap, because the correlation  $\rho$  is high for small  $L$  as in Figure 37. In general, since the correlation  $\rho$  decreases for all the four cases corresponding to the four graphs, the link



**Figure 39:**  $d_0/r_s$  versus for  $\alpha = 4$  and  $L = 6$



**Figure 40:**  $\alpha$  versus for  $d_0/r_s = 2$  and  $L = 6$

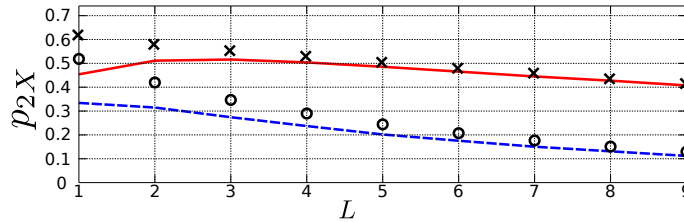


**Figure 41:**  $L$  versus for  $d_0/r_s = 2$  and  $\alpha = 4$

asymmetry must be reduced by diversity, as  $L$  increases. In case of fully uncorrelated forward and reverse links, it is very unlikely to have extremely large or small power ratio  $\eta$  because of diversity by using many nodes. For example, if plugging  $M = N = L$  and  $x = 0.5$  into (50), we can calculate the  $p_{2X}$  of the CA-indp case in the figure as

$$p_{2X}^* = 2 \cdot F_\eta^*(1/2) = 3^{1-2L} \cdot \sum_{k=0}^{L-1} \binom{2L-1}{k} \cdot 2^{k+1}, \quad (52)$$

which is a monotonically decreasing function of  $L$ , because the first exponential term,  $3^{1-2L}$ , is dominant for a large  $L$  compared to the remaining terms. Hence,  $p_{2X}$  decreases, as  $L$  increases in this case.

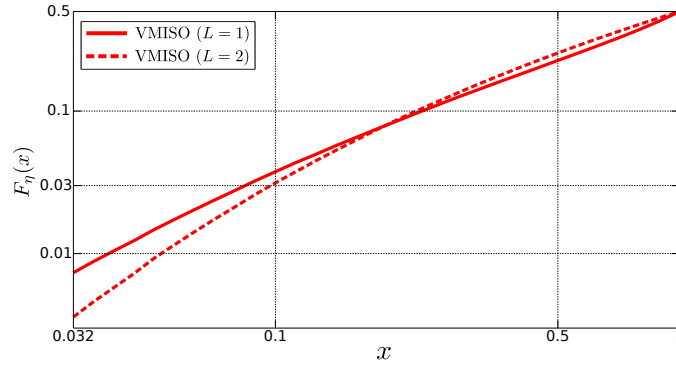


**Figure 42:**  $F_\eta(x)$  with  $L = 1$  and  $2$  for  $d_0/r_s = 2$  and  $\alpha = 4$

In contrast, the VMISO graph increases, as  $L$  changes from one to two. However, it is just because we look at the tail probability that the two powers have more than 3dB gap, which is denoted by  $p_{2X} = 2 \cdot F_\eta(0.5)$ . If we look at the probability with even a higher power gap, for example  $p_{10X} = 2 \cdot F_\eta(0.1)$ ,  $L = 1$  gives a higher probability than  $L = 2$ . Figure 42 shows the CDFs  $F_\eta(x)$ , which indicated by the y-axis, with  $L = 1$  and  $2$  for  $0.031 \leq \eta \leq 1$  as indicated by the x-axis, when  $d_0/r_s = 2$  and  $\alpha = 4$ . In the figure, the curve with  $L = 1$  is represented by the solid red line, while the  $L = 2$  curve is indicated by the red dotted line. As shown in the figure,  $L = 1$  gives lower  $F_\eta(0.5) = 0.5 \cdot p_{2X}$  than  $L = 2$ , while the order is opposite for  $F_\eta(0.1) = 0.5 \cdot p_{10X}$ . Therefore, we can say the link asymmetry level decreases by the influence of the diversity, as  $L$  increases, which also makes  $\rho$  decrease.

### 6.3 Summary

In this chapter, we explore two issues of the VMISO link model assuming the centralized architecture: path-loss disparity and link asymmetry. In Section 6.1, we analyze the impact of the path-loss disparity in the VMISO link, where physically-separated multiple nodes transmit together to a single destination node, using the high SNR assumption. By the asymptotic analysis ( $\text{SNR} \rightarrow \infty$ ) of the outage capacity, we show that the performance loss by the path-loss disparity has the same model as log-normal shadowing. The simulation results show how the error of the co-located assumption changes depending on the system parameters such as  $d_0/r_s$ ,  $\alpha$ , and  $N$ . Moreover, the derived bounds can be used to estimate this error of the co-located VMISO model in the high SNR regime.

In Section 6.2, we study the link asymmetry between the forward and reverse VMISO links, where physically separated nodes in one cluster transmit together to a single receiver node in the other cluster. We present the two main causes of the VMISO link asymmetry, which the conventional SISO links do not experience: the exclusive signal reception of the cluster head and the path-loss disparity. We present the level of the VMISO link asymmetry by two measures: the power correlation  $\rho$  and the power ratio  $\eta$  of the forward and reverse links. Moreover, we show the relationship between the VMISO link asymmetry with the system parameters such as  $d_0/r_s$ ,  $\alpha$ , and  $L$ . Also, the simulation results on  $p_{2X}$ , which tells the probability that two powers have more than 3dB difference, indicate that VMISO link asymmetry can be much more severe than SISO links, which cannot be expected by the co-located approximation. Hence, the results in this chapter should sensitize designers of CT-based higher-layer protocols that require bidirectional links to the situation that successful decoding of a packet in the forward direction is little guarantee that a similar packet will be decoded in the reverse direction.

## **CHAPTER 7**

### **EXPERIMENTAL STUDIES OF CONCURRENT COOPERATIVE TRANSMISSION**

The testbed and measurement environment are described in this section for two experimental studies: the two-hop range extension and the OLA-based routing (OLAROAD). The different settings of the two experiments such as topology, packet design are presented in Sections 7.1 and 7.2, respectively.

#### **7.1 Two-hop Range Extension of Concurrent Cooperative Transmission**

The first experimental study is focused on the CCT range extension, which is the widely used property in many CCT- and other CT-based protocols. To be specific, in this section, the experimental range extension by two-hop CCT are compared with non-CT in a typical modern office environment described in the previous section.

##### **7.1.1 Experiment Design**

The purpose of this study is to compare the maximum range reached in two hops by conventional non-CT and CCT (or CT). For the conventional non-CT, the two hops are built with two consecutive SISO links. For CT, as shown in Figure 44, the first-hop links are also SISO links as in non-CT. However, the second-hop link is multiple-input-single-output (MISO) created by multiple physically separate radios and a single destination radio, so that the second-hop receiver (destination) can exploit CT diversity for synchronization. For performance metric, the average packet error rate (APER) at the second-hop receiver is calculated over 120 multi-path fading channel realizations.

#### *7.1.1.1 Node Description*

Since no commercial off-the-shelf radio supports CCT, the testbed in the experiments is implemented using a Universal Software Radio Peripheral 1 (USRP1) [70] and GNU Radio software-defined radio (SDR). The USRP1 is a hardware platform that allows a software radio to be implemented in a general purpose processor. The USRP1 system consists of a radio frequency (RF) daughter board as an RF front-end and a main board that has an analog-to-digital converter (ADC), a digital-to-analog converter (DAC), an field-programmable gate array (FPGA), and Universal Serial Bus (USB) interfaces. The data streamed over the USB interface is in the form of 32-bit I/Q samples that consist of a 16-bit in-phase component and a 16-bit quadrature component. GNU Radio is used as a base-band signal processing module, which operates on a personal computer (PC) attached to the USRP1 via the USB interface [71]. GNU Radio is an open-source software package that is usually run on a Linux operating system. Also, GNU Radio has various signal processing blocks written in the C++ language and protocol stacks written in the Python language.

#### *7.1.1.2 Measurement Environment*

The experiments are conducted on the fifth floor of the Centergy building of the Georgia Institute of Technology, Atlanta, GA. The floor plan of this typical academic office building in Figure 43 consists of research laboratories, offices and conference rooms. The straight corridors, which have the offices on the one side and relatively large laboratories on the other, can be considered as LOS channels. The interior walls of the building are made of wallboard with steel studs, and the stairwells and the elevator columns are made of reinforced concrete. For this reason, the center of the building around the elevator lobby attenuates radio signals significantly.

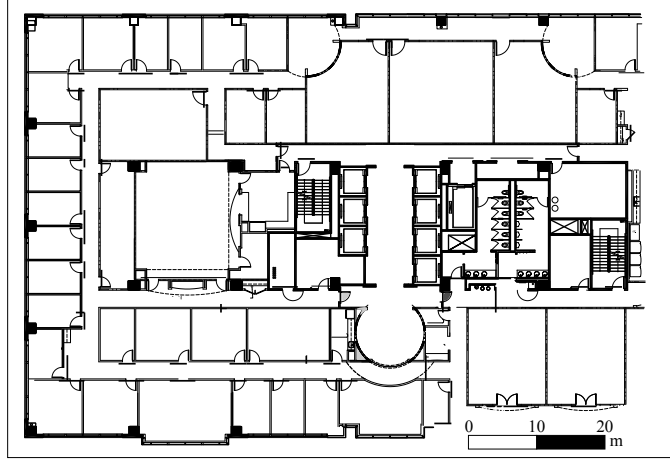


**Figure 43:** Floor plan of the measurement environment.

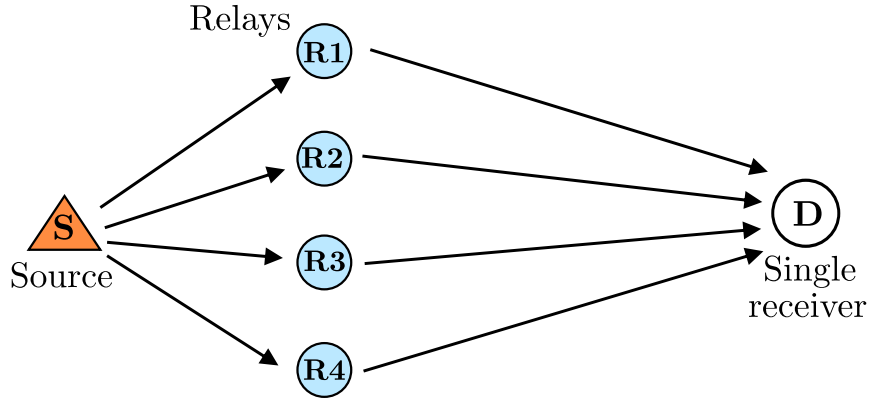


**Figure 44:** The logical topology of the experiment.

The 120 channel realizations are achieved as follows. First, as shown in Figure 45 (a), 15 radios are placed on the receiver cart with a sufficient inter-element spacing (about 1.5 wavelengths) that satisfies the condition for the uncorrelated multi-path fading and suppresses the mutual coupling effect [72]. The 15 radios on the receiver side are just for the purpose of creating 15 multi-path channels at the same time in one measurement phase of 1,000 packets. Second, each of the four relays (see one relay in Figure 45 (b)) is moved around to eight distinct locations in a local area. Through this procedure,  $15 \times 8 = 120$  channel realizations can be achieved. For the comparison between the conventional non-CT (SISO) and CT, the best (lowest) APER is selected among the four SISO APERs, and



the best APER is compared with the CT APER.

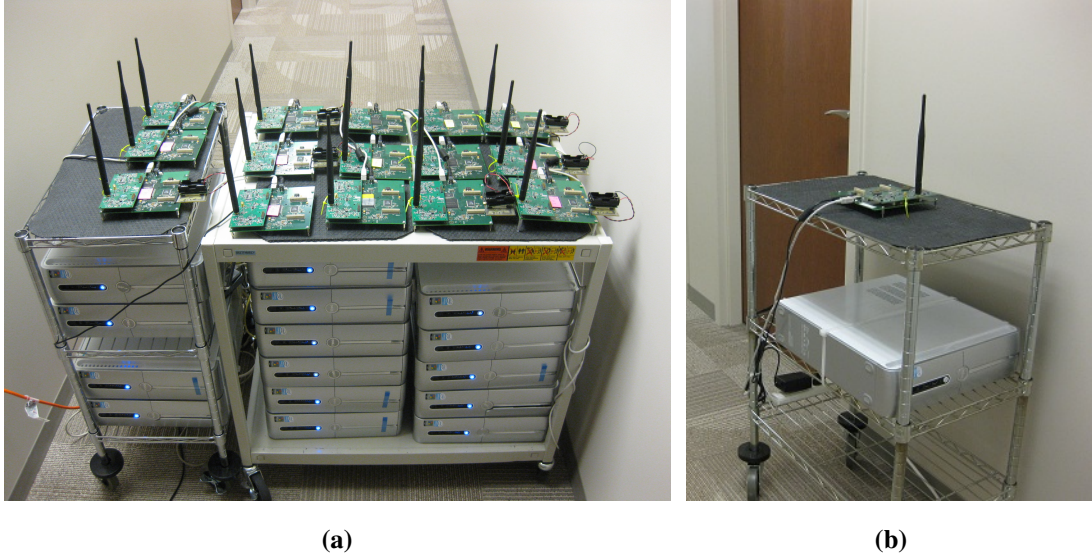


**Figure 45:** Testbed nodes: (a) the receiver cluster, (b) one relay node.

The transmit frequency of the source (the receive frequency of the first-hop receivers) is 2.482GHz. In the second hop, each transmitter uses a unique carrier frequency, with 128 kHz separation between adjacent carrier frequencies, to create the orthogonal diversity channels. The collection of carriers is centered at 2.492GHz to avoid WiFi interference. Non-coherent binary frequency shift keying (BFSK) is chosen for its high energy efficiency and low implementation complexity. Also, no error-correction coding is used. Equal gain combining and a mean-based method of transmit time synchronization is used [54]. To minimize the distortion caused by the different hardware, all the radios are calibrated to have the same receiver sensitivity. The packet is 22 bytes long, consisting of four bytes preamble, six bytes header, ten bytes data and two bytes cyclic redundancy check (CRC). A relay node transmits only if CRC check passes.

### 7.1.2 Measurement Campaign with Three Topologies

The measurement campaign consists of three stages corresponding to the three relay topologies, which are displayed in Figure 46. The three topologies are *i*) wide dispersion (indicated by the squares), *ii*) medium cluster (the circles), and *iii*) tight cluster (the dots). For all three topologies, the relays are maximally far from the source such that the first-hop APER is less than 0.01 to focus more on the second-hop decoding range. The second-hop decoding region is defined as the area where the second-hop APERs are less than or equal to 0.1. Of course, the decoding region will change depending on the receiver sensitivity and the transmit power. Any changes in the ratio of transmit power to receiver sensitivity that are large enough to change the shadowing statistics would change the relative sizes of CT and non-CT decoding regions.

The three topologies are motivated as follows. Wireless channels exhibit path loss, multi-path fading, and shadowing. If the relays are close enough to share the same path loss and shadowing, yet have sufficient separations (at least a half wavelength in an indoor environment) to achieve uncorrelated multi-path fading, then CT delivers the maximum micro-diversity gain. This relay topology with the maximum micro diversity is consistent with a real array antenna, where the transmitters are connected by wire on the same platform. However, with CT, the elements in the *virtual array* are less constrained than the real array, because the nodes in the virtual array are physically separate radios not connected by wire. Therefore, if the CT radios are separated by more than the shadowing correlation distance (e.g., about 1.7 meters for indoor NLOS channel [73]), then macro-diversity gain is also achievable. However, the path losses would be very different if the inter-element spacing is very large, which would be the case in a low-density network. In this case, some relays' contributions to the diversity gain will be very small, possibly leading to an effective diversity order less than the number of relays doing CT. Therefore, the cluster topologies are designed to capture the three cases: micro diversity only (tight cluster), full-order micro and macro diversity (medium cluster), and reduced effective diversity (wide dispersion)

because of disparate path losses.

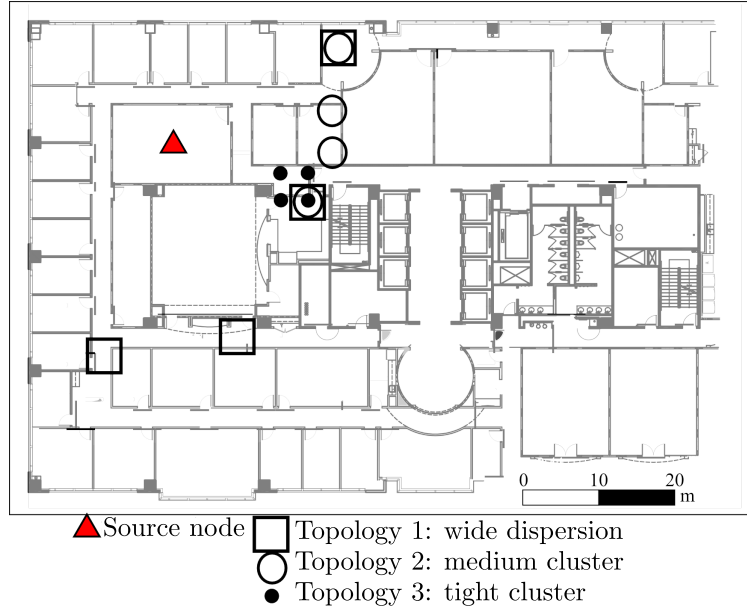


**Figure 46:** Three measurement topologies.

#### 7.1.2.1 Log-distance Path Loss Model

In this section, the channel model of the measurement environment is derived using SISO packet error rate (PER) measurement data. The channel model includes path loss exponent and log-normal shadowing parameter. In the next section, these parameters are used to calculate APER outage rates theoretically. Finally, the experimental results are compared with the simulation results based on the theoretical model using the parameters in this section.

First, without considering burst errors, the relationship between PER and bit error rate (BER) for the  $i$ th multi-path realization can be formulated by

$$BER_i = 1 - (1 - PER_i)^{1/D}, \quad (53)$$

where  $D$  is the packet length in bits that is 176 in the experiment. For non-coherent BFSK modulation, the BER as a function of the received SNR  $\gamma_i$  is

$$BER_i = \frac{1}{2} \exp\left(-\frac{1}{2}\gamma_i\right), \quad (54)$$

where  $\gamma_i = \frac{\beta_i^2 E_b}{N_0}$ , when  $E_b$  is the bit energy,  $N_0$  is the noise power spectral density, and  $\beta_i$  is the channel gain of the  $i$ th multi-path realization that is assumed to be constant during the 1,000 packets used to calculate  $PER_i$ . Thus, by combining (53) and (54), a unique value of  $\gamma_i$  can be obtained for each unique value of  $PER_i$ . Next, the average received SNR, which is averaged over 120 channel realizations within the local area of the receiver location, can be calculated as

$$\bar{\gamma} = \frac{1}{120} \sum_{i=1}^{120} \gamma_i. \quad (55)$$

Now, log-distance path loss model can be applied to the second-hop. Let  $d$  be the distance from the transmitter (relay) to the destination (the second-hop receiver),  $d_0$  be the reference distance, and  $\alpha$  be the path loss exponent. Note that  $d_0$  is a short reference distance that is in the far field of the antennas but short enough that free-space path loss applies. When  $X_\sigma$  is a random variable representing shadowing (Gaussian distribution in decibel (dB) scale with zero-mean and standard deviation  $\sigma$ ), then the received power  $P_R(d)$  is given by

$$P_R(d)_{(\text{dBm})} = 10 \log_{10} \frac{P_R(d_0)}{0.001W}_{(\text{dBm})} - 10\alpha \log_{10} \frac{d}{d_0}_{(\text{dB})} + X_{\sigma(\text{dB})}. \quad (56)$$

Since the radios are calibrated to have the same noise power spectral density, the log-distance path loss model can be rewritten in terms of an average SNR in the dB scale as

$$\bar{\gamma}(d)_{(\text{dB})} = \gamma(d_0)_{(\text{dB})} - 10\alpha \log_{10} \frac{d}{d_0} + X_{\sigma(\text{dB})}. \quad (57)$$

The standard procedure for estimating  $\alpha$  and  $\sigma$  is to do a linear regression on the set of ordered pairs  $(d, \bar{\gamma}(d))$ , with the constraint that the line passes through  $(d_0, \gamma(d_0))$  [64]. The SISO measurement data, which is derived from (57), is shown in Figure 47 with the horizontal axis of log-distance and the vertical axis of path loss values. The linear regression gives the path loss exponent of  $\alpha = 2.912$  and the standard deviation of shadowing of  $\sigma = 5.089$ , which are similar to the numbers reported for 2.5GHz and indoor environments in [74] (e.g.,  $\alpha = 2.4$  and  $\sigma = 5.8$ ).

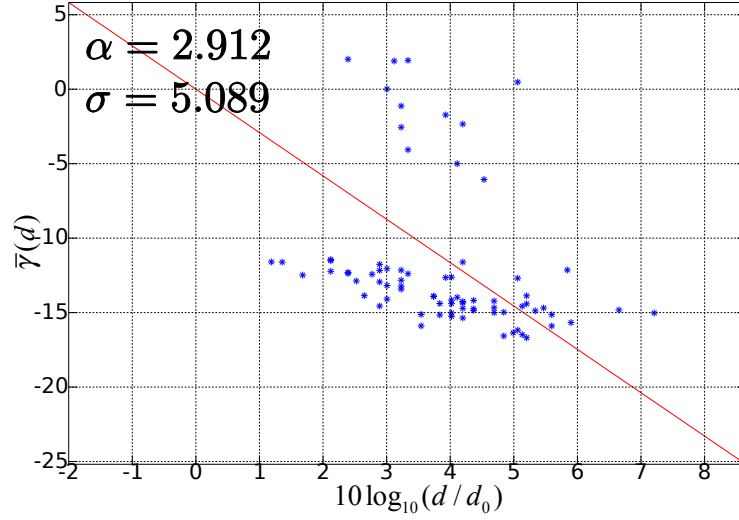


**Figure 47:** Scatter plot of  $\bar{\gamma}(d)$  and its linear regression.

#### 7.1.2.2 CCT Outage Model

Suppose that an outage is declared, when  $\text{APER} > 0.1$ . Using (53) and (54), this APER threshold of 0.1 can be transformed into an SNR threshold of about 11.3dB. Using the values of  $\alpha$  and  $\sigma$  from the previous section, the outage probability for a SISO link can be defined as

$$\Pr\{\bar{\gamma}(d)_{\text{(dB)}} < 11.3\text{dB}\} = 1 - Q\left(\frac{11.3 - \mu_{\bar{\gamma}}(d)}{\sigma}\right), \quad (58)$$

where  $\mu_{\bar{\gamma}}(d)$  is the expected value of  $\bar{\gamma}(d)$  in (57) over the outcomes of  $X_{\sigma}$ . For example,  $\Pr\{\bar{\gamma}(d)_{\text{(dB)}} < 11.3\text{dB}\} = 0.02$  implies a two percent chance that  $\text{APER} > 0.1$ .

However, when it comes to CCT, obtaining a closed form for outage probability is difficult because of the multiple transmitter-receiver pairs with correlated shadowing. The diversity-combining scheme in the experiment is non-coherent (post-detection) equal gain combining where the total received SNR is the sum of SNR from each link [75]. Hence, when the number of the transmitters is  $L$ , the outage probability is given by

$$\Pr\{\gamma_{\text{cct}} < 10^{11.3/10}\} = \Pr\left\{\sum_{k=1}^L \gamma(d_k) < 10^{11.3/10}\right\}, \quad (59)$$

where  $d_k$  is the distance from the  $k$ th first-hop relay to the destination at the second-hop. When  $k$  is the index for each link, and  $i$  is the index for one multi-path trial, the random

variable  $\gamma(d)$  is determined by path loss, multi-path fading, and shadowing as  $\gamma_i(d_k) = \beta_i^2(d_k) \cdot (E_b/N_o) \cdot X_{\sigma(k)}$ . With Rayleigh fading,  $\beta_i^2(d_k)$  follows the exponential distribution. Also,  $X_{\sigma(k)}$  is spatially correlated shadowing for different paths indexed by  $k$ . Because multiple transmitters send signals to the same receiver in the second hop, the correlation model in [76] can be used, which gives the correlation of the two links with the transmitter separation of  $d_S$  as

$$R(s) = \sigma^2 e^{-d_S/D_S}, \quad (60)$$

where  $D_S$  is the de-correlation distance, which is the distance from one transmitter to another such that the correlation is dropped by a factor of  $e^{-1}$ . The authors in [73] reported the de-correlation distance of  $1.7m$  based on the measurements in a similar indoor environment with the center frequency of  $1.8GHz$ .

### 7.1.3 Experimental Results

The experimental second-hop decoding regions and the APERs of the three relay deployments are depicted in Figures 48 (a), 49 (a), and 50 (a). Moreover, the corresponding simulation results for the three topologies, which are compared to the measurement results in Section 7.1.3.3, are shown in Figures 48 (b), 49 (b), and 50 (b). The red triangles represent the source node, and the blue circles are the relays. The SISO decoding region is indicated by the light-gray areas, and the CCT decoding range is the union of the light-gray and dark-gray areas. The green squares are labeled with the APERs of some selected SISO destinations on the SISO decoding range boundaries. The white-filled circles indexed by the letters from A to V are labeled by APERs for four-relay CCT. As stated in the previous section, the APERs on the green squares and white-filled circles are averaged over 120 multi-path realizations. However, the APERs to decide the light and dark gray areas are averaged over only 15 multi-path trials, and the measurements are made at approximately three-meter intervals. The CCT destination locations are not the same for each topology, but some locations are common. For example, A, B, C and D are common for all the three

topologies. Also, E and F are common in the wide dispersion and medium cluster deployments. Lastly, seven measurement locations (L, M, N, O, P, Q, and R) are shared by the medium cluster and tight cluster deployments.

Two types of extensions can be considered: directional range and coverage area. Directional range extension is the increase of the second-hop decoding range from non-CT to CCT in one direction. Directional range extension is important, for example, in overcoming the energy hole problem [43]. Coverage area is one of the most popular network design factors; maximizing it often corresponds to minimizing cost.

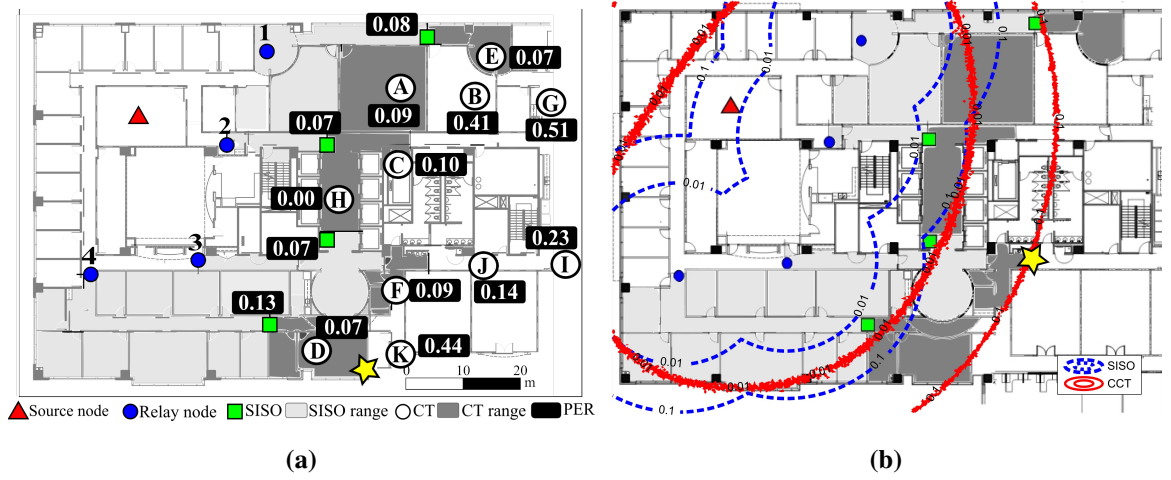


**Figure 48:** Topology1 (wide dispersion): (a) measurement, (b) experiment.

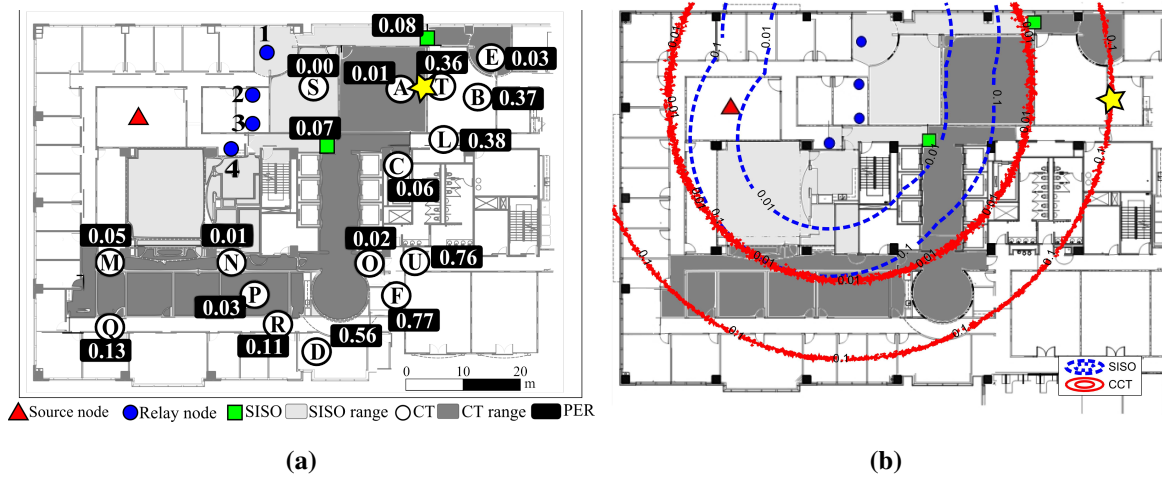


**Figure 49:** Topology 2 (medium cluster): (a) measurement, (b) experiment.

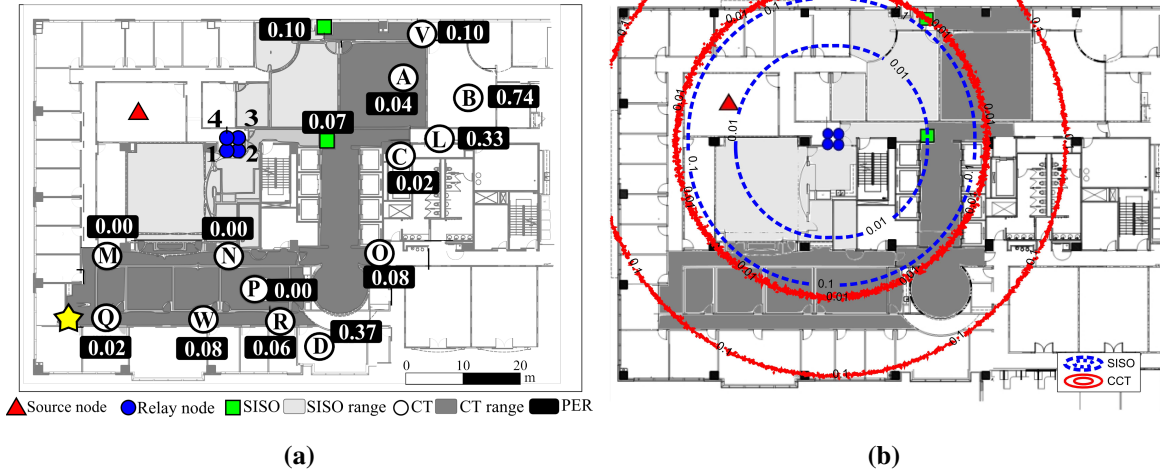


**Figure 50:** Topology 3 (tight cluster): (a) measurement, (b) experiment.

Note that the two extensions are strongly influenced by the location of the source within the building. The source node is in the upper left corner of the building, and the relays are placed to the opposite side of the corner instead of surrounding the source. Thus, the coverage areas are not disks but sectors. For this reason, APERs are not measured around the source (the white region surrounded by the light-gray area in the figures). Also, the heavy attenuation of the elevator lobby (the seven squares around H in Figure 48 (a)) and the bathrooms (on the right of the elevator lobby) limit the range extension in that direction. If the measurements were performed in a part of the building away from the building core, the range and coverage extension values would be higher.

#### 7.1.3.1 Directional Range Extension

The “direction” of the one-dimensional range extension in this experiment can be defined as the direction that corresponds to the maximum second-hop decoding range. Let  $\mathcal{S}_c$  be the set of locations  $(x_c, y_c)$  on the outer border of the CCT coverage region. Suppose  $(x_k, y_k)$  is the location of the  $k$ th relay, then the direction  $(x'_c, y'_c)$  can be defined as

$$(x'_c, y'_c) = \arg \max_{(x_c, y_c)} \left( \min_k |(x_c, y_c) - (x_k, y_k)| \right). \quad (61)$$



This means  $(x'_c, y'_c)$  is the point that maximizes the distance from the closest relay and itself. However, this definition does not consider the SISO range. For example, in the wide dispersion and the medium cluster cases, the directions following (61) would be toward the upper right edge of the dark-gray area around E in Figures 48 (a) and 49 (a), which is a LOS channel path where the SISO range is also long. Therefore, a new definition for the direction should be introduced as

$$(x'_c, y'_c) = \arg \max_{(x_c, y_c)} \left( \min_k \left| \frac{(x_c, y_c) - (x_k, y_k)}{(x_s, y_s) - (x_k, y_k)} \right| \right), \quad (62)$$

where  $(x_s, y_s) \in \mathcal{S}_s$  is the longest-range SISO reception point located on the straight line between  $(x_c, y_c)$  and the closest relay. The resulting directions of the topologies are indicated by the yellow stars in Figures 48 (a), 49 (a), and 50 (a). The ratios  $\rho_d = |[(x_c, y_c) - (x_k, y_k)] / [(x_s, y_s) - (x_k, y_k)]|$  in (62) are given in the “experiment” column of Table 4. The reason why the wide dispersed topology has the lowest  $\rho_d$  is that some relays are far from the destination and hardly contribute to the improvement in APERs because of the significant path losses. On the contrary, the medium cluster exploits both micro and macro diversity, which gives the largest  $\rho_d$ . On the other hand, the range extension of the tight cluster is based only on the array gain and micro diversity.

**Table 4:** Directional range-extension ratios  $\rho_d$ .

Topology	Experiment	0.1 contour	The direction difference
1. Wide dispersion	1.93	1.66	different (31.1°)
2. Medium cluster	2.18	1.84	almost same (5.7°)
3. Tight cluster	2.10	1.62	omnidirectional (simulation)

### 7.1.3.2 Coverage Area

The second-hop coverage area includes all destination locations within the decoding range of the four relays. Also, the coverage ratio of CT to non-CT is given by

$$\rho_c = \frac{\text{second-hop CT decoding area}}{\text{second-hop SISO decoding area}}, \quad (63)$$

where the denominator is the light-gray area and the numerator is the union of the light-gray and dark-gray areas. The results shown in the “experiment” column in Table 5 seem to favor the tight cluster topology, but the results hide the fact that the total CCT second-hop coverage area for the widely dispersed topology is larger than that of the other two. Also, the experimental results would vary, if the source location were not in the corner of the building. Another consideration is that the widely dispersed topology shows the largest SISO coverage among the three topologies, since the relays are placed on the corridors, which makes favorable LOS propagations, with the largest inter-spacing.

**Table 5:** Coverage-extension ratios  $\rho_c$ .

Topology	Experiment	0.01 contour	0.1 contour
1. Wide dispersion	1.589	1.634	1.568
2. Medium cluster	2.546	2.361	2.394
3. Tight cluster	2.700	2.533	2.357

### 7.1.3.3 Comparison of Measurements with Simulation Results

The simulation results are provided in Figures 48 (b), 49 (b), and 50 (b). The two blue dashed-contour lines represent the SISO destination locations with the outage probabilities of 0.01 (inner) and 0.1 (outer). Likewise, the two red solid lines correspond to the CCT destination locations with the outage probabilities of 0.01 (inner) and 0.1 (outer). Note that these numbers are not APERs, but the probabilities that the random APERs (because of shadowing) are greater than 0.1. The light-gray and dark-gray regions are copied from Figures 48 (a), 49 (a), and 50 (a), respectively, for reference.

One way to think about an outage contour is the following. If one could walk along a contour, for example, the 0.01 contour, then if the model is correct, one should find oneself in outage (i.e., outside of the relevant gray area) about one percent of the time. Therefore, the SISO 1% contour, for example, should be almost entirely inside the light gray area. With this interpretation in mind, the 1% contours for each of SISO and CT appear to fit the

data well. On the other hand, the 10% contours are far away from the relays. For example, in both the medium and tight relay topologies, the 10% contour is almost entirely outside of the gray areas.

This discrepancy is caused by the inaccurate parameter estimates, either because of the small samples or the ignored burst bit errors in derivation. The discrepancy could also be attributed to the simplicity of the log-distance path model (“multi-slope” models may be more appropriate [64]). Regarding directional range extension, the measured data in Figures 48 (a), 49 (a), and 50 (a) that the location of the yellow star is approximately broadside to the virtual array of relays (“broadside” means along a line that is nearly a perpendicular bisector of the “line” of the array).

The outage contours for the widely dispersed and medium cluster topologies produce yellow star locations that are also approximately broadside to the array. However, no correspondence between measurement and theory is found in the tight cluster case, because the contours are circles.

## **7.2 Demonstration of an OLA-based Routing Protocol**

The second experimental study demonstrates an OLA-based routing protocol known as OLAROAD, by comparing with AODV, which is a conventional non-CT routing protocol. In this section, the original version of OLAROAD is described to show how OLAROAD builds a route. Also, routing-failure problem in the original OLAROAD protocol is introduced with a proposed solution implemented in the testbed. In the following section, the network model of the testbed is presented. Then, the experimental results are presented in the last part of this section.

### **7.2.1 Original OLAROAD Protocol**

The OLAROAD protocol builds a cooperative route for a given source and destination pair. The original version of OLAROAD [77] constructs the route with a single control message handshake consisting of a route request (RREQ) and a route reply (RREP) for one unicast

flow. The simulation result in Figure 51 illustrates how OLAROAD creates the cooperative route, where the source is indicated by the red square at the center and the destination is denoted by the yellow star on the right of the source. Also, the gray dots and the black dots indicate the nodes not in the route and the nodes in the route, respectively. As described in [77], the source node initiates the route discovery by the OLA broadcast of an RREQ. This broadcast covers the network in successive OLA hops. The nodes that decode in  $i$ th hop form  $i$ th downstream level ( $DL^i$ ) indicated by the thick black concentric circles in Figure 51. When the relay nodes forward the RREQ message, they increment the hop count field (the downstream level) in the RREQ, so that each node identifies its own downstream level. In this way, the destination also achieves the cooperative hop count from the source to itself, e.g., the destination downstream level ( $DDL$ ) is three in Figure 51.

Upon reception of the RREQ, the destination node triggers an OLA-broadcast of an RREP message that contains the destination downstream level ( $DDL$ ) and the upstream hop-count field ( $UL^j$ ). The UL field in an RREP is incremented by the nodes relaying the RREP message similar to the RREQ transmission. However, unlike the forward path setup through the RREQ, the nodes can forward the received RREP, only when the sum of the downstream level ( $i$ ) and the upstream level ( $j$ ) is less than or equal to the destination downstream level ( $DDL$ ) plus one as given by

$$i + j \leq DDL + 1. \quad (64)$$

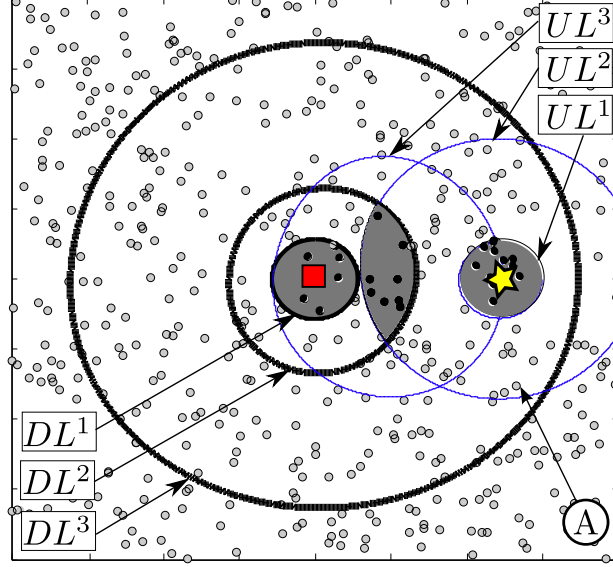


**Figure 51:** An example of the OLAROAD routing.

In Figure 51, for example, Node  $\textcircled{A}$  is in  $DL^3$  and in  $UL^2$ , then the sum is five, which is greater than four ( $=DDL+1=3+1$ ). Therefore, Node  $\textcircled{A}$  cannot forward the received RREP. On the other hand, the nodes that satisfy the condition, indicated by the black dots, forward the RREP message. Following this rule, this RREP broadcast also creates the upstream level boundaries shown by the thin blue contours in Figure 51, but unlike the downstream level boundaries, they are not concentric because of the cooperator selection. The nodes that satisfy (64) compose the “cooperative route.” In the DATA phase, the source sends the data as an OLA broadcast along the cooperative route. In other words, only nodes that participated in the RREP transmission are allowed to relay the data packets.

### 7.2.2 Protocol Modification

The previous version of OLAROAD before this research finishes the route construction when the RREP reaches the source. Therefore, the data transmission phase begins right after the single handshake (RREQ-RREP) has been completed successfully. Similar to OLAROAD, the BRN unicast routing also consists of a single handshake process. However, the cooperative route built through the single handshake might not work in some cases

because the OLAs in the RREQ phase, which are indicated by the concentric rings in Figure 51, are not the same as the OLAs of the cooperative route, which are limited to the gray shaded areas in Figure 51. Therefore, the ranges of the OLAs are different. For example, in Figure 51 the number of the cooperators at the second downstream level in the DATA phase is eight, which is about 25% of the cooperators in the RREQ phase. For the same reason, the data transmission takes four hops, while the RREQ takes only three hops to reach the destination. Moreover, it is also possible that the data transmission fails even if the RREQ-RREP handshake successfully finishes. Therefore, an additional handshake process is added to the OLAROAD protocol with two control messages called Route-Confirm (RC) and Route-Confirm Acknowledgement (RCACK). The second handshake process is triggered by the source through the RC message broadcast when the source receives the RREP in the first handshake process. Because the purpose of the second handshake is just to confirm that the cooperative route actually works, this packet has a simple format including Packet type, Source address, Destination address, and Broadcast ID. Only the nodes in the cooperative route can forward the RC packet. After the destination receives the RC packet, the destination sends an RCACK message back to the source. This message has the same fields in the RC, but Broadcast ID in the RCACK is managed by the destination node. This is a similar way to handle the destination sequence number in the control packets of AODV.

If the source receives the “RCACK” packet, then it finishes the route discovery process and starts the data packet transmission. If the source cannot receive the RREP in the first phase after sending an RREQ or cannot receive the corresponding RCACK in the second phase after sending an RC packet for a certain amount of time, then source will resend a new RREQ message with different parameters such as enabling some techniques such as ganging of levels, transmit power control, and step-size control proposed in [5].

### 7.2.3 Network Model

The OLAROAD routing protocol requires different types of physical and data/link layer protocol from the SISO-based ad-hoc routing scheme (i.e., AODV). In this section, each layer model to implement AODV and OLAROAD is described. For both routing protocols, all wireless nodes have only a single antenna with limited transmit power.

#### 7.2.3.1 Physical Layer

For the SISO communication link in the AODV protocol, BFSK with non-coherent reception (i.e., envelope detection) are used. FSK modulation enables a power efficient transmitter and a simple, low-cost receiver. On the other hand, the physical layer of OLAROAD uses CCT with transmit diversity, where each node is allocated one sub-frequency among four orthogonal sub-frequencies. A receiver for the OLAROAD protocol combines the multiple copies in the four orthogonal sub-channels using equal gain combining (EGC). To synchronize transmission times of the cooperators in the absence of a globally synchronized clock, the cooperators use the source message as a trigger signal [54]. The cooperators estimate the start of the packet (SOP) time and add a fixed amount of time  $T_{proc}$  to schedule transmission time. In [54], the authors showed that the transmission time errors of the proposed scheme are on the order of 100 nanoseconds in an indoor environment and the root mean square values converge with hop index.

#### 7.2.3.2 Data Link Layer

The data link layer consists of the media access control (MAC) and logical link control (LLC) sub-layers. In a SISO communication system, simultaneous transmissions from neighboring wireless nodes cause a collision and decoding is not possible. Typically, most wireless MAC layer standards rely on physical carrier sensing (e.g., carrier sense multiple access with collision avoidance (CSMA/CA) in IEEE 802.11 and IEEE 802.15.4) while a virtual-carrier sensing (e.g., request-to-send (RTS) and clear-to-send (CTS) in IEEE 802.11) is optional. In IEEE 802.11, RTS/CTS is used, only when a data packet size is larger than “RTS/CTS threshold.” The IEEE 802.11 specification [78] shows that the peak

throughput can be achieved when the RTS/CTS threshold is around 250~500 octets. In this experiment, RTS/CTS is not used because the data packet size is small (100 bytes). For link reliability, which is a function of LLC, a data acknowledgment (ACK) scheme is used. After a receiver correctly receives a data packet, the receiver sends an acknowledgment (ACK) to the transmitter. If an ACK is not received by the transmitter within a short timeout period, the transmitter attempts to retransmit the data packet up to seven times [79]. If no ACK is received after seven retries, the data packet is abandoned and an error is reported to the network layer.

#### 7.2.3.3 *Network Layer*

For the comparison target to OLAROAD, the widely used non-CT routing protocol, AODV is chosen [36]. The implementation of AODV follows the requirements specified in [36], such as the message formats. The AODV control messages are sent to port 654 using the User Datagram Protocol (UDP). Also, the configuration parameters, most of which are the default values in *GTNetS* [80], are shown in Table 6. However, “NODE TRAVERSAL TIME” and “NETWORK DIAMETER” are adapted corresponding to the processing time of the testbed and the network size in the experiments. Also, local route repair is performed only for the nodes that are in the route.

OLAROAD handles the routing process using UDP that has the port number of 655. As in AODV, the originating node in OLAROAD sets the timeout for receiving an RREP after sending an RREQ. However, unlike AODV, OLAROAD has another timer for the second handshake process (RC-RCACK). If the second handshake fails, the source will try the route discovery again with a new RREQ.



**Table 6:** Configuration parameters in AODV implementation.

Parameter	Value
MY ROUTE TIMEOUT	10 sec
ACTIVE ROUTE TIMEOUT	10 sec
HELLO INTERVAL	1 sec
ALLOWED HELLO LOSS	3
RREQ RETRIES	3
TTL START	7
TTL THRESHOLD	13
TTL INCREMENT	2
NETWORK DIAMETER	13
NODE TRAVERSAL TIME	0.15 sec

#### 7.2.4 Experimental Results

The experimental design and the corresponding results of the two routing protocols, AODV and OLAROAD, are presented in this section. The metrics used in the routing performance comparison are packet delivery ratio (PDR), end-to-end hop count, end-to-end round trip time, and route discovery time.

The experiment is conducted using eighteen nodes that are described in Section 7.1.1.1. The nodes are deployed as shown in Figure 52. In the figure, the eighteen nodes are placed in the corridors, with office rooms on the one side and laboratories on the other side, so that the nodes form a linear network with relatively favorable propagation without significant attenuation by walls. For comparison, the source and destination nodes, indicated by the red triangle and the blue square in Figure 52, are chosen to be the nodes at the two extreme ends of the linear network. The relay nodes, represented by the green circles, are placed with uniform spacing.

The carrier frequency is 2.482GHz, and the data rate is 64kbps. On of the four diversity

channels is assigned to each node as a repeating sequence (i.e.,  $\{A, B, C, D, A, B, C, D \dots\}$  from end to end). When multiple nodes assigned the same sub-channel belong to the same cooperation set and instantaneous received powers at a receiver are comparable to each other, the received signal suffers from self-fading within the sub-channel. However, frequency diversity and path loss disparity of each node can mitigate the performance degradation caused by self-fading.

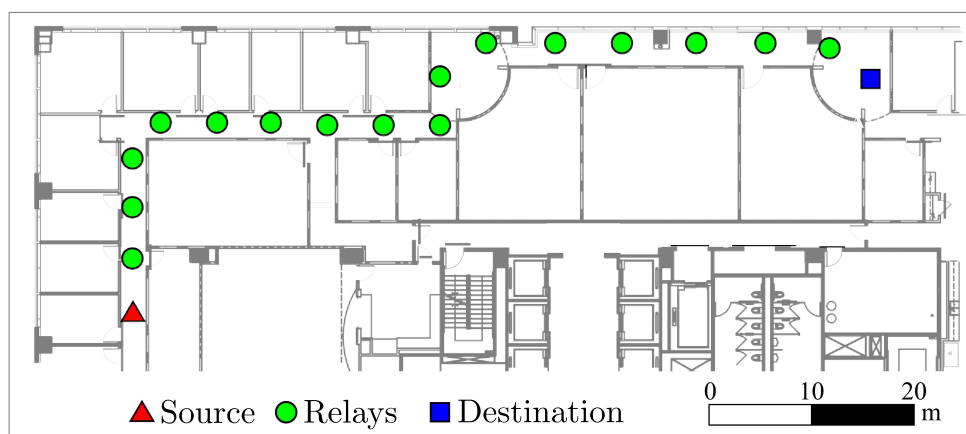


**Figure 52:** Network topology of the routing experiment.

The SISO network uses a single diversity channel, however, the bandwidth difference between the two networks does not have a big impact on the performance because the modulation scheme and the spectral efficiency in the experiment (0.5b/s/Hz) are classified to the power-limited regime [81]. The capacity linearly increases as the power increases in the power-limited regime, while the capacity is insensitive to bandwidth. Hence, each node has the same transmit power in the both SISO and CCT networks. The packet for the experiment is 128 bytes long consisting of 100 bytes of binary data, 26 bytes of data header, and two bytes of CRC.

Seven different transmit power levels are used from  $-18\text{dBm}$  to  $0\text{dBm}$  with intervals of  $3\text{dBm}$ . The increase in the transmit power makes the node degree of the network increase as shown in Figure 53, thereby decreasing hop count from the source to the destination. Also, the transmit power impacts the interference level in AODV, because all the nodes

send periodic beacons (HELLO messages).

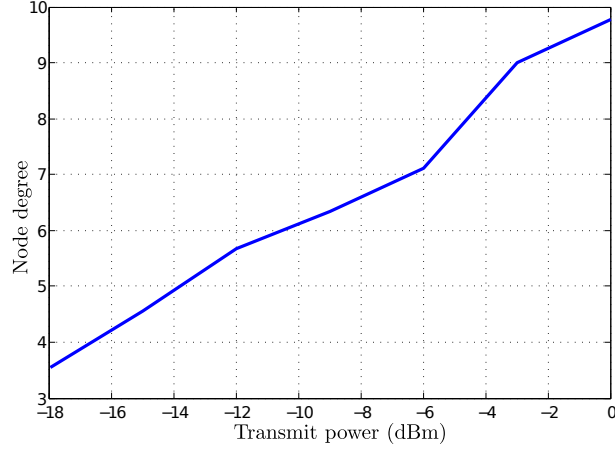


**Figure 53:** Node degree depending on transmit power levels.

#### 7.2.4.1 End-to-end Average Hop Count

The first experimental studies the delay performance in terms of the average hop count from the source to the destination. End-to-end latency is often approximated by the number of hops multiplied by the time spent on each hop, including processing, queuing, propagation, and transmission delays. The hop-count statistics, which are averaged over 100 runs of the 100 data packets transmission (the total number of transmitted packets=10,000=100×100), are shown in Figure 54. In the figure, the red and black curves represent the hop counts of AODV and OLAROAD, respectively. Also, the red and black “I-shape” error bars indicate the 95% confidence intervals of the statistical data. The hop counts of both AODV and OLAROAD decrease, as the transmit power increases. If comparing the two protocols, the hop counts of OLAROAD are always less than AODV. However, the difference is not as large as the expectation for CCT in Rayleigh fading channels, because the line of sight (LOS) channels in a corridor do not experience as significant fading as non-LOS channels, and the linear topology does not give enough node degree for OLAROAD to jump over many hops. In this setup, AODV also benefits the hop-count saving by finding the shortest path as the transmit power increases. Moreover, AODV has the link layer error control, where a node retransmits erroneous packets up to seven times in the implementation. This

retransmission is triggered by the timeout of the link layer ACK message from the desired receiver. Therefore, AODV is able to successfully send the data packets even though the shortest path is unstable.

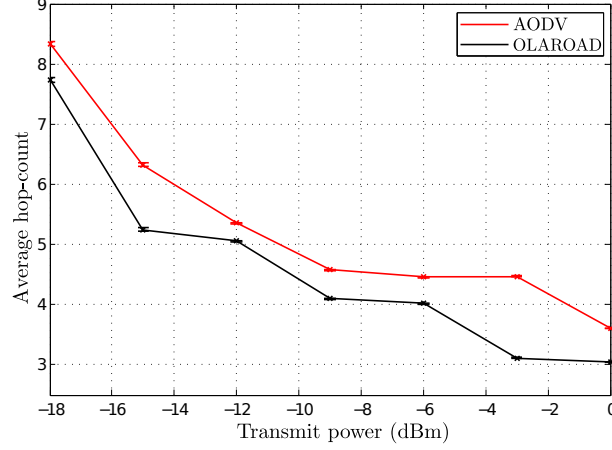


**Figure 54:** End-to-end hop count.

#### 7.2.4.2 Round Trip Time (RTT)

The second experiment is designed to measure the latency of the data transmission in terms of RTT. In this experiment, the source node first transmits a packet to the destination, then, after that packet has finally been received successfully, the destination generates another packet and sends the new packet back to the source. Therefore, the RTT is the time duration between the transmit time stamp of the first packet and the reception time stamp of the second packet, both of which are logged at the source node. After repeating this measurement process 100 times, the average RTT values are obtained as shown in Figure 55. In the figure, the RTTs of OLAROAD are about 1/3 of the AODV RTTs. Also, the confidence intervals of OLAROAD are much smaller than AODV, which implies that OLAROAD has a lower variance in RTTs than AODV. The first reason for the large difference in the average RTT values is the retransmission of AODV to repair the packet loss in the link layer. Considering the trade-off between latency and reliability in wireless networks, the latency such as RTT can be controlled by the error-control schemes such as

link layer retransmission. In the implementation of AODV, the maximum number of retries is seven. However, the number of retransmission can be reduced, if the application is latency-sensitive but error-tolerant such as voice or video transfer. Also, even though an ACK protocol for OLAROAD has been proposed, the ACK protocol is not implemented in this experiment, because of the high reliability of CCT in this network. Another reason for the large difference in RTT is the interference caused by the HELLO message in AODV, which makes the data transmission back off by CSMA/CA. However, this overhead caused by the interference is minimized by modifying the local route repair to be initiated only by the nodes in the data route. In other words, the nodes that are not in the data route, do not send an RREQ even when they lose one of the neighbors by expiration.

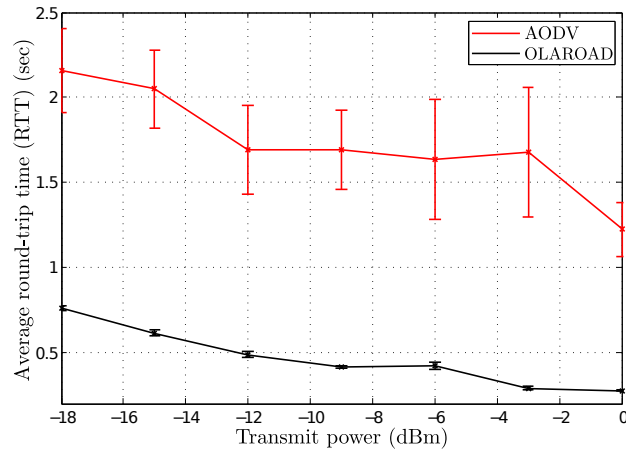


**Figure 55:** End-to-end round trip time (RTT).

#### 7.2.4.3 Packet Delivery Ratio (PDR)

Because PDR is an important performance metric for reliability evaluation, the corresponding measurement is designed to show the end-to-end PDR over 100 data packets sent from the source to the destination. To achieve a certain level of statistical significance, this PDR measurement with 100 packets is repeated 100 times. The results of the PDR measurement are shown in Figure 56. In the figure, OLAROAD performs better than AODV with the transmit power from  $-12\text{dBm}$  to  $0\text{dBm}$ . However, in the poor wireless link condition with the lower transmit powers ( $-18\text{dBm}$  and  $-15\text{dBm}$ ), the PDRs of AODV are higher than or

similar to OLAROAD.

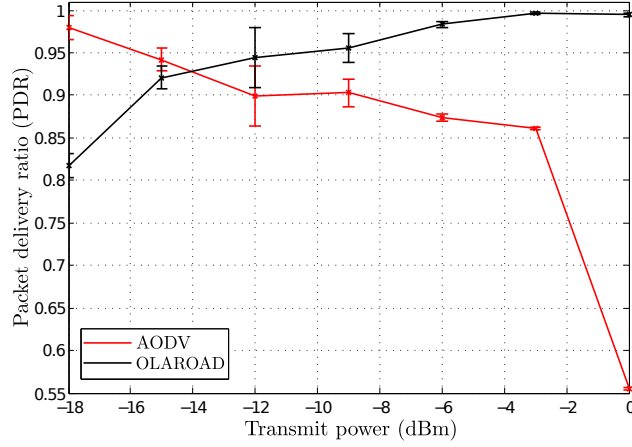


**Figure 56:** Packet delivery ratio (PDR).

Considering cooperative diversity, this might seem surprising, however, the result is reasonable based on the low node degree and the link layer error control of AODV. With the transmit power of  $-18\text{dBm}$ , the route built by OLAROAD is actually similar to the route made by AODV, because the node degree is too low to gather many cooperators. As the average hop count of the AODV and OLAROAD routes at  $-18\text{dBm}$  transmit power are about 8.5 and 8.0, respectively in Figure 54, the maximum number of cooperators on each hop on average in the cooperative route of OLAROAD is just about two. However, in fact, the number can be less than two if some nodes cannot decode. Also, as previously stated, AODV has the data link layer error control, while OLAROAD does not. Therefore, this result suggests the need of error detection and repair in the link layer independent from the end-to-end error control, even though it is challenging to design because of the asymmetry in CT-based link connections. As the transmit power increases, OLAROAD shows better PDR, while the PDR of AODV decreases. One reason for this performance degradation in AODV is the HELLO messages cause increasing interference on the data packets. Also, AODV builds the shortest route regardless of the link quality, which results in frequent re-routing and retransmissions.

#### 7.2.4.4 Route Discovery Time

The route discovery time, which is a key performance metric for reactive (on-demand) routing protocols, is the latency to discover a route for a given source and destination pair. This latency impacts the data rate, because the data packets are buffered until the route is built. In AODV, the discovery time is the time from the first RREQ transmission to the first reception RREP that does not necessarily correspond to the first RREQ. In other words, if the source cannot receive the RREP corresponding to the first RREQ, but receives the RREP for the second RREQ trial, then the route discovery delay would be the time between the first RREQ transmission and the RREP (for the second RREQ) reception. Similarly, the route discovery time of OLAROAD is the time between the first RREQ transmission and the first RCACK reception. In this way, the route discovery time is calculated by 100 repeated experiments. In Figure 57, the *median* values are presented that obtained over 100 trials, because route failure (infinite delay) happened sometimes. For the same reason, the confidence intervals are not available. The results in Figure 57 indicate that AODV takes less time to finish the routing than OLAROAD except the transmit power of  $-18\text{dBm}$ , since OLAROAD has two stages of end-to-end handshake process. The reason why AODV gives the poor performance at  $-18\text{dBm}$  is the unstable link condition, where the unicast of RREP requires many retransmissions.

Because of the two handshakes, OLAROAD has a longer route discovery time than AODV. If the nodes have small buffers, the large discovery time of OLAROAD might cause the buffer overflows. From an overhead perspective, the cost of OLAROAD's extra handshake will diminish if a large number of packets are sent along the route.

### 7.3 Summary

The first part of this chapter presents experimental directional coverage extension by CCT in terms of average PERs in a typical modern office environment. Three relay topologies

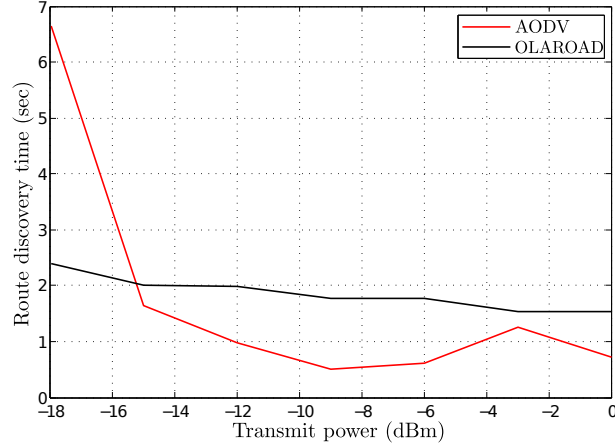


**Figure 57:** Route discovery time.

are distinguished by the presence or absence of the features: disparate path loss to the destination, micro diversity, and macro diversity. It has been shown that the widely dispersed topology is effective to maximize the coverage area while the medium cluster is best for the directional range extension. The measured data matched well the 1% outage contour, but had a poor match to the 10% outage contour. The overall conclusion is that CCT is an effective and practical way to extend range and coverage area in an indoor environment.

In the second part of the chapter, we demonstrate a CT-based routing scheme, OLAROAD, in comparison with the widely used on-demand routing protocol, AODV, on a linear network in a typical indoor environment. For a realistic evaluation, the protocols were implemented on a testbed using GNU Radio and USRP1 software defined radio. We provide the details of the challenge in CT-based routing, and the system structure of the physical, MAC, and network (routing) layers for the implementation of OLAROAD and AODV. The experimental results show that OLAROAD improves the most of the performance metrics considered except the route discovery time. Moreover, OLAROAD shows the poor reliability performance (PDR) compared to AODV in low node degree situation.



## CHAPTER 8

### OLA-BASED ROUTING AND ERROR CONTROL

In this chapter, we introduce the unicast routing scheme, OLA with primary route set-up (OLA-PRISE), which is more efficient than OLAROAD in terms of numbers of nodes participating. OLA-PRISE uses conventional non-CT (or SISO) transmission for route set-up, but uses OLA transmission for data transmission for data packet transmission.

#### 8.1 Comparison Cases

We will compare OLA-PRISE with two other CT-based routing methods: non-OLA-based routing with a primary route (FM-PR) and the all-OLA routing scheme without a primary route (OLAROAD), which were described in Section 2.4. A summary of the three methods is shown in Table 7. The first method, FM-PR, is identical to the schemes in [1, 42, 55], where the number of nodes in each cluster is constant for multiple packets. The second method, OLA-PRISE, is a new scheme that uses the SISO primary-route nodes and their one-hop neighbors for route set-up, but uses OLAs for data transmission. The last method, OLAROAD, is the all-OLA routing scheme without a primary route described in [35, 77] and Section 2.4. We are mainly interested in the two OLA-based routing methods, OLA-PRISE and OLAROAD, because FM-PR cannot fully benefit from wireless broadcast advantage because of its fixed membership and that reception is solely by a single node (cluster head) in a cluster.

#### 8.2 Example Routes of OLA-PRISE and OLAROAD

In this section, we show example routes through MATLAB simulation to explain OLA-PRISE and compare it to OLAROAD. In the simulation, we assume a  $300 \times 300$  square network, where 2000 nodes are uniformly and randomly distributed. Also, we assume Rayleigh multi-path fading with path-loss exponent  $\alpha = 4$ . The transmit SNR, TSNR is

**Table 7:** Three CT-based Routing Algorithms

Routing Methods	Properties
FM-PR	<ul style="list-style-type: none"> <li>• SISO primary routing in the initial phase</li> <li>• <i>Some selected</i> one-hop neighbors of the nodes in the primary route join the final CT-route</li> <li>• Single cluster head (single receiver in each VMISO hop)</li> <li>• Fixed membership</li> </ul>
OLA-PRISE	<ul style="list-style-type: none"> <li>• SISO primary routing in the initial phase</li> <li>• <i>All</i> one-hop neighbors of the nodes in the primary route join the final CT-route</li> <li>• OLA transmission in the data transmission phase</li> </ul>
OLAROAD	<ul style="list-style-type: none"> <li>• SISO primary routing in the initial phase</li> <li>• All-OLA routing scheme without a SISO primary route</li> <li>• OLA transmission in the data transmission phase</li> </ul>

such that the received SNR at the reference distance is 40dB, while the decoding threshold is set at  $\tau = -1\text{dB}$ . Figure 58 shows the network topology of the simulation example, where the yellow triangle at the lower left corner indicates the source, while the yellow square at the upper right corner is the destination. Also, the black circles indicate the nodes that are not in the route. The 22 solid red circles connected by the red line are the SISO primary-route nodes, corresponding to 23 hops from the source to the destination. In FM-PR in Table 7, the nodes in this primary route will collect their cooperators, the numbers of which are the same in each hop. Different from OLA-PRISE and OLAROAD, FM-PR has a single designated receiver, which is the next-hop primary-route node, in each hop. By the CT range extension, FM-PR can hop over some relays in the SISO primary route and reduce the end-to-end hop-count.

In OLA-PRISE, the SISO primary route, which is indicated by the red circles connected by the red line, is first constructed as in FM-PR. In FM-PR, some primary-route nodes are used as a cluster head that exclusively decodes following the centralized CT architecture described in Section 2.2. The blue circles in the figure represent the one-hop neighbors

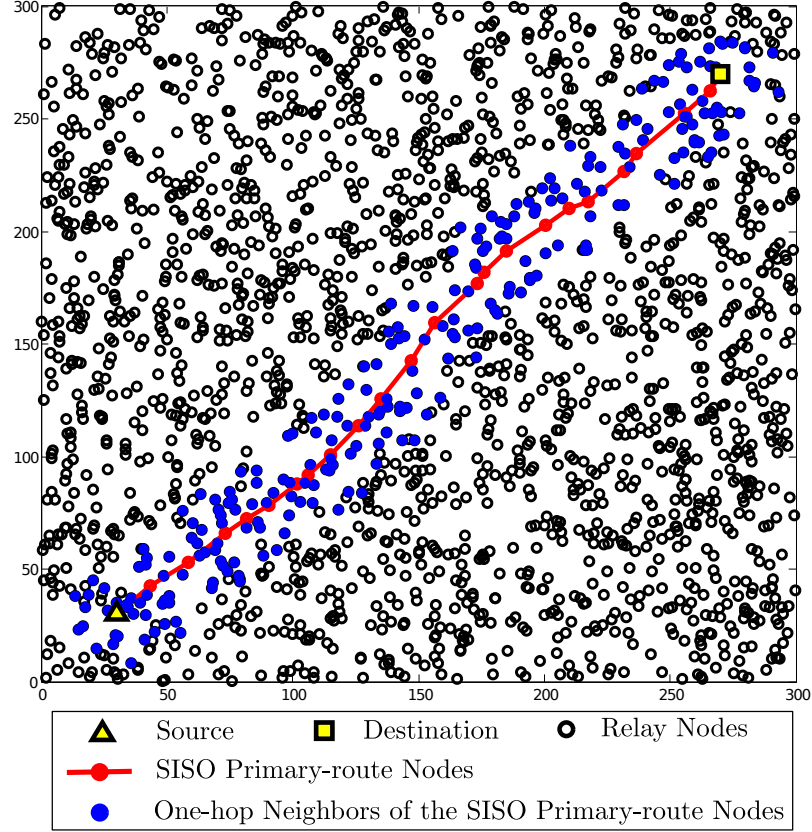


**Figure 58:** Route examples of SISO-based scheme and OLA-PRISE.

of the primary-route nodes. These one-hop neighbors do CT with the primary-route nodes both in FM-PR and OLA-PRISE. The union of the red and blue circles is the cooperative route for data transmission with OLAs in OLA-PRISE, where all the nodes in this collection have the same role. In contrast, FM-PR uses a subset of the nodes used in OLA-PRISE to keep a fixed number of cooperators in each hop to minimize link asymmetry. Moreover, FM-PR has a deterministic hop count, because only the cluster heads decode the data packet. On the other hand, because OLA-PRISE uses OLA transmission in the data transmission phase after the route is constructed, the membership (OLA level) of OLA-PRISE is determined on the fly, which means the membership can change for different packets.

The last method in Table 7, OLAROAD, has the route indicated by the blue circles in Figure 59. Because of its ring expansion in the RREQ transmission through OLA broadcasts, which is described in Section 3.3, the resulting route of OLAROAD uses excessively

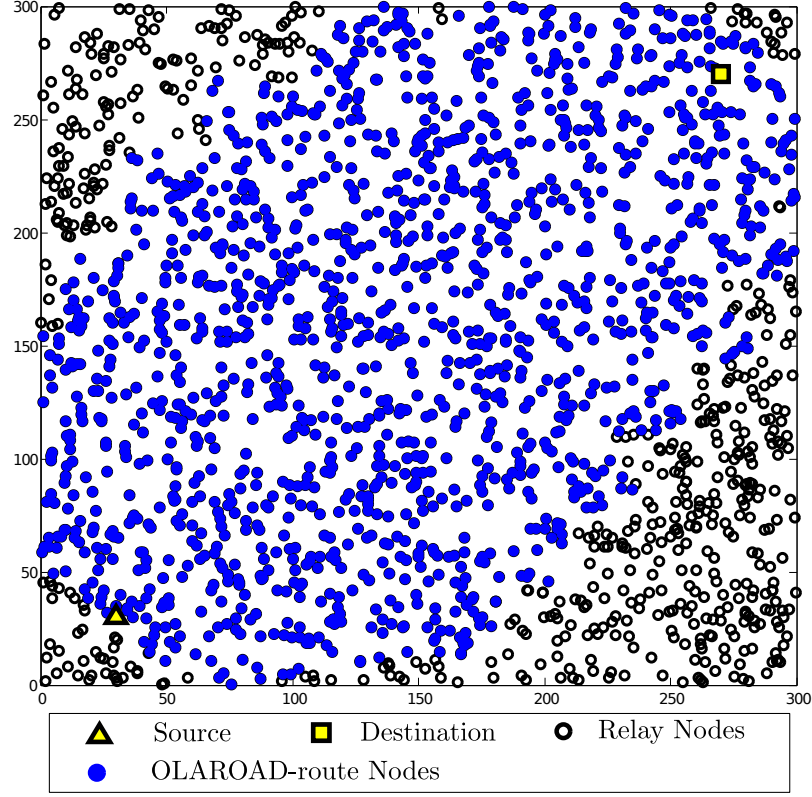


Figure 59: OLAROAD route example.

many nodes, where all the nodes have the same role. Moreover, the ring-expansion of OLAROAD might create voids in the middle of the route in higher node degree as shown in Figure 51. In [5], various solutions to the ring expansion problem are proposed, such as ganging of levels in the upstream, power control of the source, and step-size control. However, these solutions are difficult to implement in practice, because they require topology information or uniform node distribution assumption. In other words, the proposed solutions work only for (randomly but) uniformly distributed networks. Also, the proposed power control schemes are proposed based on a certain path-loss exponent without considering fading channels.

Compared to OLAROAD, OLA-PRISE provides a more efficient route in high node density situation as in the example case. In other words, OLA-PRISE makes a strip-shaped route, which is an idealized version of CT route, while OLAROAD suffers from excessive node participation. Also, OLA-PRISE produces a more controlled shape of the route, while

the shape of route constructed by OLAROAD is hard to predict as a function of different system parameters such as node degree, and the participation condition determined by the uplink and downlink levels of a node. However, OLAROAD can overcome the network partition problem by higher range extension, while the SISO primary route may detour the partitions.

### **8.3 Issues in Link-level MAC and ARQ for OLA-based Routing**

As discussed in Section 2.4, link-layer MAC and ARQ are used in cooperative schemes that have cluster heads, and end-to-end (or path)-based MAC and ARQ are cooperative schemes that do not use cluster heads (i.e., OLA-based schemes). In this section, we discuss why link-layer ARQ and the corresponding link-layer MAC are difficult to implement for OLA-based protocols, which are our main interest, because of the limited broadcast advantage in FM-PR.

#### **8.3.1 Uncertainty in Link Definition**

The existing algorithms using FM-PR routing can operate link-level MAC and ARQ, because of its fixed hop-count membership and the existence of the cluster head in each cluster. On the other hand, the CT routing methods in Sections 2.4.2.3 and 2.4.2.2, which allow flexible hop-count membership (i.e., a hop-count of a node is determined on the fly), do not use link-level MAC and ARQ. Similarly, the two OLA-based routing methods have uncertainty in cluster membership, which makes difficult the definition of an *error* in terms of the number of nodes that fail to successfully decode the received packet.

#### **8.3.2 Cluster-level Decision**

For link-level MAC and ARQ, cluster-level consensus should be made about 1) whether the packet will be retransmitted or not, based on a feedback signal and 2) when to access the channel, if the nodes in the cluster either forward or retransmit a packet. To reach the consensus, there can be two cluster architectures: centralized cluster or non-centralized

cluster. Relatively, the centralized cluster achieves consensus more easily compared to the non-centralized case. A related issue is that, in the OLA-based routing methods, cluster head election is another consensus problem. Also, the cluster head election might need to be repeated for each packet, because the OLA level changes randomly for different packets.

This cluster-level consensus is important for contention-based MAC such as CSMA/CA, because multiple nodes in the CT group might have different sensing ranges. Also, not to recognize the group transmission from a cooperator, highly precise network time synchronization (NTS) is required in the contention-based MAC. Therefore, contention-free MAC (e.g., FDMA and TDMA) is more appropriate for the OLA-based routing methods. We consider the periodic packet transmission with the transmit time synchronization in [54] based on the packet reception from the previous hop, which makes TDMA-like MAC without any external device for NTS.

### **8.3.3 Link Asymmetry**

For link-level MAC and ARQ, link symmetry (or bidirectionality) between neighbor clusters is required, because of the feedback signal (e.g., acknowledgement) in the reverse path after the data transmission in the forward direction. In OLA-PRISE and OLAROAD, link symmetry is hard to achieve, because cooperative clusters have different numbers of nodes and the VMISO channel gains are different. Considering the link asymmetry is also severe even for FM-PR with the fixed number of nodes in each cluster in Section 6.2, link symmetry is extremely difficult to achieve in the OLA-based schemes.

## **8.4 Proposed Algorithms**

In experimental results in Section 7.2.4.3, the packet delivery ratio of OLAROAD is worse than AODV for low transmit power, while OLAROAD outperforms AODV with high transmit power. That is because the node degree is very low for OLAROAD to gather enough number of cooperators, when the transmit power is low. Therefore, the route of OLAROAD is not much different from the one built by AODV with low transmit power. Moreover,

AODV has the link-level ARQ that triggers retransmission up to seven times to overcome frequent transmission errors caused by low transmit power. However, as stated in the previous section, the link-layer MAC and ARQ are difficult to implement in OLA-based unicasting. Therefore, instead of impractical link-layer MAC and ARQ for the two OLA-based schemes, we propose selective routing protocol operation depending on the node degree and local ganging, which are covered in the following sections.

#### **8.4.1 Routing Operation based on Node Degree**

The routing scheme should be selected depending on the network conditions. For example, the routes constructed by CT and primary SISO routing schemes are almost identical in low node degree. Thus, in this case, SISO routing is better to use considering its link-layer error control. On the other hand, when node degree is high enough to recruit many cooperators, OLA-based routing does not need the link-layer error control, because the transmission errors are very unlikely because of the array and diversity gains as shown in Section 7.2.4.3. The routing selection also depends on the traffic condition and latency requirement. For example, OLAROAD usually uses a significantly larger number of nodes than other CT routing methods and the conventional SISO routing, which saves the end-to-end latency but causes high interference to other flows. Thus, CT-based schemes are appropriate for latency-sensitive applications or large file transfer. Moreover, the two OLA-based routing methods (OLA-PRISE and OLAROAD) will use end-to-end error control except the local ganging technique, which will be introduced in Section 8.4.2.

In this context, the main question is how to identify and reflect the node-degree information into the routing selection. We propose to use local beacon signals such as HELLO message in AODV so that each node can identify its local node degree. As the flow chart in Figure 60, all the nodes identify the number of their one-hop neighbors. Then, the protocol first tries to find a SISO primary route. If the primary route is not available because of network partitions, OLAROAD will be triggered when the source can collect enough number of cooperators. On the other hand, if the SISO primary route exists, the protocol will test

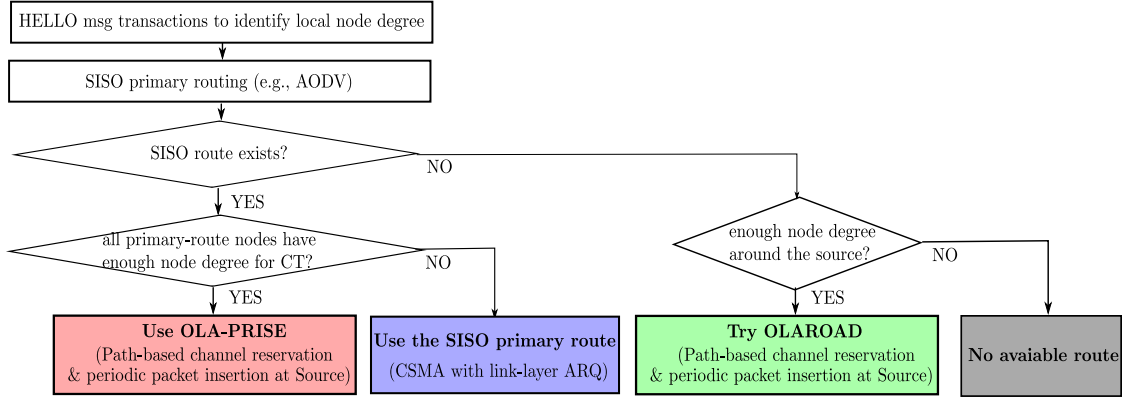


**Figure 60:** Flow chart of routing selection

if all the primary-route nodes have enough number of one-hop neighbors to use as cooperators. The source can obtain this information by serialized fields inserted in RREP at each hop from the destination back to source. If at least one of the primary-route nodes does not have enough node degree for CT, which means the OLA- and SISO-based routes are not much different, the SISO primary route (e.g., AODV) will be used with CSMA/CA and its link-layer ARQ. If all the primary-route nodes can collect enough number of cooperators, the protocol will trigger OLA-PRISE. Also, OLA-PRISE will operate under path-based channel reservation, which is suitable for data burst application, with periodic packet insertion at the source. If an error control algorithm is required, we will use the end-to-end error control or let TCP handle the error.

In this proposed algorithm, we do not consider FM-PR, because OLA-PRISE and OLAROAD can benefit from reception diversity by its opportunistic feature and multiple receivers. In other words, for high enough node degree, OLA-PRISE and OLAROAD can perform better, because FM-PR only has a single desired receiver (cluster head) in each hop. Moreover, OLA-PRISE has higher priority than OLAROAD in the proposed routing selection in Figure 60, since OLA-PRISE can guarantee more efficient routing, while OLAROAD is difficult to adapt the shape of the route or the number of the nodes participating in routing.



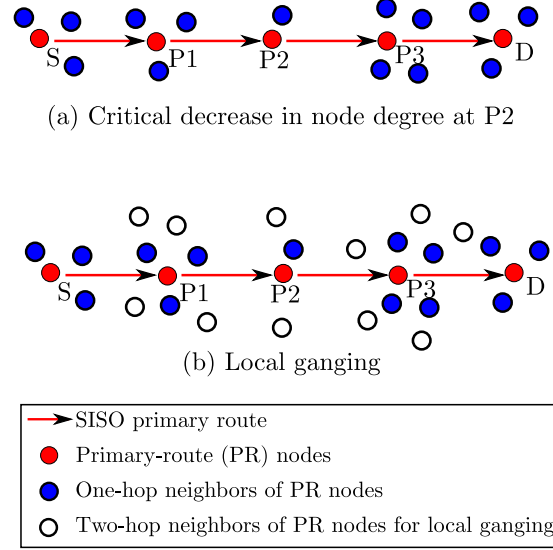


**Figure 61:** Illustration of local ganging for OLA-PRISE

#### 8.4.2 Local Ganging in OLA-PRISE

In this section, we consider a local link repair technique, local ganging, which is designed for OLA-PRISE to overcome frequent transmission errors in low-node degree hops. The main purpose of local ganging is to improve the quality of the route by using more number of nodes before the data transmission, by collecting more cooperators in intermediate hops with low node degree as shown in Figure 61.

In the figure, the red circles indicate the SISO primary-route nodes (the source labeled with S, and intermediate-hop nodes from P1 to P3, and the destination labeled with D). In OLA-PRISE the one-hop neighbors of the primary-route nodes, which are indicated by the blue circles in Figure 61, are used for the cooperative transmission. However, in the figure, P2 has only one cooperator, while the other primary-route nodes have more number of neighbors. In this case, the group transmission around the P2 may fail frequently. As a result, the end-to-end packet delivery is low.

Therefore, by the node degree identification of the primary-route nodes as suggested in the previous section, we can repair the OLA-PRISE route before the actual data transmission as shown in Figure 61 (b). With the local ganging technique, the three consecutive primary-route nodes P1-P2-P3 recruit more nodes (two-hop neighbors) to fix the critical

link-quality drop at P2. The recruit message for this local ganging is created and broadcasted by the three primary-route nodes (using multiple hops with a time-to-live field of two) that already know that the node degree of P2 is significantly lower than the average of the other primary-route nodes, by the two-way end-to-end handshake with RREQ and RREP in the SISO primary route construction.

## 8.5 Simulation Results

In this section, we compare four routing protocols: SISO-based routing, two OLA-PRISE algorithms (with and without local ganging), and OLAROAD. To be specific, there are two OLA-PRISE schemes in the simulation: the original OLA-PRISE without local ganging and OLA-PRISE with local ganging. We note that the threshold of the one-hop neighbors to activate the local ganging is four. In other words, if Hop  $k$  has its one-hop neighbors smaller than four, the primary route nodes in Hops  $k - 1$ ,  $k$ , and  $k + 1$  will collect all of their two-hop neighbors. The four routing methods are evaluated using three different performance metrics for a single flow: average throughput, end-to-end latency, which indicates the number of transmissions from the source to the destination, and the number of nodes in the route.

### 8.5.1 System Model

As in Section 8.2, we assume path-loss exponent  $\alpha = 4$  with Rayleigh fading channel. Also, we use three transmit SNR levels as  $P = 40, 42.5$ , and  $45\text{dB}$ . Moreover, for more realistic simulation, we consider the gray zone effect in [82], which implies data transmission errors caused by the decoding range difference between the data and routing control packets. To be specific, data packets with longer length or higher modulation rate are more likely to be lost than control packets with shorter length or lower modulation rate. Therefore, the routing control packets (e.g., RREQ, RREP, and HELLO message in AODV) may have larger transmission ranges than the data packet, which is a longer packet and modulated with a higher rate. Thus, we have two different decoding threshold  $\tau = 0\text{dB}$  for the

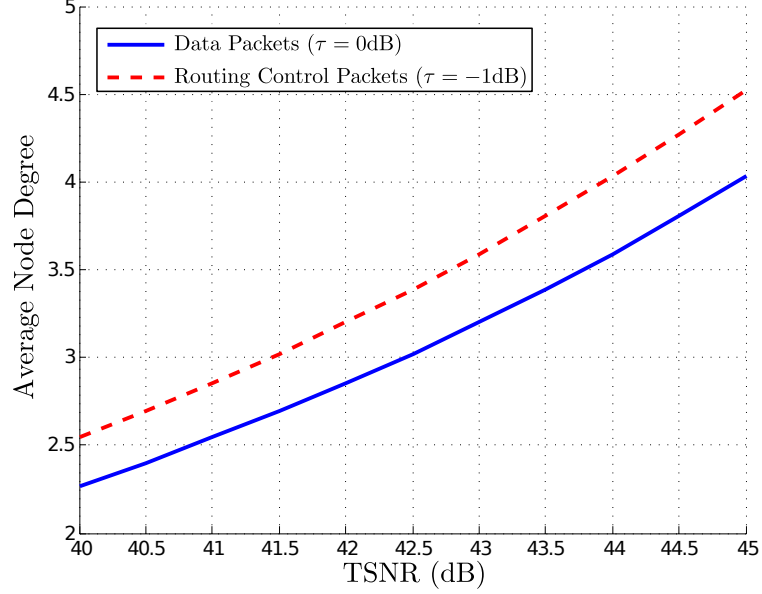


**Figure 62:** Average node degree  $\kappa$

data packets and  $\tau = -1\text{dB}$  for the routing control packets. In other words, the routing control packet has a longer transmission range than the data packets by the 1dB decoding threshold difference. We note that we assume this decoding threshold difference to make our simulation reflect the gray zone effect, but the 1dB is much lower than the extreme case shown through the simulation results of the IEEE 802.11 implementation on QualNet in [82].

We assume a  $300 \times 300$  square network, where 2000 nodes are uniformly and randomly distributed. Figure 62 shows the average node degrees for data packets and routing control packets. In the figure, the y-axis indicates the average node degree, while the x-axis indicates the transmit SNR, TSNR. Also, the blue solid line and red dotted line represent the node degrees  $\kappa$  with  $\tau = 0$  and  $-1\text{dB}$  for the data and routing control packets, respectively. The node degree  $\kappa$  in the figure is calculated by the average number of nodes with the outage rate less than or equal to 0.1 assuming Rayleigh fading channel. Comparing the two curves, at the same TSNR, the node degree based on the data packets is always lower than the node degree defined by the routing control packets, because the decoding requirement of the data packets ( $\tau = 0\text{dB}$ ) is more demanding than the routing control packets

( $\tau = -1\text{dB}$ ). Also, the two graphs increase, as TSNR increases, because the transmission range of a node increases, as the transmit power increases.

We note that because  $\kappa$  in Figure 62 includes both neighboring nodes and the node itself, it is very challenging to build a SISO primary route with low TSNR in the graph (e.g., TSNR=40dB). Furthermore, the gap between the two curves, which implies the degree of the gray zone effect in [82], increases, as TSNR increases.

Moreover, we consider the intra-flow interference with packet insertion period  $M = 3$  for OLA-PRISE and OLAROAD. In other words, the source sends a new packet every  $M = 3$  time slots. Because  $\alpha = 4$ , the spatial reuse in the multi-packet transmissions is high enough to support  $M = 3$ . We note that a lower path-loss exponent (e.g.,  $\alpha = 2$  or 3) require a longer packet insertion period  $M$ , as shown in our previous multi-packet OLA transmission studies in Chapters 4 and 5. On the other hand, we assume interference-free simulation for the SISO-based routing, because CSMA/CA, which is difficult to model in the simulation, can deal with the collision caused by the intra-flow interference. Also, we assume link-level retransmission up to seven times with new fading realizations for each try in the SISO-based routing.

### 8.5.2 Simulation Results

Figures 63, 64, and 65 show the simulation results with 100 iterations of 100 data packet transmissions over a random i.i.d. Rayleigh fading realization for each packet. In each figure, the horizontal axis indicates TSNR from 40dB to 45dB with 2.5dB interval and the vertical axis indicates end-to-end latency (E2E hop-count)  $L$ , average throughput  $\eta$ , and average number of nodes in the route  $N_{\text{node}}$ , respectively. Also, at each TSNR, there are four bar graphs with different colors corresponding to the SISO-based scheme (black), OLA-PRISE (dark-gray), OLA-PRISE with local ganging (light-gray), and OLAROAD (white), respectively.

In Figure 63, the end-to-end latency  $L$ , which means the number of transmissions from the source to the destination including retransmission, of the SISO-based scheme is much

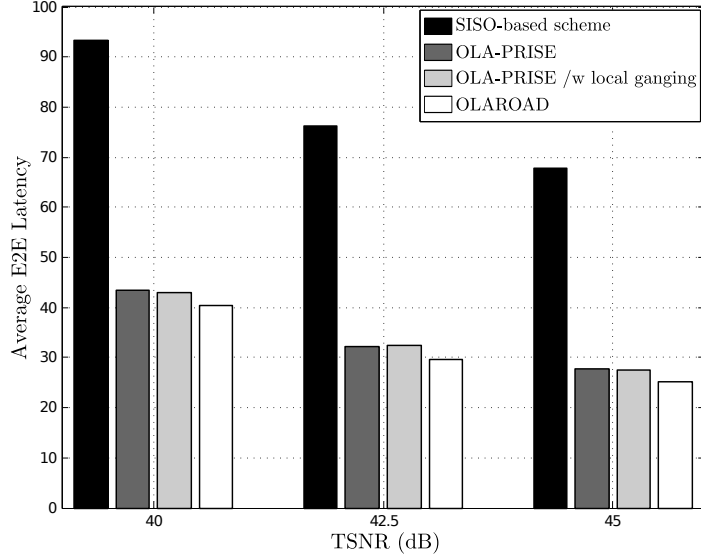


**Figure 63:** Average end-to-end latency  $L$

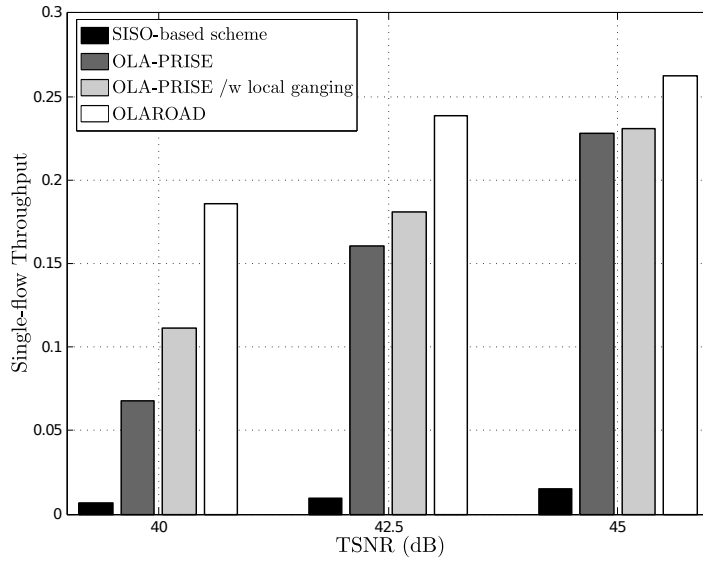


**Figure 64:** Average throughput  $\eta$

higher than the three CT-based schemes. As TSNR increases,  $L$  of the four scheme decreases, because of hop-count saving by the increased transmission range. For the SISO-based scheme, even though the number of nodes in the SISO-based route is relatively small (e.g., 23 hops with TSNR=40dB in Figure 58), the latency including retransmission, which can happen up to seven times for each hop, is significantly greater. On the other hand, the three CT-based schemes show almost the same latencies, which are about 50% of the

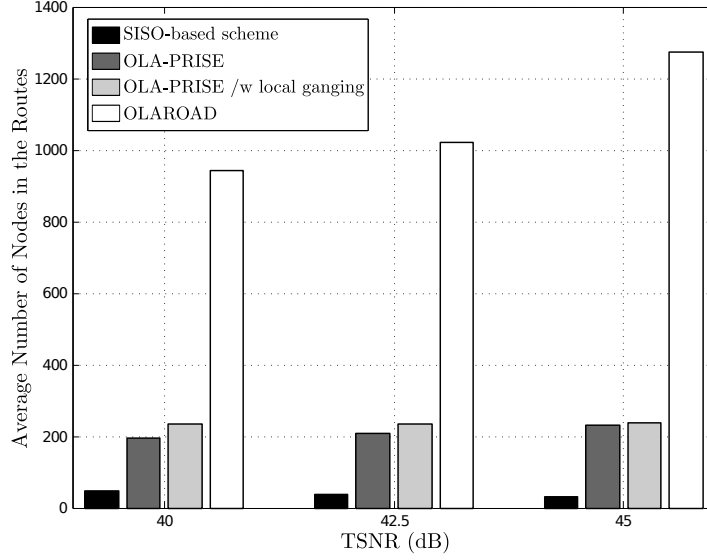


**Figure 65:** Average number of nodes in route  $N_{\text{node}}$

latency in the SISO-based scheme, because the three CT-based algorithm exploit the range extension through array and diversity gains.

Figure 64 shows the average single-flow throughput  $\eta$  of the four algorithms. First, the SISO-based routing shows the worst throughput, because SISO links are unstable with the given transmission range in the presence of random Rayleigh fading. On the other hand, OLAROAD shows the best (highest) throughput  $\eta$ , because the route is much wider with a larger number of nodes than the other three algorithms. The second best algorithm is OLA-PRISE with local ganging, and the original OLA-PRISE without local ganging shows lower throughput  $\eta$  than OLA-PRISE with local ganging. The difference in  $\eta$  of the two OLA-PRISE schemes decreases, as TSNR increases. In other words, with higher transmit SNR (e.g., TSNR=45), the local ganging technique does not help the throughput improvement much, because the primary-route nodes have enough number of one-hop neighbors, the threshold of which for triggering local ganging is four with high TSNR.

The average numbers of nodes used in the route are shown in Figure 65, which is proportional to energy consumption and possible interference to the other flows in the network. As we expect, OLAROAD uses the largest number of nodes. Interestingly, as TSNR

increases, only the number of nodes used in the SISO-based scheme decreases, while it increases in the three CT-based schemes. That is because the SISO-based route takes smaller hops to reach the destination by the transmission range increase. On the other hand, in the three OLA-based schemes, more cooperators are collected by the transmission range extension. Comparing the heights of the bar graphs, OLAROAD shows the largest number of nodes in the route. Especially, at TSNR=45dB, OLAROAD uses about 65% of the entire network, considering the total number of nodes in the network is 2000, while about 1300 nodes are used in OLAROAD. Also, the two OLA-PRISE schemes show the decreasing gap, as TSNR increases, which means local ganging is not triggered frequently at the higher transmit powers with the large enough node degree.

## 8.6 Summary

In this chapter, we present the existing CT-based routing protocols and error control algorithms. We specify three different CT-based routing methods: FM-PR, OLA-PRISE, and OLAROAD. The OLA-based routing scheme, OLA-PRISE, can be a good solution to overcome the limited broadcast advantage in FM-PR and difficult shaping control of OLAROAD. Also, we specify the possible issues to develop link-level ARQ and MAC such as uncertainty in link definition, cluster-level decision, and link asymmetry. Therefore, the path-based ARQ and MAC are more desirable for OLA-based routing. Also, we propose selective routing operation depending the node degree and local ganging for OLA-PRISE to improve the quality of the OLA-based routing. The simulation results show that the performances of the SISO-based routing, OLA-PRISE, OLA-PRISE with local ganging, and OLAROAD in terms of the average end-to-end latency  $L$ , average throughput  $\eta$ , and average number of nodes in the route  $N_{\text{node}}$ . Compared to the SISO-based schemes, the OLA-based methods provide better  $L$  and  $\eta$ . However, the OLA-based schemes (especially OLAROAD) use significantly more number of nodes for unicasting. Therefore, considering the interference increased by the large size of the routes, OLA-based schemes

are more appropriate in light traffic scenarios that require high single-flow throughput, for example infrequent large file transfer, and that require high reliability. Moreover, the proposed route repair, local ganging, in OLA-PRISE can improve throughput in the low node degree situation with low transmit power.



## **CHAPTER 9**

### **CONCLUSION AND SUGGESTED FUTURE WORKS**

Cooperative transmission (CT) is an effective communication technique to improve link and route performance. The signal-to-noise-ratio (SNR) advantage can be used to enhance reliability, latency, and energy efficiency. In wireless multi-hop networks with power and hardware limitations, where conventional multi-antenna arrays cannot be deployed, CT is an alternative way to achieve spatial diversity in fading channels. Moreover, compared to the conventional multi-antenna array, the distributed multi-antenna array created by CT can provide better diversity gain, because of macro-diversity with widely spread cooperative nodes. However, the network-scale protocol design based on CT still needs much more development with realistic evaluation.

In this dissertation, we focus on one type of CT known as concurrent cooperative transmission (CCT), where cooperating nodes transmit multiple copies of the same message at approximately the same time through orthogonal channels, and a receiver achieves a signal-to-noise-ratio (SNR) advantage by combining the copies of the signals. To be specific, we consider a simple CCT strategy called Opportunistic Large Arrays (OLAs), where groups of relays are formed without coordination by each relay's successful decoding of a message from a single source or another OLA.

The main contribution of this dissertation is to clarify and examine important characteristics of CCT and OLA through analysis and experimentation. This doctoral research is aimed to elicit better understanding of CCT in the context of cooperative multi-hop networks.

One contribution of this research is the optimization of multi-packet OLA transmission in presence of the intra-flow interference caused by multiple co-channel packets. While most of the previous studies on OLA only consider single-packet transmission case, which

fully exploits the CT range extension without any degradation by the co-channel interference, we analyze OLA broadcasting and unicasting along disk- and strip-shaped networks assuming multiple packets are transmitted within a single flow (e.g., large file transfers). To be specific, we optimize throughput by spatial pipelining, which implies multiple packets are propagating across the network at the same time using the same channel with certain inter-separations, depending on network shape, path loss exponent, transmit power, and other system parameters. Also, we analyze the feasibility of spatial pipelining in extremely large networks and provide numerical results showing impacts of various system parameters.

The second contribution in this doctoral research is CCT link modeling for more realistic protocol design and evaluation. In multi-hop ad hoc network, CT-based protocols are classified into two architectures: centralized architecture with a cluster head in each CT cluster and decentralized architecture with equal-role cooperators as in OLA. Assuming the centralized CT architecture, we consider two significant issues: path-loss disparity and link asymmetry. In the literature, multiple distributed nodes that create a CT cluster together are frequently approximated by a single node with multiple antennas for simplicity. We identify the impact of path-loss disparity ignored by this co-located approximation and quantify the SNR gap (i.e., error) in outage probability calculation. Moreover, we show that CCT links suffer from the more significant difference between the forward and reverse link performance than non-CT or SISO-based links. The results in our CCT link modeling should sensitize designers of CT-based higher-layer protocols in multi-hop networks.

Moreover, we demonstrate CCT range extension and OLA-based routing using a software-defined radio (SDR) testbed. First, we show the two-hop CCT measurement that provides the range extension ratio of CCT compared to non-CT in a realistic indoor environment. Three relay topologies, which have distinct features (e.g., path-disparity, micro-diversity, and macro-diversity), are compared in terms of directional range and coverage area. The

overall conclusion is that CCT is an effective and practical way to extend range and coverage area in an indoor environment. The second experiment, we compare the OLA-based routing scheme called OLAROAD with the widely used non-CT routing protocol, AODV. The experimental results show that OLAROAD improves the most of the performance metrics considered except the route discovery time. Moreover, OLAROAD shows the poor reliability performance (PDR) compared to AODV in low node degree situation because of the lack of the error control algorithm.

Lastly, inspired by our experimental results, we develop an efficient OLA-based routing protocol to build a multi-hop path for unicasting between a random source and destination pair. Moreover, we specify possible issues in implementation of an error control algorithm and medium access control (MAC) for OLA-based routing. As a solution, we propose selective routing operation depending the node degree and local ganging for OLA-PRISE to improve the quality of the OLA-based routing. Through simulation, we show that OLA-PRISE with local ganging can significantly improve latency and throughput from non-CT routing protocol, using a smaller number of nodes than OLAROAD, while the performance is still comparable.

The following is a list of possible directions for future research.

1. This dissertation has considered only single-flow performance. Multi-flow analysis should be conducted. Because OLA-PRISE is expected to enhance multi-flow throughput, the protocol overlay that decides between OLAROAD and OLA-PRISE may need to consider additional information relative to network throughput.
2. Multi-packet OLA transmission has been optimized using continuum and deterministic channel assumptions, which is accurate for high density networks with a large number of diversity channels. Thus, a mathematical model for low node density and low diversity order scenarios might lead to an efficient multi-packet transmission strategy for a broader scope of OLA broadcasting and unicasting applications. This will require a new framework different from the continuum assumption to capture

the randomness in node distribution with low enough computational complexity.

3. Because the path-loss disparity analysis in this dissertation only assumes path loss and Rayleigh multi-path fading, different channel models can be considered in the future. For example, the variation of SNR penalty caused by path-loss disparity in log-normal shadowing and Ricean multi-path fading channel cases will be interesting. Moreover, CCT link budget analysis including the impact of path-loss disparity can be used for abstraction in higher layer protocol design. Also, possible future work includes a detailed analysis of the impact of the virtual multi-input-single-output (VMISO) link asymmetry on network capacity and throughput in multi-hop networks.
4. Another future direction would be to implement OLA-PRISE proposed in Chapter 8. Experimental results of OLA-PRISE in a large scale network will provide guidelines to operate or selectively choose OLA-based routing protocols, OLA-PRISE and OLAROAD, and the conventional non-CT routing protocol depending on node degree, traffic model, and other system parameters.

## APPENDIX A

### PROOF OF THE PROPERTIES OF $H(X)$

The properties in Section 3.4.2 with  $\alpha > 2$  are proved as follows. The proof procedure is the same as [21], which assumes  $\alpha = 2$ , but the following functions and equations corresponding to  $\alpha > 2$  are different from [21].

1) When  $f(y) := \int_y^{y+x} G(u, \alpha, W) du$  with  $G$  is the term inside the integral in (9),  $f(y)$  is a monotonically decreasing function with respect to  $y$ , because the derivative of  $f(\cdot)$  is given by

$$f'(y) = G(y + x, \alpha, W) - G(y, \alpha, W). \quad (65)$$

For positive  $\bar{P}_r$  and  $W$  with  $\alpha > 2$ , it can be seen that  $f'(y) < 0$  by inspection. Also, the limiting values at zero and infinity can be found as  $\lim_{y \rightarrow 0} f(y) = \infty$  and  $\lim_{y \rightarrow \infty} f(y) = 0$ . Hence, there always exists a unique solution of the equation  $f(y) = \tau$ .

2) When  $\int_{h(x)}^{h(x)+x} G(u, \alpha, W) du = \frac{\tau}{\bar{P}_r}$ ,  $h'(x)$  can be obtained by differentiating the both sides with respect to  $x$  as

$$h'(x) = \frac{G(h(x) + x, \alpha, W)}{G(h(x), \alpha, W) - G(h(x) + x, \alpha, W)}, \quad (66)$$

The derivative of  $G(x, \alpha, \bar{P}_r, W)$  with respect to  $x$  is given by

$$\begin{aligned} \frac{dG(x, \alpha, W)}{dx} = & \frac{1}{8(\alpha - 2)Wx^5} \left( \frac{W^2}{4} + x^2 \right)^{-\alpha/2} \times \left( 4W^4x^2\Upsilon_1 + 8\alpha W^2x^4\Upsilon_1 - 64x^6\Upsilon_1 \right. \\ & + 32\alpha x^6\Upsilon_1 - 20W^4x^2\Upsilon_2 + 4\alpha W^4x^2\Upsilon_2 - 40\alpha W^2x^4\Upsilon_2 + 8\alpha^2 W^2x^4\Upsilon_2 \\ & + 64x^6\Upsilon_2 - 32\alpha x^6\Upsilon_2 + 3W^6\Upsilon_3 - \alpha W^6\Upsilon_3 + 24W^4x^2\Upsilon_3 - 8\alpha W^4x^2\Upsilon_3 \\ & + 48W^2x^4\Upsilon_3 - 16\alpha W^2x^4\Upsilon_3 + 15W^6\Upsilon_4 - 8\alpha W^6\Upsilon_4 + \alpha^2 W^6\Upsilon_4 + 72W^4x^2\Upsilon_4 \\ & \left. - 36\alpha W^4x^2\Upsilon_4 + 4\alpha^2 W^4x^2\Upsilon_4 + 48W^2x^4\Upsilon_4 - 16\alpha W^2x^4\Upsilon_4 \right), \end{aligned} \quad (67)$$

where  $\Upsilon_1 = {}_2F_1(1, \frac{3-\alpha}{2}, \frac{-1}{2}, \frac{-W^2}{4x^2})$ ,  $\Upsilon_2 = {}_2F_1(1, \frac{3-\alpha}{2}, \frac{1}{2}, \frac{-W^2}{4x^2})$ ,  $\Upsilon_3 = {}_2F_1(2, 1 + \frac{3-\alpha}{2}, \frac{1}{2}, \frac{-W^2}{4x^2})$ , and  $\Upsilon_4 = {}_2F_1(2, 1 + \frac{3-\alpha}{2}, \frac{3}{2}, \frac{-W^2}{4x^2})$ . Because  $\frac{dG(x, \alpha, W)}{dx} < 0$  for  $x > 0$ ,  $G(x, \alpha, W)$  is a monotonically

decreasing function with respect to  $x$ . Therefore,  $h'(x)$  is always positive for  $x > 0$ , which means  $h(\cdot)$  is monotonically increasing.

3) If we denote  $G(x, \alpha, W)$  by  $G(x)$  in short and  $\frac{dG(x, \alpha, W)}{dx}$  by  $G'(x)$ , the second derivative of  $h(\cdot)$  with respect to  $x$  is given by

$$h''(x) = \frac{(h' + 1)G'(h + x)G(h) - G(h + x)G'(h)h'}{(G(h) - G(h + x))^2}. \quad (68)$$

To show the concavity (i.e.,  $h''(x) < 0$ ), the numerator should be negative, which means  $(h' + 1)G'(h + x)G(h) < G(h + x)G'(h)h'$ . By dividing the both sides by  $h'$ , which is positive as proven in the second property, the inequality is given by  $(h' + 1)G'(h + x)G(h)/h' < G(h + x)G'(h)$ . If plugging (66), it can be expressed as

$$\frac{-G'(h + x)}{(G(h + x))^2} > \frac{-G'(h)}{(G(h))^2}, \quad (69)$$

It is true, because  $\frac{-G'(h)}{(G(h))^2}$  is increasing for any positive  $\alpha, W, \bar{P}_r$ , which is given by

$$\begin{aligned} \frac{-G'(h)}{(G(h))^2} &= 2(2 - \alpha)W\left(\frac{W^2}{4} + x^2\right)^{\alpha/2} \left( 4W^4x^2\Upsilon_1 + 8\alpha W^2x^4\Upsilon_1 - 64x^6\Upsilon_1 + 32\alpha x^6\Upsilon_1 \right. \\ &\quad - 20W^4x^2\Upsilon_2 + 4\alpha W^4x^2\Upsilon_2 - 40\alpha W^2x^4\Upsilon_2 + 8\alpha^2 W^2x^4\Upsilon_2 + 64x^6\Upsilon_2 \\ &\quad - 32\alpha x^6\Upsilon_2 + 3W^6\Upsilon_3 - \alpha W^6\Upsilon_3 + 24W^4x^2\Upsilon_3 - 8\alpha W^4x^2\Upsilon_3 + 48W^2x^4\Upsilon_3 \\ &\quad - 16\alpha W^2x^4\Upsilon_3 + 15W^6\Upsilon_4 - 8\alpha W^6\Upsilon_4 + \alpha^2 W^6\Upsilon_4 + 72W^4x^2\Upsilon_4 - 36\alpha W^4x^2\Upsilon_4 \\ &\quad \left. + 4\alpha^2 W^4x^2\Upsilon_4 + 48W^2x^4\Upsilon_4 - 16\alpha W^2x^4\Upsilon_4 \right) \\ &\quad / \left( x(W^2 + 4x^2)^2 (W^2\Upsilon_1 + 4x^2\Upsilon_1 - 5W^2\Upsilon_2 + \alpha W^2\Upsilon_2 - 4x^2\Upsilon_2)^2 \right). \end{aligned} \quad (70)$$

Hence,  $h(\cdot)$  is concave.

## APPENDIX B

### PROOF OF THEOREM 1

Let  $\mu_2$  be the version of  $\mu$  for the interference case. In other words, let  $\mu_2 = \exp\left(\frac{\tau(N+1)}{\pi\bar{P}_r}\right)$ .

Then, Lemma 2 implies  $\mu_2$  has a lower bound,

$$\mu_{2min} = \exp\left(\frac{\tau[1 + P(0 \leftarrow \mathbb{O}_{(1;\infty)})|_{\alpha=2}]}{\pi\bar{P}_r}\right). \quad (71)$$

By substituting (15),

$$\mu_{2min} = \frac{\mu}{(\mu - 1)^\tau}. \quad (72)$$

However,  $\frac{\mu}{(\mu-1)^\tau} > \frac{\mu}{\mu-1}$  and  $\frac{\mu}{\mu-1}$  is a decreasing function of  $\mu$  over  $1 < \mu < 2$ . For  $\mu = 2$ ,  $\frac{\mu}{\mu-1} = 2$ . Thus,  $\mu_{2min} > 2$ , when  $\tau \geq 1$ . Therefore, the second packet always stops propagating in finite hops, because the condition for infinite broadcast fails.

## APPENDIX C

### PROOF OF THEOREM 2

This can be proved by contradiction with the two-packet case as follows. Suppose two packets are successfully broadcasted. By the assumption,  $\mu = 2$ . We do not allow the transmit power  $\bar{P}_r$  to change between packets, so if  $\mu = 2$ , then  $\mu_2 = 2$ .

However, a finite packet insertion gap results in  $P(0 \leftarrow \mathbb{O}_{(1;M-1)})|_{\alpha=2} = \epsilon$ , where  $\epsilon$  is infinitesimally small positive value. Because 2 is the upper bound of  $\mu$  for the infinite OLA broadcast, even an infinitesimally small decrease in SINR by  $\epsilon(> 0)$  makes  $\mu$  greater than the upper bound

$$\mu_2 = \exp\left(\frac{\tau(\mathbf{N} + \mathbf{I})}{\pi\bar{P}_r}\right) = \mu^{(1+\epsilon)} > \mu = 2. \quad (73)$$

Hence, the supposition is false, which implies at least one of the two packets stops propagating. Therefore, when  $\mu = 2$ , the pipelined transmission with a finite  $M$  is impossible, too, when  $\tau \geq 1$ .



## APPENDIX D

### PROOF OF THEOREM 3

Suppose co-channel packets are inserted with packet insertion period of  $M$ . In Figure 11, simultaneous OLAs are indicated by the gray areas. We note that the OLAs are actually concentric rings, however, only partial areas of the OLAs are shown in the illustration. In the figure, the dark-gray area means the desired signal source  $\mathbb{O}_{(i,k)}$ , while the light-gray areas are the co-channel interfering OLAs, which are infinitely many in the infinite disk network. Also, the dotted line indicates a circle with a radius of  $r_{(i,k)} + \Delta$ , where  $\Delta > 0$ , and Point  $z$  is on the circle. The semicircle (C1) in Figure 11, the radius of which is  $\Delta$ , is centered at the point that is  $2\Delta$  away from Point  $z$  on the same x-axis. Moreover, the circle (C2), the radius of which is  $3\Delta$ , is centered at the point that is  $\Delta$  away from Point  $z$ . To be at-least-linearly propagating, the OLA should have boundaries that satisfy

$$r_{(i,k+1)} \geq r_{(i,k)} + \Delta. \quad (74)$$

In other words, the SINR at Point  $z$  must be greater than or equal to the decoding threshold  $\tau$  for at linearly increasing OLA boundaries.

First, the received signal power  $\mathbf{S}$  at Point  $z$  has a lower bound  $\mathbf{S}_{LB}$  as given by

$$\begin{aligned} \mathbf{S} &= P(\mathbb{O}_{(i,k)} \rightarrow z) \\ &> [\text{received power from area inside (C1)}] \\ &\geq \frac{\text{Area}(C1)\bar{P}_r}{(2\Delta)^\alpha} = \frac{\pi\bar{P}_r}{2^{\alpha+1}\Delta^{\alpha-2}} = \mathbf{S}_{LB}. \end{aligned} \quad (75)$$

On the other hand, the upper bound for the interference  $\mathbf{I}_{UB}$  from infinite number of the

co-channel packets with packet insertion period of  $M$  can be given by

$$\begin{aligned}
\mathbf{I} &= \sum_{j \neq 0} P(\mathbb{O}_{(i+j; k-Mj)} \rightarrow z) \\
&< [\text{received power from area outside (C2)}] \\
&\stackrel{(a)}{=} \int_0^{2\pi} \int_{(M-2)\Delta}^{\infty} \bar{P}_r \cdot l(r) d\theta dr \\
&= \frac{2\pi \bar{P}_r}{(\alpha-2)(M-2)^{\alpha-2} \Delta^{\alpha-2}} = \mathbf{I}_{UB}, \tag{76}
\end{aligned}$$

where the domain of the integration at (a) corresponds to the minimum distance from Point  $z$  to the closest co-channel OLA assuming linear propagation, which is  $(M-2)\Delta$  for  $M \geq 3$  as the worst case in terms of SINR. Moreover, we note that this upper bound is also highly inflated compared to the actual co-channel interference, because the domain of the integration is the whole network (to infinity) outside of the region in (C2).

It is feasible for spatially pipelined co-channel packets to propagate at least linearly, when the SINR at Point  $z$  is greater than or equal to  $\tau$ , which is guaranteed when the lower bound  $\mathbf{SINR}_{LB}$  is greater than  $\tau$  as

$$\mathbf{SINR}_{LB} = \frac{\mathbf{S}_{LB}}{\mathbf{I}_{UB} + \mathbf{N}} = \frac{\mathbf{S}_{LB}}{\mathbf{I}_{UB} + 1} \geq \tau, \tag{77}$$

where  $\mathbf{S}_{LB} = \frac{\pi \bar{P}_r}{2^{\alpha+1} \Delta^{\alpha-2}}$  and  $\mathbf{I}_{UB} = \frac{2\pi \bar{P}_r}{(\alpha-2)(M-2)^{\alpha-2} \Delta^{\alpha-2}}$  represent the lower bound of  $\mathbf{S}$  and the upper bound of  $\mathbf{I}$  in (75) and (76), respectively. Also,  $\mathbf{N} = 1$  by the unity power noise assumption. If there is a solution pair  $(M, \Delta)$ , where  $M \geq 3$  and  $\Delta > 0$ , the spatial pipelining of OLA broadcasts is possible without causing any packet loss in infinite disk networks, since all the packets propagate at least linearly across infinite disk networks by  $\Delta$ . Because  $\mathbf{SINR}_{LB}$  is a monotonically increasing function of  $M$ , there exist an infinite number of solutions  $M$  for a finite  $\tau$  and given value of  $\Delta$ , as long as the relay transmission power  $\bar{P}_r$  is large enough (it should at least pass the SNR threshold in the absence of interference).

## APPENDIX E

### PROOF OF THEOREM 4

We focus on the worst-case scenario in Section 5.2.3 assuming the infinite length, where a packet is in between infinitely many preceding and following co-channel packets as shown in Figure 66. If this packet (the dark-gray one in Figure 66) propagates at least linearly with a fixed step-size  $\Delta$ , then the other packets (the light-gray ones in Figure 66) also propagate at least linearly. We inflate the co-channel interference by treating all the inter-packet separation areas between any consecutive interfering OLAs as interfering areas, which makes two (preceding and following) infinitely large interfering OLAs: the two areas (S 1) and (S 2) indicated by the thick black lines in Figure 66. We will prove that if the worst-case packet has the inter-separation of  $M\Delta$  to the two infinitely-large-area interfering OLAs, this packet is at-least-linearly propagating by  $\Delta$ .

Suppose the packets are inserted with the period of  $M$ . In Figure 66, the dark-gray area is the desired signal source  $\tilde{\mathcal{O}}_{(i,k)}$ , while the light-gray areas represent the interfering OLAs  $\tilde{\mathcal{O}}_{(i+j,k-Mj)}$  with  $j \neq 0$ , which are infinitely many for infinite  $L$ . For Packet  $i$  to propagate at least linearly, its  $k$ th level boundary  $x_{(i,k)}$  must satisfy

$$x_{(i,k)} \geq k\Delta, \quad (78)$$

where  $\Delta$  is an arbitrary positive number. Moreover, the  $k$ th step-size  $r_{(i,k)}$  of  $\tilde{\mathcal{O}}_{(i,k)}$  must satisfy  $r_{(i,k)} \geq \Delta$ . To satisfy (78), the received SINR at Point  $z$ , which is  $\Delta$  away from  $x_{(i,k)}$ , should be greater than or equal to  $\tau$ . For the SINR calculation in this proof, we use the two large OLAs (S 1) and (S 2) in Figure 66. First, the received signal power  $\mathbf{S}$  at Point  $z$  has an lower bound  $\mathbf{S}_{LB}$ , which is derived as

$$\begin{aligned} \mathbf{S} &= P(\tilde{\mathcal{O}}_{(i,k)} \rightarrow z) \\ &> \frac{\bar{P}_r \cdot \text{Area}[\tilde{\mathcal{O}}_{(i,k)}]}{(2\Delta)^\alpha} = \frac{\bar{P}_r W}{2^\alpha \Delta^{\alpha-1}} = \mathbf{S}_{LB}, \end{aligned} \quad (79)$$

where  $\alpha \geq 2$  and  $W < \Delta$  for the rectangular approximation in Figure 7. On the other hand,

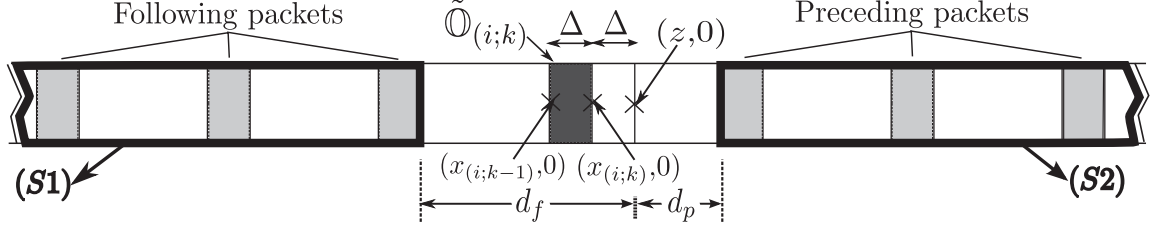


**Figure 66:** Illustration of the spatially pipelined OLA transmission in infinite strip network

the interference is divided into two: the interferences from the preceding packets and from the following packets, which are denote by  $\mathbf{I}_p$  and  $\mathbf{I}_f$ , respectively. Using the “two infinite-length OLAs” approach, the separation from Point  $z$  to  $(S1)$  is  $d_f$ , while the separation from Point  $z$  to  $(S2)$  is  $d_p$ . When the packets propagate at least linearly,  $d_f \geq (M+1)\Delta$  and  $d_p \geq (M-2)\Delta$ . Hence, the upper bound for the interference  $\mathbf{I}_{UB}$  with packet insertion period of  $M$  can be given by

$$\begin{aligned}
 \mathbf{I} &= \sum_{j \neq 0} P(\tilde{\mathcal{O}}_{(i+j;k-Mj)} \rightarrow z) = \mathbf{I}_p + \mathbf{I}_f \\
 &< \bar{P}_r W \int_{(M-2)\Delta}^{\infty} \frac{1}{x^\alpha} dx + \bar{P}_r W \int_{(M+1)\Delta}^{\infty} \frac{1}{x^\alpha} dx \\
 &= \frac{\bar{P}_r W}{(\alpha-1)\Delta^{\alpha-1}} \left( \frac{1}{(M-2)^{\alpha-1}} + \frac{1}{(M+1)^{\alpha-1}} \right) \\
 &< \frac{2\bar{P}_r W}{(\alpha-1)\Delta^{\alpha-1}(M-2)^{\alpha-1}} = \mathbf{I}_{UB},
 \end{aligned} \tag{80}$$

Therefore, using (79) and (80), we can derive the lower bound of the received SINR at Point  $z$ , which is denoted by  $\mathbf{SINR}_{LB}$ . Therefore, the co-channel packets propagate at least linearly, if the following inequality holds to satisfy the decoding condition at Point  $z$ :

$$\mathbf{SINR}_{LB} = \frac{\mathbf{S}_{LB}}{\mathbf{I}_{UB} + 1} = \frac{\frac{\bar{P}_r W}{2^\alpha \Delta^{\alpha-1}}}{\frac{2\bar{P}_r W}{(\alpha-1)\Delta^{\alpha-1}(M-2)^{\alpha-1}} + 1} \geq \tau. \tag{81}$$

Because  $\mathbf{SINR}_{LB}$  is a monotonically increasing function of  $M$ , when  $\tau < \infty$  with large enough  $\bar{P}_r$ , there always exists a solution pair  $(M, \Delta)$ , where  $M \geq 3$  and  $\Delta > 0$ . Therefore, if  $k$ th level OLA has a step-size of  $\Delta$ , the  $(k+1)$ st level OLA also has a step-size greater than or equal to  $\Delta$  with a finite  $M$ .

Also, when a new packet is inserted at the source, which corresponds to  $k = 0$ , the signal component  $\mathbf{S}$  of  $P_s/\Delta^\alpha$ , and the interference is only from the preceding packets because it does not have any following packet yet. Therefore, the interference from the preceding packets, which is smaller than  $\mathbf{I}_{UB}$  in (80), is a monotonically decreasing function of  $M$ . Hence, with large enough  $P_s$ , we can guarantee the initial step-size  $r_{(i;1)} = \Delta$  by using a finite  $M$  as well. Thus, it is shown that (78) can be satisfied with finite  $M$  as long as the decoding threshold is also finite.

## REFERENCES

- [1] G. Jakllari, S. V. Krishnamurthy, M. Faloutsos, P. V. Krishnamurthy, and O. Ercetin, “A cross-layer framework for exploiting virtual MISO links in mobile ad hoc networks,” *IEEE Trans. Mobile Computing*, vol. 6, pp. 579–594, June 2007.
- [2] J. Yackoski, L. Zhang, C.-C. Shen, L. Cimini, and B. Gui, “Networking with cooperative communications: Holistic design and realistic evaluation,” *Commun. Magazine, IEEE*, vol. 47, pp. 113–119, Aug. 2009.
- [3] R. Ramanathan, “Challenges: a radically new architecture for next generation mobile ad hoc networks,” in *Proc. ACM MobiCom*.
- [4] 3GPP TR 36.819 v11.0.0, “Coordinated Multi-Point Operation for LTE,” *3GPP TSG RAN WG1*, 2011.
- [5] L. Thanayankizil, A. Kailas, and M. A. Ingram, “Routing for wireless sensor networks with an opportunistic large array (OLA) physical layer,” *Ad Hoc & Sensor Wireless Networks*, vol. 8, no. 1-2, pp. 79–117, 2009.
- [6] X. Hong, K. Xu, and M. Gerla, “Scalable routing protocols for mobile ad hoc networks,” *IEEE Network*, vol. 16, no. 4, pp. 11–21, 2002.
- [7] J. Laneman, D. Tse, and G. Wornell, “Cooperative diversity in wireless networks: Efficient protocols and outage behavior,” *IEEE Trans. Inf. Theory*, vol. 50, pp. 3062–3080, Dec. 2004.
- [8] S. Cui, A. Goldsmith, and A. Bahai, “Energy-efficiency of mimo and cooperative mimo techniques in sensor networks,” *IEEE J. on Sel. Areas in Commun.*, vol. 22, no. 6, pp. 1089–1098, 2004.

- [9] A. Scaglione and Y.-W. Hong, "Opportunistic large arrays: cooperative transmission in wireless multihop ad hoc networks to reach far distances," *IEEE Trans. Sig. Proc.*, vol. 51, pp. 2082–2092, Aug. 2003.
- [10] I. Maric and R. Yates, "Cooperative multihop broadcast for wireless networks," *IEEE J. on Sel. Areas in Commun.*, vol. 22, pp. 1080–1088, Aug. 2004.
- [11] G. Jakllari, S. V. Krishnamurthy, M. Faloutsos, and P. V. Krishnamurthy, "On broadcasting with cooperative diversity in multi-hop wireless networks," *IEEE J. on Sel. Areas in Commun.*, vol. 25, pp. 484–496, Feb. 2007.
- [12] T. Halford and K. Chugg, "Barrage relay networks," in *Proc. Inf. Theory and Applications Workshop (ITA)*, pp. 1–8, Feb. 2010.
- [13] Y. J. Chang, H. Jung, and M. A. Ingram, "Demonstration of an OLA-based cooperative routing protocol in an indoor environment," in *Proc. IEEE European Wireless*, pp. 1–8, Apr. 2011.
- [14] T. Halford, T. Courtade, and K. Turck, "The user capacity of barrage relay networks," *IEEE MILCOM*, pp. 1–6, 2012.
- [15] P. Gupta and P. Kumar, "The capacity of wireless networks," *IEEE Trans. Inf. Theory*, vol. 46, pp. 388–404, Mar. 2000.
- [16] B. Sirkeci-Mergen and M. Gastpar, "On the broadcast capacity of wireless networks with cooperative relays," *IEEE Trans. Info Theory*, vol. 56, pp. 3847–3861, Aug. 2010.
- [17] M.-K. Oh, X. Ma, G. Giannakis, and D.-J. Park, "Cooperative synchronization and channel estimation in wireless sensor networks," in *Proc. IEEE Conf. on Signals, System and Computers (ASILOMAR)*, vol. 1, pp. 238–242, Nov. 2003.

- [18] A. Bader and E. Ekici, "Performance optimization of interference-limited multihop networks," *IEEE/ACM Trans. Networking*, vol. 16, pp. 1147–1160, Oct. 2008.
- [19] B. Sirkeci-Mergen, A. Scaglione, and G. Mergen, "Asymptotic analysis of multi-stage cooperative broadcast in wireless networks," *IEEE Trans. Inf. Theory*, vol. 52, pp. 2531–2550, June 2006. corrected version: <http://crisp.ece.cornell.edu/papers/BirsenITTran2006.pdf>.
- [20] A. Kailas and M. A. Ingram, "Alternating opportunistic large arrays in broadcasting for network lifetime extension," *IEEE Trans. Wireless Commun.*, vol. 8, no. 6, pp. 2831–2835, 2009.
- [21] B. Sirkeci-Mersén and A. Scaglione, "A continuum approach to dense wireless networks with cooperation," in *Proc. INFOCOM*, vol. 4, pp. 2755–2763 vol. 4, Mar. 2005.
- [22] A. Kailas and M. A. Ingram, "Analysis of a simple recruiting method for cooperative routes and strip networks," *IEEE Trans. Wireless Commun.*, vol. 9, pp. 2415–2419, Aug. 2010.
- [23] S. Hassan and M. A. Ingram, "A quasi-stationary markov chain model of a cooperative multi-hop linear network," *IEEE Trans. Wireless Commun.*, vol. 10, no. 7, pp. 2306–2315, 2011.
- [24] S. Hassan and M. A. Ingram, "On the modeling of randomized distributed cooperation for linear multi-hop networks," in *Proc. IEEE ICC*, pp. 366–370, 2012.
- [25] B. Williams and T. Camp, "Comparison of broadcasting techniques for mobile ad hoc networks," in *Proc. ACM MobiHoc*, pp. 194–205, 2002.
- [26] S.-Y. Ni, Y.-C. Tseng, Y.-S. Chen, and J.-P. Sheu, "The broadcast storm problem in a mobile ad hoc network," in *Proc. ACM/IEEE MobiCom*, pp. 151–162, 1999.



- [27] Q. Zhang and D. Agrawal, "Dynamic probabilistic broadcasting in mobile ad hoc networks," in *Proc. IEEE VTC*, vol. 5, pp. 2860–2864 Vol.5, Oct. 2003.
- [28] J. E. Wieselthier, G. D. Nguyen, and A. Ephremides, "Energy-efficient broadcast and multicast trees in wireless networks," *Mobile Networks and Applications*, vol. 7, pp. 481–492, 2002.
- [29] A. Das, R. Marks, M. El-Sharkawi, P. Arabshahi, and A. Gray, "Minimum power broadcast trees for wireless networks: integer programming formulations," in *Proc. INFOCOM*, vol. 2, pp. 1001–1010 vol.2, Mar. 2003.
- [30] Q. Yang, L. Shen, and W. Xia, "Distributed probabilistic broadcasting for safety applications in vehicular ad hoc networks," in *Proc. Int. Conf. on Wireless Commun. Sig. Proc.*, pp. 1–5, Nov. 2009.
- [31] A. Ahizoune, A. Hafid, and R. Ben Ali, "A contention-free broadcast protocol for periodic safety messages in vehicular ad-hoc networks," in *Proc. IEEE Conf. on Local Computer Networks (LCN)*, pp. 48–55, Oct. 2010.
- [32] J. Laneman and G. Wornell, "Distributed space-time-coded protocols for exploiting cooperative diversity in wireless networks," *IEEE Trans. Inf. Theory*, vol. 49, pp. 2415–2425, Oct. 2003.
- [33] L. Thanayankizil and M. Ingram, "Reactive routing for multi-hop dynamic ad hoc networks based on opportunistic large arrays," in *Proc. IEEE GLOBECOM*, pp. 1–6, 2008.
- [34] L. Thanayankizil, A. Kailas, and M. A. Ingram, "Opportunistic large array concentric routing algorithm (OLACRA) for upstream routing in wireless sensor networks," *Ad Hoc Networks*, vol. 8, no. 1-2, pp. 79–117, 2011.

- [35] T. Halford, K. Chugg, and A. Polydoros, "Barrage relay networks: System and protocol design," in *Proc. IEEE PIMRC*, pp. 1133–1138, Sept. 2010.
- [36] C. E. Perkins, E. M. Belding-Royer, and S. R. Das, "Ad hoc on-demand distance vector (AODV) routing," RFC Experimental 3561, Internet Engineering Task Force, July 2003.
- [37] W. Ge, J. Zhang, and G. Xue, "Cooperative geographic routing in wireless sensor networks," in *Proc. IEEE MILCOM*, pp. 1–7, Oct. 2006.
- [38] S. Kim, S. Pakzad, D. Culler, J. Demmel, G. Fenves, S. Glaser, and M. Turon, "Health monitoring of civil infrastructures using wireless sensor networks," in *Proc. IEEE Intl Symp. Info. Processing in Sensor Networks (IPSN)*, pp. 254–263, Apr. 2007.
- [39] D. De Caneva, P. Montessoro, and D. Pierattoni, "WiWi: Deterministic and fault tolerant wireless communication over a strip of pervasive devices," in *Proc. 4th IEEE Wireless Commun., Networking, and Mobile Computing Conf.*, pp. 1–5, Oct. 2008.
- [40] J. Laneman, "Limiting analysis of outage probabilities for diversity schemes in fading channels," in *Proc. IEEE GLOBECOM*, vol. 3, pp. 1242–1246 vol.3, Dec. 2003.
- [41] N. C. Beaulieu and J. Hu, "A closed-form expression for the outage probability of decode-and-forward relaying in dissimilar rayleigh fading channels," *IEEE Commun. Letters*, vol. 10, pp. 813–815, december 2006.
- [42] S. Lakshmanan and R. Sivakumar, "Diversity routing for multi-hop wireless networks with cooperative transmissions," in *Proc. IEEE SECON*, pp. 1–9, June 2009.
- [43] J. W. Jung and M. A. Ingram, "Residual-energy activated cooperative transmission (REACT) to avoid the energy hole," in *Proc. IEEE ICC*, June 2010.
- [44] A. Scaglione, D. Goeckel, and J. Laneman, "Cooperative communications in mobile ad hoc networks," *IEEE Sig. Proc. Magazine*, vol. 23, pp. 18–29, Sept. 2006.

- [45] A. Scaglione and Y.-W. Hong, “Opportunistic large arrays: cooperative transmission in wireless multihop ad hoc networks to reach far distances,” *IEEE Trans. Sig. Proc.*, vol. 51, pp. 2082 – 2092, Aug. 2003.
- [46] A. Kailas and M. A. Ingram, “Alternating opportunistic large arrays in broadcasting for network lifetime extension,” *IEEE Trans. Wireless Commun.*, vol. 8, pp. 2831–2835, June 2009.
- [47] A. Aksu and O. Ercetin, “Reliable multi-hop routing with cooperative transmissions in energy-constrained networks,” *IEEE Trans. Wireless Commun.*, vol. 7, pp. 2861 –2865, Aug. 2008.
- [48] J. Lin and M. A. Ingram, “SCT-MAC: A scheduling duty cycle mac protocol for cooperative wireless sensor network,” in *Proc. IEEE ICC 2012*, June 2012.
- [49] B. Bash, D. Goeckel, and D. Towsley, “Clustering in cooperative networks,” in *Proc. IEEE INFOCOM 2011*, pp. 486 –490, Apr. 2011.
- [50] V. Ramasubramanian and D. Mosse, “BRA: A bidirectional routing abstraction for asymmetric mobile ad hoc networks,” *IEEE/ACM Trans. Networking*, vol. 16, no. 1, pp. 116–129, 2008.
- [51] V. Ramasubramanian, R. Chandra, and D. Mosse, “Providing a bidirectional abstraction for unidirectional ad hoc networks,” in *Proc. IEEE INFOCOM*, vol. 3, pp. 1258 – 1267 vol.3, 2002.
- [52] “IEEE Standard for Wireless LAN Medium Access Control (MAC) and Physical Layer (PHY) Specifications,” Nov. 1997.
- [53] G. Caire and S. Shamai, “On the capacity of some channels with channel state information,” *IEEE Trans. Info Theory*, vol. 45, no. 6, pp. 2007–2019, 1999.

- [54] Y. J. Chang, M. A. Ingram, and S. Frazier, "Cluster transmission time synchronization for cooperative transmission using software defined radio," in *Proc. IEEE ICC*, June 2010.
- [55] B. Gui, L. Dai, and L. Cimini, "Routing strategies in multihop cooperative networks," *IEEE Trans. Wireless Commun.*, vol. 8, no. 2, pp. 843–855, 2009.
- [56] K. Phil, C. Bormann, G. Fairhurst, D. Grossman, R. Ludwig, J. Mahdavi, G. Montenegro, J. Touch, and L. Wood, "RFC 3819: Advice for internet subnetwork designers," tech. rep.
- [57] J. Proakis, *Digital Communications*. McGraw-Hill, 2000.
- [58] H. Jung and M. A. Ingram, "SNR penalty from the path-loss disparity in virtual multiple-input-single-output (VMISO) link," in *Proc. IEEE ICC*, June 2013.
- [59] G. L. Stuber, *Principles of Mobile Communications, second ed.* Kluwer Academics Publishers, 2000.
- [60] A. Kailas, L. Thanayankizil, and M. A. Ingram, "A simple cooperative transmission protocol for energy-efficient broadcasting over multi-hop wireless networks," *Journal of Communications and Networks*, vol. 10, no. 2, pp. 213–220, 2008.
- [61] A. Kailas, "On the performance of alternating concurrent cooperative transmissions in the high path-loss attenuation regime," *Int. Journal of Network Protocols and Algorithms*, vol. 4, no. 2, pp. 68–81, 2012.
- [62] M. Abramowitz and I. Stegun, *Handbook of mathematical functions with formulas, graphs, and mathematical tables*, vol. 55. Dover publications, 1964.
- [63] M. Garetto, T. Salonidis, and E. Knightly, "Modeling per-flow throughput and capturing starvation in CSMA multi-hop wireless networks," *IEEE/ACM Trans. Networking*, vol. 16, pp. 864–877, Aug. 2008.

- [64] T. Rappaport, *Wireless Communications: Principles and Practice*. Prentice Hall PTR, 2001.
- [65] H. Jung and M. A. Weitnauer, “Link asymmetry in virtual miso-based networks,” *to be presented at IEEE MILCOM*, Nov. 2013.
- [66] Z. Zhou, S. Zhou, S. Cui, and J.-H. Cui, “Energy-efficient cooperative communication in a clustered wireless sensor network,” *IEEE Trans. Vehicular Tech.*, vol. 57, pp. 3618–3628, Nov. 2008.
- [67] S. Ross, *Introduction to Probability Models*. 2000.
- [68] M. Abramowitz and I. A. Stegun, *Handbook of Mathematical Functions 10th Printing with Corrections*. Dover, New York, 1972.
- [69] M. K. Simon and M.-S. Alouini, “On the difference of two chi-square variates with application to outage probability computation,” *IEEE Trans. Commun.*, vol. 49, no. 11, pp. 1946–1954, 2001.
- [70] “Universal Software Radio Peripheral.” <http://www.ettus.com>.
- [71] “GNU Radio.” <http://gnuradio.org>.
- [72] P.-S. Kildal and K. Rosengren, “Correlation and capacity of MIMO systems and mutual coupling, radiation efficiency, and diversity gain of their antennas: simulations and measurements in a reverberation chamber,” *IEEE Commun. Mag.*, vol. 42, pp. 104–112, Dec. 2004.
- [73] N. Jalden, P. Zetterberg, B. Ottersten, A. Hong, and R. Thoma, “Correlation properties of large scale fading based on indoor measurements,” in *Proc. IEEE WCNC*, pp. 1894–1899, Mar. 2007.
- [74] C. Anderson and T. Rappaport, “In-building wideband partition loss measurements at 2.5 and 60 ghz,” *IEEE Trans. Wireless Commun.*, vol. 3, pp. 922–928, May 2004.

- [75] M. K. Simon and M.-S. Alouini, *Digital Communication over Fading Channels*. Wiley-IEEE Press, 2002.
- [76] M. Gudmundson, “Correlation model for shadow fading in mobile radio systems,” *Electronics Letters*, vol. 27, pp. 2145–2146, 7 1991.
- [77] L. Thanayankizil and M. Ingram, “Reactive robust routing with opportunistic large arrays,” in *Proc. IEEE ICC*, pp. 1–5, June 2009.
- [78] B. Crow, I. Widjaja, L. Kim, and P. Sakai, “IEEE 802.11 wireless local area networks,” *IEEE Commun. Magazine*, vol. 35, pp. 116–126, Sept. 1997.
- [79] I. Chakeres and E. Belding-Royer, “AODV routing protocol implementation design,” Mar. 2004.
- [80] “GTNets.” <http://www.ece.gatech.edu/research/labs/MANIACS/GTNetS/>.
- [81] B. Sklar, *Digital communications: fundamentals and applications*. Prentice-Hall, Inc., 1988.
- [82] H. Lundgren, E. Nordström, and C. Tschudin, “Coping with communication gray zones in IEEE 802.11b based ad hoc networks,” in *Proc. ACM Int. Workshop on Wireless Mobile Multimedia*, pp. 49–55, 2002.